AN ABSTRACT OF THE THESIS OF

Udom Techakijkajorn for the degree of Master of Science in Chemical Engineering presented on October 4, 1995. Title: Sintering of Fume Deposits in Kraft Recovery Boilers.

Redacted for Privacy

Abstract approved : _____

William James Frederick

Fume, sub-micron aerosal particles in the combustion gases, have been identified as a cause of extensive plugging and fouling in the heat transfer section of a kraft recovery boiler in kraft pulp mills. After the deposition on the heat transfer surface, fume deposits will undergo the sintering process which causes densification and hardening, making them hard to remove. There has been relatively little information available on the kinetics of the sintering of fume particles, and no information on the modeling of the sintering process of this particular material. No conclusion about the effect of chloride species on the sintering of fume particles has been made.

A series of sintering tests in air at various temperatures were conducted using dense pellets made from a specific fume dust which contains a low amount of chlorides. Each pellet was heated at a constant temperature, ranging from 300 ^{0}C to 550 ^{0}C, for a different time interval. By the study of the microstructural change of each sintered specimen, the initial stage, intermediate stage, and final stage of sintering were identified. By the presence of an empirical constant K_1, the relative linear shrinkage data

in the initial stage sintering fit well with the model proposed by Kingery and Berg[7] when volume diffusion is the controlling mechanism. By the presence of an empirical constant K_2 and the application of grain growth data, the porosity-time data in the intermediate stage sintering fit well with the model proposed by Coble[16] when volume diffusion is the controlling mechanism. The apparent activation energy obtained from the initial stage sintering is equal to 54.5 ± 27.7 kcal/mol which is in good agreement with the apparent activation energy obtained from the intermediate stage sintering which is equal to 56.0 ± 31.3 kcal/mol. A semi-empirical model for the sintering process of this particular well-packed fume dust was formulated. The model does not apply well to the loosely-packed fume dust due to some unidentified factors

The same experiment was carried out for the other fume dust which contains a high amount of chloride. By the use of the fractional density, the qualitative comparison of the sintering of the low chloride and high chloride dusts was made. At low temperatures, the sintering rate of the high chloride fume dust is lower than that of the low chloride fume dust. At high temperatures, both dusts have the same sintering rate and can sinter close to the theoretical density. It is postulated here that the retarded grain growth rate for the high chloride dust can improve the densification process in the intermediate stage sintering.

Sintering of Fume Deposits in Kraft Recovery Boilers

by

Udom Techakijkajorn

A THESIS

submitted to

Oregon State University

in partial fulfillment of

the requirements for the

degree of

Master of Science

Completed October 4, 1995

Commencement June, 1996

Master of Science thesis of Udom Techakijkajorn presented on October 4, 1995

APPROVED :

Redacted for Privacy

Major Professor, representing Chemical Engineering

Redacted for Privacy

Chair of Department of Chemical Engineering

Redacted for Privacy

Dean of Graduate Schlool

I understand that my thesis will become part of the permanent collection of Oregon State University libraries. My signature below authorizes release of my thesis to any reader upon request.

Redacted for Privacy

Udom Techakijkajorn, Author

ACKNOWLEDGEMENTS

I would like to take this opportunity to thank all the people who directly or indirectly helped me in getting through this long and winding road.

Many thanks to:

- all the professors for providing the great education
- Dr.Frederick for his kindness, guidance, financial support which also includes all the expenses for the two-month Toronto research trip, and his sense of humor which makes him a real nice person to work with
- Dr.Barham and Dr.Tran from the University of Toronto and Dr.Skrifvars from the Abo Akademi for valuable discussions
- Dr.Iisa, Dr.Jovanovic, Dr.Kimura, and Dr.Rochefort for their valuable advice
- all the fellow colleagues, particularly those of the combustion group
- Alarick, Farshad, Sue, and other fellows from the University of Toronto for their great support and dearly friendship during my memorable research trip
- all my friends and my loved one in Toronto for their warm welcome and encouragement
- Dawn Belveal and Jordana Chambers, for always being there when needed
- my parents for all their support and care

This work has been supported by the US Department of Energy's Office of Industrial Technoligies. The support is gratefully acknowledged.

TABLE OF CONTENTS

CHAPTER		Page
1	INTRODUCTION	1
	1.1 Problem Statement	1
	1.2 Recovery Boiler Fundamental	2
	1.3 Fireside Deposits in Recovery Boiler	5
	1.4 Sintering Process	6
	1.5 Objectives	6
2	SINTERING THEORY	8
	2.1 Fundamental Knowledge	8
	2.2 Solid-State Sintering Models	11
	2.2.1 Initial Stage Sintering Models	12
	2.2.2 Intermediate Stage Sintering Models	24
	2.3 Grain Growth	26
	2.4 Activated Sintering	29
3	LITERATURE STUDY	32
	3.1 Application of Sintering Models	32
	3.2 Fume Formation	32
	3.3 Sintering of Fume Particles	34
4	EXPERIMENTAL METHODS	36
	4.1 Materials	36

TABLE OF CONTENTS (continued)

CHAPTER		Page
	4.2 Equipment	36
	4.3 Experimental Procedure	39
	4.3.1 Pellet Making	39
	4.3.2 Sintering Test	39
5	RESULTS AND DISCUSSION	42
	5.1 Side Reaction During Sintering	42
	5.2 Reproducibility	42
	5.3 Temperature Effect	43
	5.4 Microstructural Development	48
	5.5 Effect of Initial Density	57
	5.6 Final Density	58
	5.7 Effect of Chloride Contents	58
6	MODELING OF SINTERING OF LOW CHLORIDE DUST	64
	6.1 Initial Stage Sintering	64
	6.2 Grain Growth	68
	6.2.1 Grain Growth Rate at 400 ^{0}C	68
	6.2.2 Grain Growth Rate at 450 ^{0}C	70
	6.2.3 Grain Growth Rate at 500 ^{0}C	70
	6.3 Intermediate Stage Sintering	74

TABLE OF CONTENTS (continued)

CHAPTER		Page
	6.4 Model Testing	84
7	CONCLUSION	91
	7.1 Initial Stage Sintering Model	91
	7.2 Intermediate Stage Sintering Model	92
	BIBLIOGRAPHY	94
	APPENDICES	96
	APPENDIX A - Experimental Data	97
	APPENDIX B - Modeling of Tran's Sintering Data	114
	APPENDIX C - Phase Diagram of KCl-NaCl-K_2SO_4-Na_2SO_4 system	117
	APPENDIX D - Grain Growth Data	118
	APPENDIX E - Fractional Density and Porosity Data	119

LIST OF FIGURES

FIGURE		Page
1.1	Schematic diagram of a kraft recovery boiler	4
2.1	Microstructural development in each stage of sintering	10
2.2	Two-sphere model	13
2.3	Effects of diffusion mechanisms on the geometry of the model	14
2.4	Approaching sphere model	16
2.5	Tetrakaidecahedron formed from truncated Octahedron	25
2.6	Grain-boundary movement	27
2.7	Pore agglomeration by grain-boundary movement	28
2.8	Densification mechanisms during sintering	30
2.9	Mechanisms for the control of boundary migration and hence for the control of grain growth during sintering	31
3.1	Fume formation mechanisms in the presence of metal oxide seeds	33
4.1	Pellet holder	37
4.2	Experimental setup	38
5.1	Isotherms of density change with time for low chloride dust	44
5.2	Isotherms of density change with time for high chloride dust	45
5.3	SEM picture of a pellet (low chloride dust) sintered at 550 ^{0}C for 30 minutes	47
5.4	SEM pictures of precipitator dusts	48
5.5	SEM pictures of pellets (low chloride dust) sintered for 8 hours at various temperatures	49

LIST OF FIGURES (continued)

FIGURE		Page
5.6	Final grain size at each sintering temperature	51
5.7	SEM pictures of pellets (low chloride dust) sintered at 400 ^{0}C	52
5.8	SEM pictures of pellets (low chloride dust) sintered at 450 ^{0}C	53
5.9	SEM pictures of pellets (low chloride dust) sintered at 500 ^{0}C	54
5.10	Isotherms of average grain size change with time	56
5.11	Sintering of pellets (low chloride) with different initial density at 450 ^{0}C	57
5.12	Fractional density change with time of two dusts	59
5.13	Morphology of pellets sintered at 450 ^{0}C for 60 minutes	62
6.1	Relative linear shrinkage as a function of time for the initial stage sintering	65
6.2	Arhenius-type plot of K_1	67
6.3	Grain growth rate at 400 ^{0}C	69
6.4	Grain growth rate at 450 ^{0}C	71
6.5	Grain growth rate at 500 ^{0}C	72
6.6	Arhenius-type plot of grain growth rate constant m	73
6.7	Porosity change with time during the intermediate stage sintering at 400 ^{0}C	80
6.8	Porosity change with time during the intermediate stage sintering at 450 ^{0}C	81
6.9	Porosity change with time during the intermediate stage sintering at 500 ^{0}C	82
6.10	Arhenius-type plot of K_2	83
6.11	Porosity change with time (model testing)	86

LIST OF FIGURES (continued)

FIGURE		Page
6.12	Grain size change with time (model testing)	87
6.13	Final grain size at each sintering temperature (model testing)	88
6.14	The effect of different pellet green density on the sintering at 450 ^{0}C (model testing)	89

LIST OF TABLES

TABLE		Page
1.1	Sample analysis of a typical black liquor	3
2.1	Geometry relations used in sintering models	17
2.2	Numerical constants for initial stage sintering model	20
4.1	Chemical composition as weight percent of the two precipitator dusts	36
4.2	Sintering temperature and time schemes	41
5.1	Reproducibility testing	43
5.2	Comparison of final density of pellets sintered at 500 and 550 ^{0}C	47
5.3	Theoretical densities of the dusts	58
5.4	Comparison of the average final fractional density of pellets made from different dusts sintered at various temperature	60
6.1	Value K_1 at 300-400 ^{0}C	67
6.2	Values t, G, $t-t_0$, and $G^3-G_0^3$ for grain growth at 400^{0}C	69
6.3	Values t, G, $t-t_0$, and $G^3-G_0^3$ for grain growth at 450^{0}C	70
6.4	Values t, G, $t-t_0$, and $G^3-G_0^3$ for grain growth at 500^{0}C	71
6.5	Grain growth rate constant m at 400-500 ^{0}C	72
6.6	The values Λ at each porosity-time data for each individual pellet during the intermediate stage sintering at 400 ^{0}C	77
6.7	The values Λ at each porosity-time data for each individual pellet during the intermediate stage sintering at 450 ^{0}C	78

LIST OF TABLES (continued)

TABLE		Page
6.8	The values Λ at each porosity-time data for each individual pellet during the intermediate stage sintering at 500 ^{0}C	79
6.9	Value K_2 at 400-500 ^{0}C	83

LIST OF APPENDIX FIGURES

FIGURE		Page
B.1	Tran's experimental data	114
C.1	Phase diagram of KCl-NaCl-K_2SO_4-Na_2SO_4 system	117

LIST OF APPENDIX TABLES

TABLE		Page
A-1	Experimental data for sintering of low chloride dust at 300 ^{0}C	97
A-2	Experimental data for sintering of low chloride dust at 350 ^{0}C	98
A-3	Experimental data for sintering of low chloride dust at 400 ^{0}C	100
A-4	Experimental data for sintering of low chloride dust at 450 ^{0}C	101
A-5	Experimental data for sintering of low chloride dust at 500 ^{0}C	106
A-6	Experimental data for sintering of low chloride dust at 550 ^{0}C	108
A-7	Experimental data for sintering of high chloride dust at 350 ^{0}C	109
A-8	Experimental data for sintering of high chloride dust at 400 ^{0}C	110
A-9	Experimental data for sintering of high chloride dust at 450 ^{0}C	111
A-10	Experimental data for sintering of high chloride dust at 500 ^{0}C	112
A-11	Experimental data for sintering of high chloride dust at 550 ^{0}C	113
B-1	Tran's grain growth data	115
D-1	Grain growth data	118
E-1	Fractional density and porosity of low chloride dust sintered at 300 ^{0}C	119
E-2	Fractional density and porosity of low chloride dust sintered at 350 ^{0}C	120
E-3	Fractional density and porosity of low chloride dust sintered at 400 ^{0}C	121
E-4	Fractional density and porosity of low chloride dust sintered at 450 ^{0}C	123
E-5	Fractional density and porosity of low chloride dust sintered at 500 ^{0}C	128
E-6	Fractional density and porosity of high chloride dust sintered at 350 ^{0}C	130

LIST OF APPENDIX TABLES (continued)

TABLE		Page
E-7	Fractional density and porosity of high chloride dust sintered at 400 ^{0}C	131
E-8	Fractional density and porosity of high chloride dust sintered at 450 ^{0}C	132
E-9	Fractional density and porosity of high chloride dust sintered at 500 ^{0}C	133

SYMBOLS

A_1, A_2	=	numerical constants
b	=	grain-boundary thickness
D	=	diffusion coefficient
D_{GB}	=	grain-boundary diffusion coefficient
D_V	=	volume diffusion coefficient
$\Delta L/L_0$	=	relative linear shrinkage
E_G	=	activation energy of the grain growth process
E_1, E_2	=	activation energies of the sintering processes
G	=	instantaneous grain size
G_0	=	initial grain size
γ	=	surface energy
K	=	numerical constant
K_1,K_1',K_2,K_2'	=	empirical constants for the sintering models
k	=	Boltzman's constant
m,m_0	=	grain growth rate constants
N	=	numerical constant
N_1	=	number of interconnected voids per unit volume
n	=	numerical constant
P	=	instantaneous porosity
$P_{unsintered}$	=	porosity of an unsintered pellet

P_0	=	porosity at the beginning of the intermediate stage sintering
p	=	numerical constant
R	=	gas constant
ρ	=	bulk density
ρ_{th}	=	theoretical density
T	=	temperature
t	=	time
t_0	=	starting time of the intermediate stage sintering
Ω	=	atomic volume

CHAPTER 1
INTRODUCTION

1.1 Problem Statement

Fume describes sub-micron aerosal particles which are part of the combustion gases in the recovery boiler, an important unit operation in the pulping process. Fume particles in the flue gas tend to form agglomerates and collect on the heat transfer surface, forming hard deposits at high temperatures. Fume deposits can cause extensive fouling of heat transfer surfaces and plugging of the flue gas passages in the boiler bank and economizer regions in the heat transfer section. With high pressure jet steam from soothblower, deposits can be knocked off regularly, but they are not always removed completely. The remaining deposits can only be removed by other methods such as high pressure water washing during a shutdown period. Loss of production during a boiler outage can cost hundreds of thousands of dollars.

Sintering has been identified as a cause of densification and hardening of fume deposits, making them hard to remove. The process itself involves complex microstructural changes and is known to be strongly dependent on many factors including sintering temperature, particle size, chemical composition of the fume, and flue gas composition. The ultimate goal of a sintering study is to understand the sintering behavior of fume deposits under various conditions. The outcome can provide useful information that is applicable to the following problems:

- prediction of fume deposits strength
- reoptimization of soothblowing scheduling
- improvement of boiler operation to reduce sinterability of fume deposits
- inhibition of the sintering process

1.2 Recovery Boiler Fundamental

The kraft recovery boiler is the most important unit operation in the kraft black liquor recovery cycle, a chemical process used to recover the chemicals used in chemical pulping. The two main objectives of the boiler are to recover the essential inorganic chemicals used in the pulping process and to utilize the energy in the organic portion of black liquor to generate steam for the pulp mill. Figure 1.1 shows a general schematic diagram of a recovery boiler.

Black liquor contains the inorganic matter dissolved from wood during chemical pulping, the residual pulping chemicals, and water. Table 1.1 contains the elemental analysis of a typical kraft black liquor. After being concentrated to 65-80% solids content, the black liquor is mixed with makeup chemicals which contain sodium-sulfur salts. The mixed fuel then undergoes combustion in the furnace section. The organic material is converted into gaseous products in a series of processes involving drying, pyrolysis, char gasification, and finally homogeneous combustion of the gases produced. The char, the residue left after black liquor pyrolysis, goes downward into the char bed which covers the floor of the furnace. The char bed is where most of the char is gasified and the inorganic compounds in the char are released and form a liquid smelt which

flows to the bottom and is tapped from the furnace through smelt spouts. The inorganic compounds are dissolved in water, converted to the active pulping chemicals, and recycled to the pulp mill.

Table 1.1 : Sample analysis of a typical kraft black liquor

Element	**wt.%**
carbon	39.0
hydrogen	3.8
oxygen	33.0
sodium	18.6
potassium	1.2
sulfur	3.6
chloride	0.6
inerts (Si, Al, Fe, Ca, etc.)	0.2

The high temperature flue gas goes upward from the furnace into the pendant heat transfer sections to generate superheated steam. The heat transfer section consists of the superheater, boiler bank, and economizer. The deposition of particles in the flue gas occurs on the heat transfer surface in these regions.

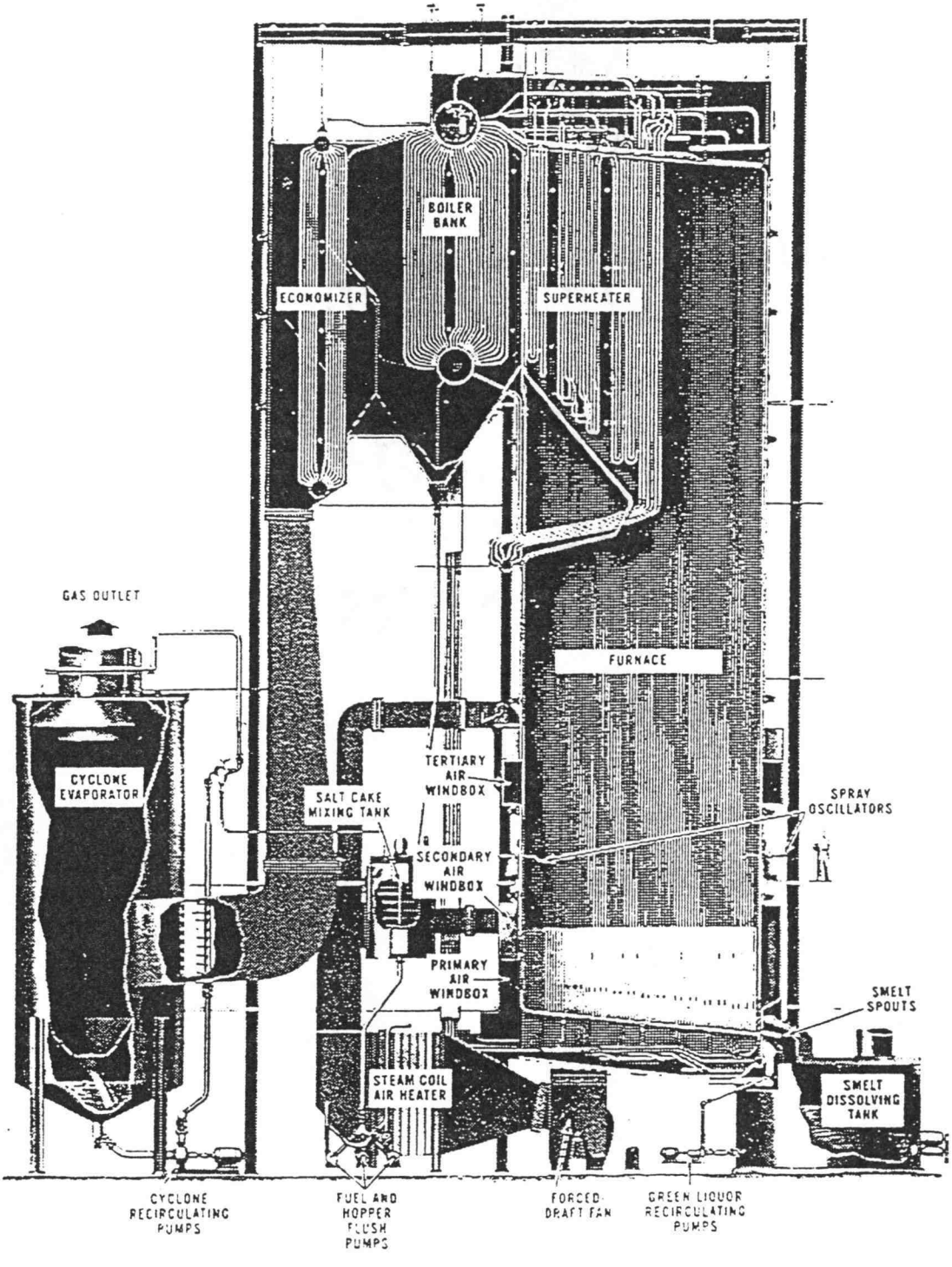

Figure 1.1 : Schematic diagram of a kraft recovery boiler

1.3 Fireside Deposits in Recovery Boiler

Deposition of sodium and potassium salt particles can cause severe problems in kraft recovery boilers. Deposits on heating surface not only reduce heat transfer effectiveness, but also cause plugging. Moreover, they also promote corrosion under an appropriate atmosphere.

Tran *et al.* has done several investigations on plugging in recovery boilers and concluded that deposition occurs by two different mechanisms[1]:

- deposition of carry-over particles
- deposition of fume particles

Carry-over particles, consisting of 20-30% of Na_2SO_4 and 60-70% of Na_2CO_3, are generated from entrained residue of black liquor droplets. They are typically 100 μm to 1 mm in diameter. They form deposits in the superheater region and boiler bank by direct impaction on the heat transfer tubes.

Fume particles, consisting mainly of Na_2SO_4, are originated from inorganic salts that are volatilized during black liquor combustion. They also contain small amount of Na_2CO_3, NaCl, and potassium salts.

After depositing, fume deposits will become hard at high temperature in a short period of time. This makes them more difficult to remove and results in plugging and long-term fouling. A study by Tran[2] reveals that dust particles, varying in size from less than a micron to a few microns, agglomerate and form necks between contact points.

This corresponds to the structural change of materials in sintering process described by Kingery[3].

1.4 Sintering Process

Sintering is a name given for a process in which the compact particles densify and form dense solid mass under high temperature. The application of the sintering process can be found largely in the field of material science. It is used in the fabrication of dense metallic and ceramic materials. Therefore, most of the effort put into this field of research aims at improving and supporting the sinterability of materials. Only a few applications are intended to retard the sintering process. One of not many examples is the study of sintering of catalyst powder in some packed-bed and fluidized-bed reactors in order to prevent reduction of the reaction surface area. In the present study, the sintering process is categorized as a source of many problems in recovery boiler operation.

1.5 Objectives

The study on the kinetics of sintering of submicron sodium sulfate has not been done before. This project, which is part of a joint study between the Department of Chemical Engineering, Oregon State University, and the Department of Chemical Engineering and Applied Chemistry, University of Toronto, focuses on the study of sintering kinetics and microstructural changes of two particular fume dusts sintered in air. The study also includes the effect of chloride species on the sintering of the two

fume dusts which contain low amount of chloride and high amount of chloride. Finally, the sintering data of low chloride fume dust will be used to develop a semi-empirical model that can predict the sintering behavior of this specific fume dust.

CHAPTER 2
SINTERING THEORY

2.1 Fundamental Knowledge

The sintering process can be defined in microscopic terms as a combining of small solid particles in contact into a single unit solid body. The system of study is a compact material containing fine grain particles being fired at high temperature close to the melting point. In order to make this section more understandable, some of the applicable terminology is defined here,

'interface' - a boundary for a condensed phase, either a solid or a liquid

'surface' - an interface which is in contact with gas atmosphere

'grain boundary' - an interface between two crystalline particles, having the same composition, in contact

'surface energy' - an amount of energy at the surface in excess of the energy of the same amount of material within the bulk

'grain-boundary energy' - an amount of energy at the grain boundary in excess of the energy of the same amount of material within the bulk

The excess free energy arises from the fact that surface atoms are more active and are at a higher energy level than those within the bulk. It can be affected by adsorbed species at the interface, atmospheric pressure, etc.

From thermodynamic point of view, the sintering process, which is thermally activated, will drive the system toward equilibrium by reducing total interfacial energy. This results in the decrease in solid-vapor surface area and increase in grain-boundary or neck area. This concept explains why a compact material with very small particle size is more easily sintered. According to the thermodynamic relation shown below (Pask)[4], equilibrium occurs when dG reaches zero,

$$dG = \gamma_{SV} dA_{SV} + \gamma_{GB} dA_{GB} \qquad 2.1$$

where dG = change in Gibb's free energy

γ_{SV} = surface energy

γ_{GB} = grain-boundary energy

dA_{SV} = change in surface area

dA_{GB} = change in grain-boundary area

Sintering process can be divided into three stages, the initial stage, intermediate stage, and final stage. Figures 2.1 shows the changes in microstructure during each stage of sintering process. The initial stage sintering, which is the least complex stage, involves inter-particle bridging. Particles in contact will start forming necks while there still is continuous open-pore channel. Neither grain growth nor a decrease in the number of voids occurs in this stage. Once the necks become larger, the void space will

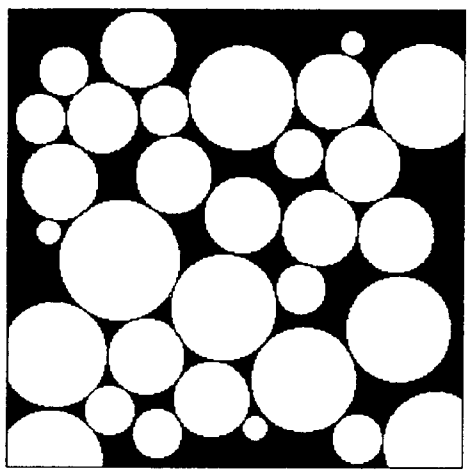

a

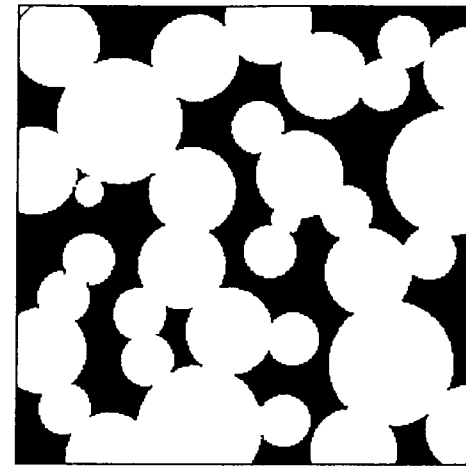

b

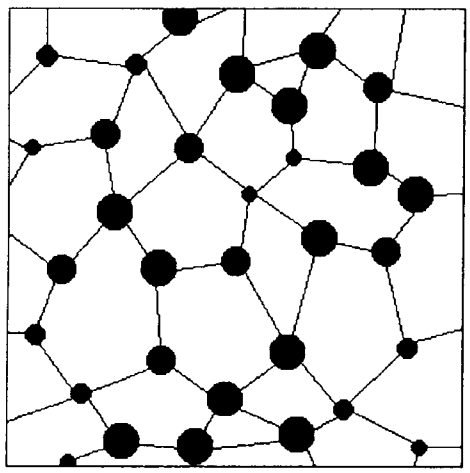

c

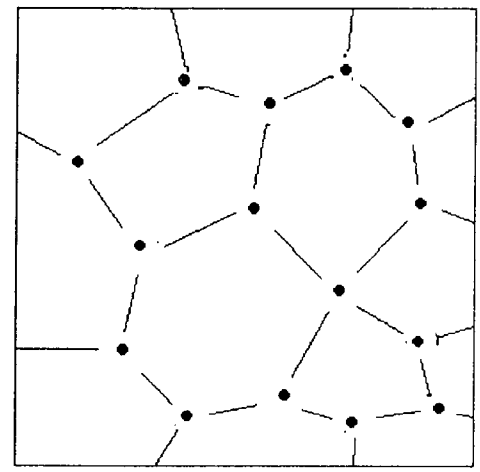

d

Figure 2.1 : Microstructural development in each stage of sintering, (a) no sintering, (b) initial stage, (c) intermediate stage, (d) final stage

become smaller. Up to some point, smaller particles will combine with larger particles and disappear, resulting in an increase in average grain-size. Some pores are trapped and there is a measurable grain growth. This is where the intermediate stage starts. The final stage occurs when all the pores are closed and only grain growth continues with the continued firing. Shrinkage or densification occurs mostly in the first two stages. In the final stage, the densification rate is extremely low. In real particle assemblages, there is no clear transition point between each stage because the compact material contains particles with a distribution of sizes and packing density.

2.2 Solid-State Sintering Models

A common objective of sintering studies is to identify the kinetics of the densification process. Even though the basic concepts of the sintering process are well understood, sintering of real particle assemblages can hardly be quantified by simple numerical models. There have been a number of sintering models proposed by ceramists and metallurgists. However, all the models were developed based on a lot of simplifications which will be described later in this chapter. Some models were applied successfully under ideal circumstances or to a specific material such as in the sintering of some monosize pure ceramic powders. Other models remain to be tested. A number of models are presented and discussed later in this chapter.

The basic mechanism of the sintering process is solid state mass transfer. In other word, sintering is a diffusion control process which involves the transport of atoms through different kinds of defects. Several types of atomic defects are vacant atom sites,

interstitial atoms or substitution of a foreign atom for a normal one, and grain boundaries. For a pure ionic or metallic compound, a sintering model can be developed by using different vacancy diffusion flux equations depending on different diffusion mechanisms. The motion of atoms from a normal position into an adjacent vacant site results in the movement of vacancies in the opposite direction. Mobility by means of this vacancy mechanism is probably the most common process giving rise to atom motion. For impure ionic species, the diffusion process is controlled by the slower diffusing species. Therefore, sintering is treated as a mass transfer due to chemical potential gradients of the constituents as recommended by Readey[5]. However, sintering of either pure or impure ionic species can result in the pores elimination process. Therefore, it is postulated here that the sintering process inevitably involves the transport of atoms through vacant sites.

As stated earlier, sintering can be divided into three stages , each of which should be treated differently. The initial stage can be described by a very commonly used two-sphere model. The intermediate stage, which appears to be the most complicated step, is treated by a totally different model which will be described later. The final stage, which does not play any role in the densification process, receives the least attention and will not be discussed here.

2.2.1 Initial Stage Sintering Models

The geometry of the initial stage sintering can be represented by two-sphere model as shown in Figure 2.2. All the arrows pointing in the direction of atom transport

represent different paths or mechanisms for mass transfer process. The driving force for the diffusion flux is the chemical potential gradient between the atom sources and sink (neck surface) or vacancy sinks and source (neck surface). The causes of the local variation in chemical potential are non-uniform surface curvature and the small stress applied at the contact point at high temperature.

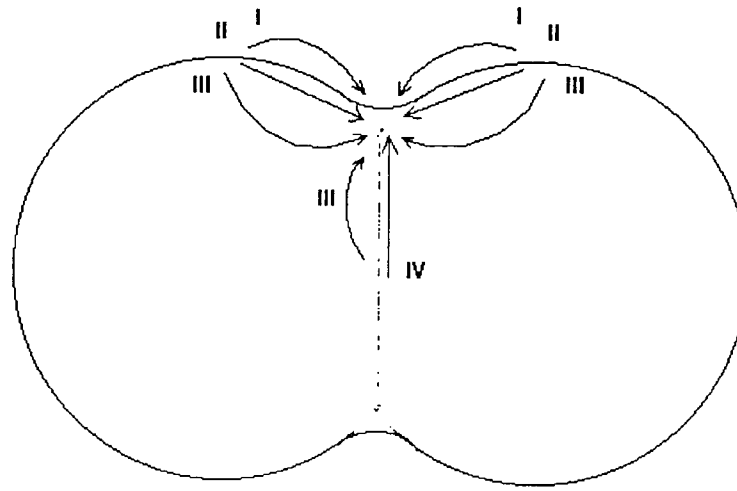

Figure 2.2 : Two-sphere model, (i) evaporation-condensation, (ii) surface diffusion, (iii) volume diffusion, (iv) grain-boundary diffusion

Grain-boundary diffusion is the mass transfer of atoms along the grain boundary to the neck surface. Volume, or bulk, or lattice diffusion is the mass transfer of atoms from grain boundary and/or spherical surface to the neck surface through the lattice structure. Surface diffusion is the mass transfer of atoms from the spherical surface to the neck surface along the particle surface. Evaporation-condensation is the recondensation of the atoms, which vaporize from the spherical surface, onto the neck surface.

In sintering of real materials, none of the mechanisms mentioned above occurs alone. In fact, all the mechanisms occur simultaneously. The problem is to figure out which of these mechanisms may dominate. Furthermore, different mechanism can have different effect on the geometry of the model as shown in Figure 2.3.

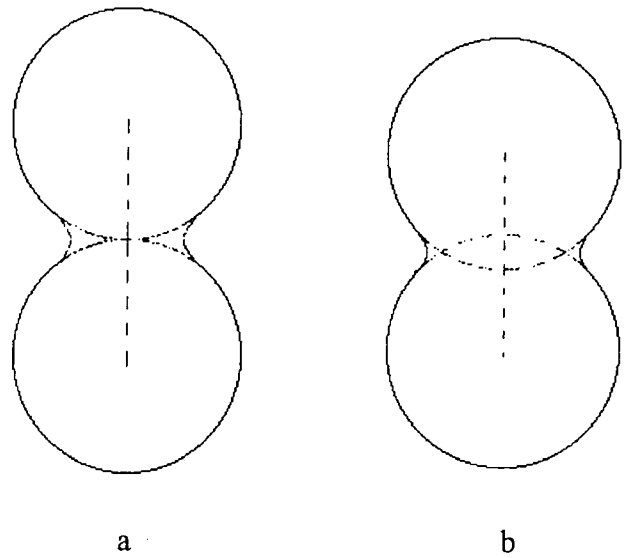

Figure 2.3 : Effects of diffusion mechanisms on the geometry of the model, (a) no shrinkage, (b) with shrinkage

In Figure 2.3.a, the interface of two spheres grows by mass filling through evaporation-condensation, surface diffusion, and volume diffusion, all with the spherical surface as a source of material. The coaxial distance between the center points of the two spheres does not change so that there is no shrinkage or densification. In Figure 2.3.b, the interface grows and the two centers move closer together at the same time. The source of material is the grain boundary itself and the paths of mass transport

are through grain-boundary diffusion and volume diffusion. In this case, densification and strength development of the compact material do occur.

A lot of models have been developed and modified from time to time. This also includes a number of computer simulations. Models in the early days were developed based on a single diffusion mechanism and a series of simplified geometry relationships. The mass transport occurs via the vacancy diffusion process. Various vacancy flux equations based on each individual mechanism were used under a number of assumptions. In this work, interest is limited to the models of sintering via volume and grain-boundary diffusion which cause the densification process. Details regarding the analytical method used to obtain the kinetic equation proposed by Johnson and Cutler[6] are explained here as an example.

2.2.1.1 Geometry

Johnson and Cutler used, as a graphical geometry, two sintering spheres of radius r with various overlap, $2\Delta r$ representing the amount of shrinkage as shown in Figure 2.4. For each value of $2\Delta r$, the volume of the double convex lens bounded by the original surfaces of the interpenetrating spheres was calculated to be equal to the volume of the annular body bounded by the neck surface and the original surfaces of the interpenetrating spheres. Johnson and Cutler assumed a series of values of ρ and, at each time, a circle of radius ρ was drawn tangent to the two circles, the area of the cross section of the annular body was measured, its centroid was determined, and the volume of the body was calculated. Successive approximations were carried out until the

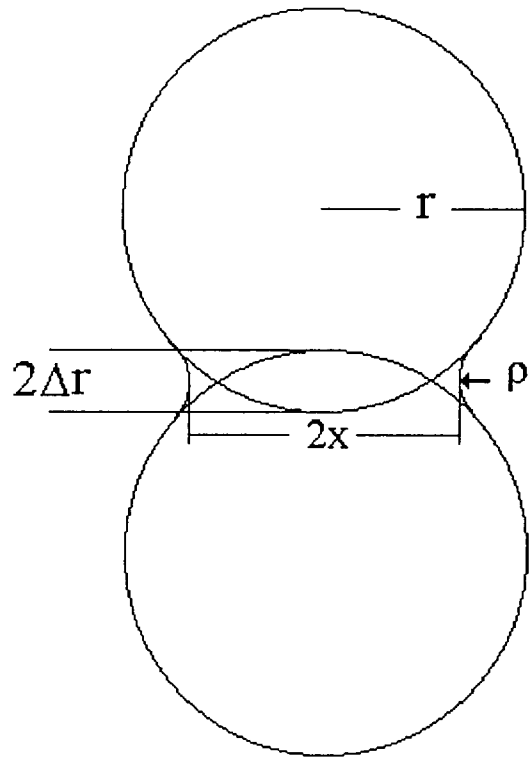

Figure 2.4 : Approaching spheres model. ρ is the neck surface radius. x is the neck half width.

volume of the annular body and the volume of the convex lens were equal and the values of ρ and x, the neck half width, were determined. The value of A, the area across which diffusion occurs in the case of volume diffusion, was also estimated. All of the geometry relationships are shown in Table 2.1 where $\Delta L/L_0$ is the relative linear shrinkage which is equal to $\Delta r/r$.

Table 2.1 : Geometry relations used in sintering models

Diffusion path	ρ	x	A
volume diffusion	$\frac{7\pi}{8} r \left(\frac{\Delta L}{L_0}\right)^{1.2}$	$\frac{5\pi}{9} r \left(\frac{\Delta L}{L_0}\right)^{0.46}$	$7\pi r^2 \left(\frac{\Delta L}{L_0}\right)^{1.5}$
grain-boundary diffusion	$\frac{7\pi}{8} r \left(\frac{\Delta L}{L_0}\right)^{1.2}$	$\frac{7\pi}{8} r \left(\frac{\Delta L}{L_0}\right)^{1.2}$	$2\pi x b$

2.2.1.2 Assumptions

- The axial section through the neck is assumed to be circular at the surface and tangential to the spherical surface.
- Grain boundary and spherical surface are assumed to have equally effective vacancy sinks.
- Only one diffusion mechanism dominates.
- For bulk diffusion model, the vacancies are assumed to diffuse with cylindrical symmetry away from the neck surface.
- For grain-boundary diffusion, the vacancies are assumed to diffuse with cylindrical symmetry within grain boundary between particles assumed to have thickness b.
- The neck geometry is maintained by surface diffusion.
- The vacancy annihilation rate is uniform, at any instant, over the entire grain-boundary area.

2.2.1.3 Modeling

The vacancy flux equations are

$$\frac{dn}{dt} = 2d_V A \frac{\Delta C}{x} \qquad 2.2$$

for bulk diffusion, and

$$\frac{dn}{dt} = 4\pi b d_{GB} \Delta C \qquad 2.3$$

for grain-boundary diffusion

where d_V = vacancy volume diffusion coefficient

d_{GB} = vacancy grain-boundary diffusion coefficient

A = neck surface area

ΔC = difference in vacancy concentration between neck surface and center of grain boundary

x = neck half width

b = grain-boundary thickness

From one of the assumptions, the vacancy concentration near the center of the grain boundary is not different from that at the spherical surface. Therefore, Kelvin's equation can be used to relate ΔC to ρ as follow,

$$\frac{\Delta C}{C_0} = \frac{\gamma\Omega}{kT}\left(\frac{1}{\rho} - \frac{1}{x}\right) \qquad 2.4$$

$$\cong \frac{\gamma\Omega}{kT\rho} \qquad 2.5$$

when x is much larger than ρ

where C_0 = vacancy concentration under a flat surface

γ = surface energy

Ω = vacancy volume

k = Boltzman's constant

T = absolute temperature

Substituting eq.(2.5) together with the geometric relations from Table 2.1 into eq.(2.2) and eq.(2.3) results in equation in the following form.

$$\frac{\Delta L}{L_0} = \left[\frac{K\gamma\Omega D}{kTG_0^p}\right]^n t^n \qquad 2.6$$

where $\Delta L/L_0$ = relative linear shrinkage

D = self diffusion coefficient

= $\Omega C_0 d_V$

= D_V for volume diffusion

= $\Omega C_0 d_{GB}$

	=	D_{GB} for grain-boundary diffusion
G_0	=	grain size
n,p,K	=	numerical constants
t	=	time

All the numerical constants are shown in Table 2.2. This form of kinetic equation, which is written for a small segment of the total structure, represents the geometrical changes of the total structure by assuming that the compact material contains monosize particles and has reasonably dense packing. Other models have a similar form of equation, but different numerical constants depending on applied geometry relations and vacancy flux equations. All the numerical constants for different models are also shown in Table 2.2. Details regarding the formulation of these constants can be found in the references.

Table 2.2 : Numerical constants for initial stage sintering model

Controlling mechanism	K	n	p	Reference
volume diffusion	3.141	0.46	3	Johnson and Culter[6]
	14.142	0.4	3	Kingery and Berg[7]
	2	0.5	3	Coble[8]
grain-boundary diffusion	$2.274G_0$	0.31	4	Johnson and Culter[6]
	$15G_0$	0.33	4	Coble[8]

All the models presented previously are based on the assumption that there is only one mechanism dominates. When there are more one mechanism occur simultaneously, the vacancy flux equation is changed correspondingly. With the grain boundary as a vacancy sink, Johnson and Clark[9] used a vacancy flux equation by assuming the concurrent grain-boundary and volume diffusions. The simultaneous mechanism model was derived as shown below,

$$\left(\frac{\Delta L}{L_0}\right)^{2.1}\frac{d(\Delta L/L_0)}{dt}=\frac{2\gamma\Omega D_V}{kTG_0^3}\left(\frac{\Delta L}{L_0}\right)+\frac{\gamma\Omega bD_{GB}}{2kTG_0^4} \qquad 2.7$$

Johnson[10] also developed a new concept in modeling by using the atom flux equation. He successfully developed a model based on mass transport of active chemical species. He no longer used the concept of the vacancy flux diffusion as a basis to explain the kinetic of sintering process. Instead, he used the chemical potential gradient between the source and the sink of material as a key to define the equation of atom flux as shown below. All the terms in the parenthesis are the geometrical terms.

$$j=4\gamma B_a\left(\frac{x+\rho\cos\alpha}{\rho x^2}\right) \qquad 2.8$$

where B_a is the atomic mobility and j is atom flux per unit area. By substituting the apparent diffusion coefficient $D_{app} = B_akT$, we can rewrite eq.(2.8) as shown below,

$$j=\frac{g\gamma}{kT\rho}D_{app} \qquad 2.9$$

where g is the group of geometrical terms. This equation agrees well with the atom flux equation proposed by Readey[5] in a study on mass transport and sintering in impure ionic solids.

Using eq.(2.8) and some geometrical relations, Johnson came up with the concurrent grain-boundary and volume diffusions sintering model as follows:

$$\left(\frac{\Delta L}{L_0}\right)^{2.06} \frac{d(\Delta L / L_0)}{dt} = \frac{2.63\gamma\Omega D_V}{kTG_0^3}\left(\frac{\Delta L}{L_0}\right) + \frac{0.7\gamma\Omega b D_{GB}}{kTG_0^4} \qquad 2.10$$

It can be seen that the general form of the model is very similar to the vacancy flux based model. However, Johnson[10] claimed that not only the effect of impurities, but also the effect of the ambient atmosphere can be determined with confidence.

Speculation reveals that all the vacancy flux equations used in the derivation of the earlier models[6,7,8,9] are also comparable with eq.(2.9) when self-diffusion coefficients D_V and D_{GB} are changed to the apparent diffusion coefficient D_{app}. In addition, all the vacancy flux based models have the same form as the models developed by the atom flux concept. Thus, it is postulated here that all the models in the form of eq.(2.6) are applicable to the multicomponent system. However, estimation of diffusion coefficient of atomic species of interest is not recommended because the apparent diffusion coefficient D_{app} includes the contributions from several diffusion paths into one net diffusion coefficient.

All the models presented so far do not take into account the effect of surface diffusion which was thought to have no effect on the densification rate. Not long ago

have attempts been made to account for the effect of mass transfer from the surface on the densification rate. Gessinger[11] pointed out that grain-boundary diffusion can be limited by the redistribution rate of material from the neck over the spherical surface. Johnson[12] agreed with the concept, but further explained that redistribution can occur either through surface diffusion or volume diffusion, depending on temperature and particle size. However, neither of them came up with a final model based on the chemical potential gradient between the source and sink of material. It was Wong and Pask[13] who first developed models which take into account the effect of surface diffusion. The models, each for a different controlling mass transfer mechanism, are shown here.

- Densification rate is controlled by the redistribution rate of material from the neck to the surface

$$P - P_o = \left[\frac{-A_1 D_V \Omega \gamma N_1^3}{kT}\right](t - t_0) \qquad 2.11$$

- Densification rate is controlled by the rate of material moving from grain boundary to the neck region

$$\frac{1}{P^{0.5}\left(0.60 + 0.17P^{0.5} - 0.12P\right)}\frac{dP}{dt} = \frac{-A_2 D_{GB} b \Omega \gamma N_1^4}{kT} \qquad 2.12$$

where P = porosity at time t

P_0 = porosity at time t_0

t_0 = time at which initial stage sintering ends

A_1 = numerical constant

A_2 = numerical constant

N_1 = number of interconnected voids per unit volume

Other researchers whose studies have been cited, but not yet evaluated, are Swinkels and Ashby[14] who proposed a complete analytical model combining grain-boundary diffusion and surface redistribution, Exner[15] who performed the computer simulation of the exact shape of the neck when grain-boundary and surface diffusion occur simultaneously by normalizing all the physical terms. He came up with the upper and lower limit of grain-boundary and surface diffusivity ratio which predict the densification behavior. Due to the laborious formulations of these models, they are used in the advance sintering study only.

2.2.2 Intermediate Stage Sintering Models

For intermediate stage sintering, not many models have been proposed. Surprisingly, this stage of sintering represents the major part of the densification, especially when the initial stage happens in a short period. Coble[16] firstly developed models based on a different concept from initial stage sintering modeling. He represented a compact structure built up by tetrakaidecahedron shape particles connecting side by side. Figure 2.5 shows a single tetrakaidecahedron.

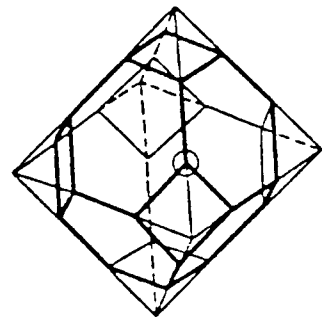

Figure 2.5 : Tetrakaidecahedron formed from truncated octahedron[16]

Again, the vacancy diffusion flux concept was utilized. Applying the volume flux equation together with some geometrical analysis, Coble came up with models predicting porosity change with time as shown below,

$$P = \left[\frac{2D_{GB}b\gamma\Omega}{G^4kT}\right]^{2/3} t^{2/3} \qquad 2.13$$

for grain-boundary diffusion control, and

$$\frac{dP}{dt} = \frac{-720D_V\gamma\Omega}{G^3kT} \qquad 2.14$$

for volume diffusion control.

2.3 Grain Growth

As previously mentioned, grain growth is the major phenomenon in the final stage of sintering. Even though grain growth has very little effect on the densification process in the final stage sintering, the phenomenon is worth mentioning about since it involves a critical microstructural change. In addition, the intermediate stage sintering involves a degree of grain growth which can retard the densification rate.

All the grain boundaries are in equilibrium when they form angles of 120^0. To meet this condition, each grain must have six identical straight sides on two-dimensional plain. Grains with fewer sides have concave boundaries which tend to move to their center of curvature toward the center of the grains, resulting in smaller grains. Grains with more than six sides have boundaries which tend to move away from the center of the grain toward their center of curvature, resulting in larger grains. The process occurs in order to reduce the total grain-boundary energy and drive the system into equilibrium. Figure 2.6 shows the concave boundaries movement.

A pore, which is classified as a second phase inclusion, can reduce the grain-boundary velocity because it increases the energy necessary for the migration of the grain boundary. When a number of pores are present at a grain boundary, four possible mechanisms can take place as follows,

- Grain-boundary energy is insufficient for continued grain growth.
- Pores are so immobile that the grain boundary moves past them, trapping a pore inside the grain.

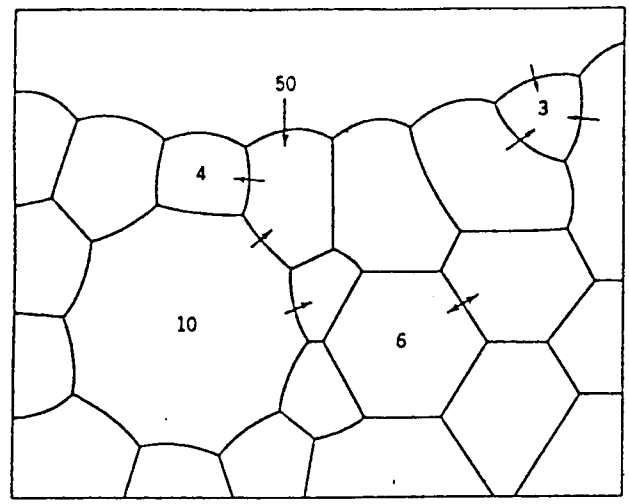

Figure 2.6 : Grain-boundary movement (Kingery)[3]

- Pores move along with boundary, causing little resistance.
- Pores move along with boundary with the inclusion mobility controlling the boundary movement.

The last two phenomena can cause the agglomeration of pores into a larger pore as shown in Figure 2.7. An increase in pore size can reduce the driving force for grain-boundary movement greatly, resulting in grain growth inhibition.

In addition to the curvature of the grain boundary that causes the boundary movement, differences in the crystalline structure of two opposing surfaces at an interface is also a driving force for boundary movement. In order to lower the

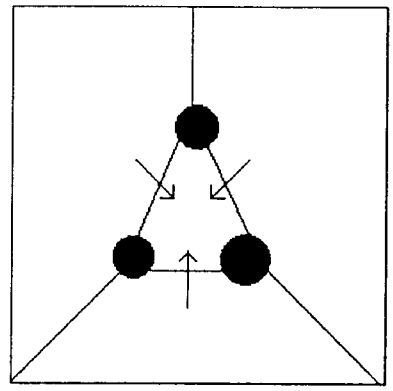

Figure 2.7 : Pore agglomeration by grain-boundary movement

grain-boundary energy, the system tries to rearrange the crystallinity of each interface into the same alignment, resulting in the jumping of atoms across the grain boundary and boundary movement.

The kinetics of grain growth can usually be described by the following equation (Yan *et.al.*)[17],

$$G^N - G_0^N = m_0 e^{-\left(\frac{E_G}{RT}\right)}(t - t_0) \qquad 2.15$$

where G = instantaneous grain size at time t

G_0 = initial grain size at time t_0

m_0 = a numerical constant

E_G = activation energy of grain growth process

N = grain growth kinetic exponent

2.4 Activated Sintering

In the field of material science, sintering is a novel technique in fabricating metallic or ceramic materials from metallic or ceramic powders utilizing the solid state thermodynamic concept. The ultimate goal is to achieve the theoretical density or the density of the dense solid particle. An effective way to improve the sinterability of the compact powders is to reduce the particle size of the raw material in order to increase the total surface area, the driving force for the sintering process. Unfortunately, the densification rate can be retarded by on-going grain growth which causes both pore entrapment and reducing in total surface area. The use of additives has proved to be one of the most effective ways to improve the sinterability and prevent grain growth. Although many mechanisms can be predicted for the function of additives, it is still very hard to apply each hypothesis to the experimental results because of the limitation in analytical techniques. Nonetheless, Brook *et al.*[18] proposed two groups of mechanisms together with some illustrations for the function of additive as shown in Figure 2.8 and 2.9. The first group is for the mechanisms of additives that act as second phase by

- providing a high diffusivity pathway, e.g. liquid phase, along the grain boundary (mechanism iii, Figure 2.8)
- providing a low diffusivity pathway for the diffusion across the boundary which then retards grain-boundary migration (mechanism 6, Figure 2.9)

The second group is for the mechanisms of additives that act as a solid solution by

- promoting diffusivity of the controlling species in the lattice structure or along the grain boundary by affecting the point of defect concentration in the boundary or lattice structure (mechanism ii or iii, Figure 2.8)
- retarding grain-boundary migration by forming a segregated layer at the boundary which has to be pulled along by the boundary (mechanism 7, Figure 2.9)
- changing the driving force for sintering by changing the ratio of grain-boundary energy to free surface energy
- slowing the atom diffusion across the boundary which then retards grain-boundary movement (mechanism 6, Figure 2.9)

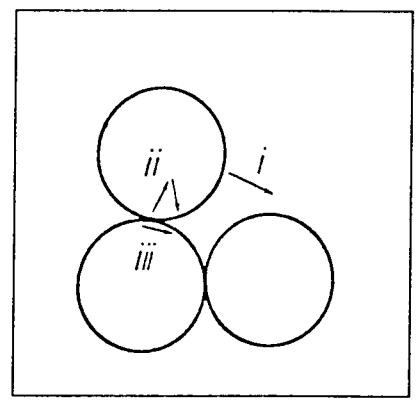

Figure 2.8 : Densification mechanisms during sintering, (i) particle rearrangement, (ii) volume diffusion, (iii) grain-boundary diffusion

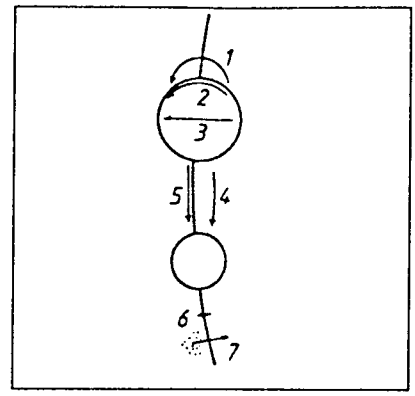

Figure 2.9 : Mechanisms for the control of boundary migration and hence for control of grain growth during sintering. (1) pore movement by volume diffusion, (2) pore movement by surface diffusion, (3) pore movement by vapor transport, (4) pore coalescence by volume diffusion, (5) pore coalescence by boundary diffusion, (6) intrinsic boundary movement, (7) impurity drag

Brook *et al.* suggested that an additive introduced in an amount close to the solid solution limit will maximize the extent of modification of the defect chemistry. It is further postulated here that an excessive amount of additive will act like a non-densifying inclusion, thus slowing the densification rate and reducing the sinterability. In contrast, too little amount of additive will not activate the sintering process effectively.

CHAPTER 3
LITERATURE STUDY

3.1 Application of Sintering Models

All the application of sintering models fall in the study of metallic and ceramic materials.[6,7,8,9,10,16] For alkali salts, such as sodium sulfate, whose application in the field of material science is extremely rare, there has never before been any study on the kinetics of sintering.

It is also important to mention here about Johnson's critical assessment on the application of kinetic models for the sintering process[19]. He stated that sintering mechanisms can hardly be identified by the time dependence of shrinkage of powder compacts, especially in the case of sub-micron ceramic particles. The major reason is that all the models were developed based on a number of assumptions of questionable validity which have been mentioned earlier. However, he also added that these equations may be useful once adjusted and applied to sintering of specific materials.

3.2 Fume Formation

Jokineimi *et al.*[20] has successfully developed a numerical model for fume formation that can predict fume particle size distribution and chemical composition. The mechanisms they used as a basis for model development are shown together with Figure 3.1 as follows,

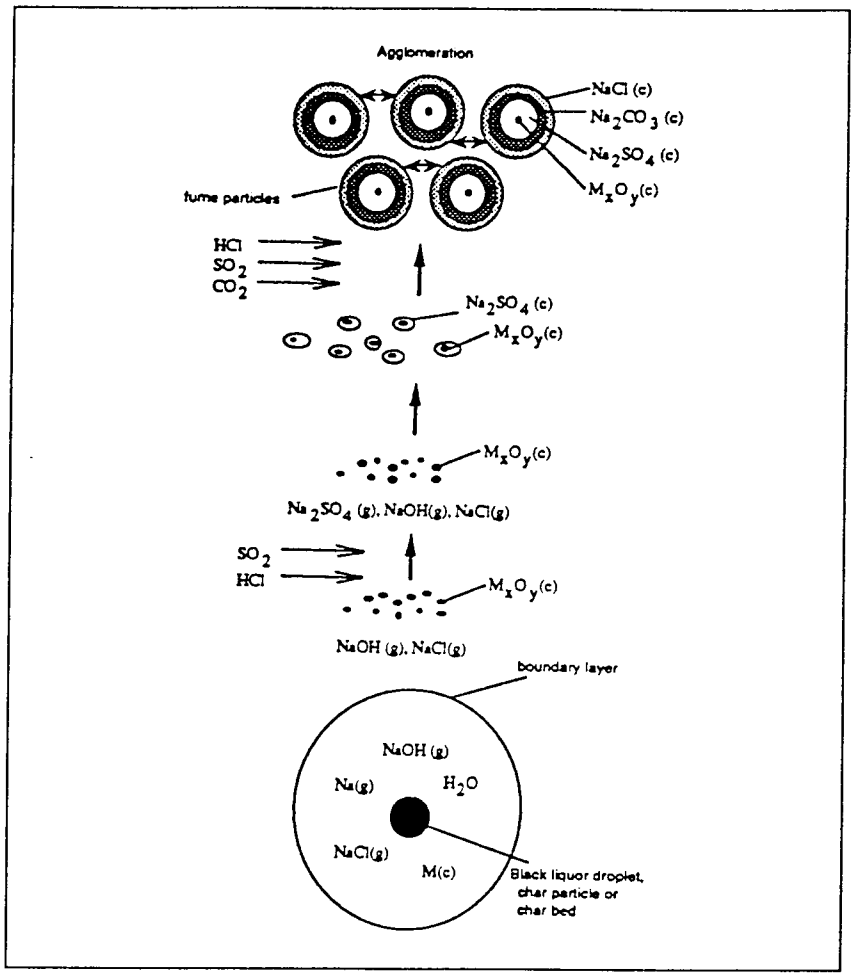

Figure 3.1 : Fume formation mechanisms in the presence of metal oxide seeds (M = metal, M_xO_y = metal oxide, g = gas, c = condensed)[21]

a) All volatilized Na and K exist firstly as hydroxides and chlorides in the flue gas, vaporized by three possible mechanisms : (1) released during the pyrolysis of black liquor droplets before entering the char bed, (2) volatilization of char bed smelt, (3) released from carryover particles during pyrolysis and char burning.

b) The reactions of Na, K, NaCl, and KCl with gaseous H_2O, CO_2, CO, O_2, H_2S, SO_2, OH and HCl take place rapidly, forming NaOH, KOH, NaCl, KCl, Na_2SO_4 and K_2SO_4.

c) Alkali hydroxides and chlorides are converted to sulphates by reactions with SO_2.

d) Due to the very low vapour pressures, sodium and potassium sulphates condense rapidly after formation by three possible mechanisms : (1) homogeneous nucleation of sulphates species, (2) condensation of gaseous sulphates directly on tiny metal oxide particles forming during black liquor combustion, (3) reaction of gaseous sulphates promptly with metal oxide forming a condensed phase on the surface.

e) When there is not enough SO_2, alkali hydroxides and chlorides react with gaseous CO_2 and H_2O to form Na_2CO_3 on the surface.

f) At lower temperatures, alkali chlorides condense directly onto particle surfaces.

3.3 Sintering of Fume Particles

Tran *et al.*[2] investigated sintering of fume particles by using pellets made from precipitator dusts, particles collected from the flue gas in the precipitator of a kraft recovery boiler. They concluded that the minimum temperature for the sintering of fume dusts is about 300 ^{0}C. In the same study, they also ran a series of isothermal sintering tests by measuring volume shrinkage and density change with time for sintered dust pellets. They concluded that the rate of sintering increases with temperature. However, they did not attempt to fit the experimental data to a sintering model. Also, they did not interpret the microstructural development and did not apply the concept of grain size

evolution to the modeling of sintering kinetics. Originally, part of this current project involved the modeling of their available sintering data. Due to insufficient amount of data, it was not possible. In spite of that, their study provide an excellent basis on which to begin the present work. The modeling of Tran's data is shown in Appendix B.

For the effect of dust chemical composition, Skrifvars and Hupa[21] have done an excellent study on the sintering of recovery boiler dusts and synthetic dusts of various chemical composition. They focused mainly on the strength measurement of specimens sintered to a steady state at different temperature. Their work showed that chloride content has significant effects on the sinterability of synthetic dusts, and that potassium, to lesser degree, also has some effects on the sintering of synthetic dusts. For their boiler dusts, no conclusion about the effect of impurities can be drawn due to the number of uncontrolled factors during their experiments. They did not consider the kinetics of sintering in their work.

CHAPTER 4
EXPERIMENTAL METHODS

4.1 Materials

The materials used in this experiment are dusts collected from the electrostatic precipitators of two kraft recovery boilers. One dust contains a low amount of chloride while the other contains a large amount of chloride. The compositions distributed by ionic species for these two dusts were previously analysed and are shown in Table 4.1 below.

Table 4.1 : Chemical compositions as weight percent of the two precipitator dusts

Dust sample	Na^+	K^+	Cl^-	SO_4^{2-}	CO_3^{2-}	Total (%wt)
low chloride	26.0	9.9	2.2	58.6	3.1	99.8
high chloride	29.9	5.9	13.5	43.6	4.9	97.8

4.2 Equipment

All the equipments used in this experiment are listed as followed,

Furnace # 1 - The muffle furnace used was Cenco-Dekhotinsky furnace. The maximum operating temperature in the experiment was 200 ^{0}C.

Furnace # 2 - The muffle furnace used was NEYTECH 185P furnace. The maximum operating temperature in the experiment was 550 ^{0}C.

Chronometer - The timing watch used was a TAG-HEUER automatic model.

Thermocouple - The thermocouple used was a K-type chromel-alumel thermocouple with the temperature range -200 to 1000 ^{0}C.

Temperature Controller - The temperature controller used was a digital temperature controller.

Pellet Holder - The pellet mold or block used was an metal block with 1-inch inside diameter. It had a cylindrical shape. It also contained a 1-inch diameter cylindrical piston and a 1-inch diameter cylindrical stopper. The general design is shown in Figure 4.1 below.

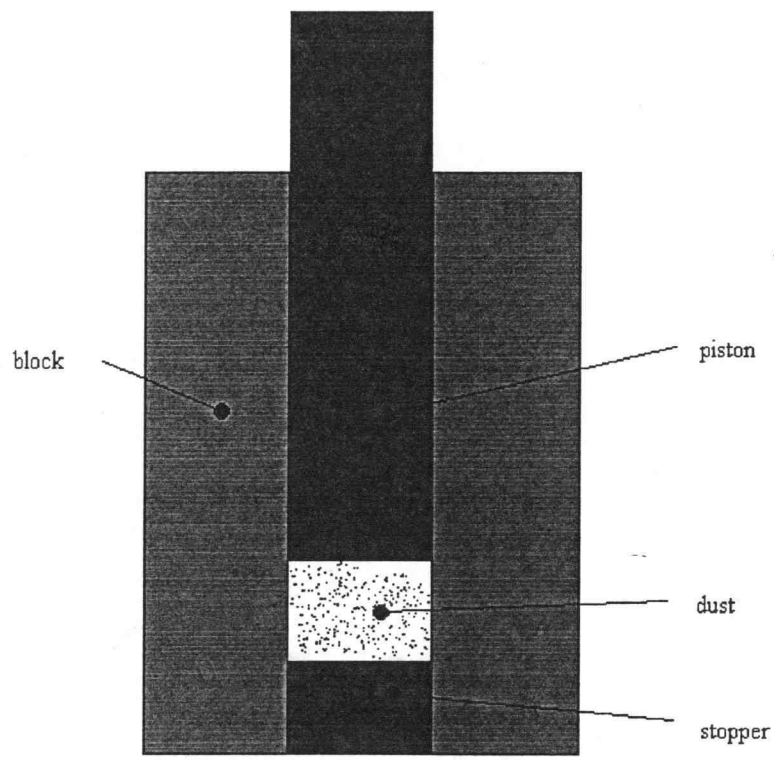

Figure 4.1 : Pellet holder

Press - The press used was a Carver laboratory press model C.

Ceramic Plate - The ceramic plate used was an alumina ceramic plate.

Micrometer - The micrometer used had an accuracy within 0.005 mm.

Calipers - The calipers used had an accuracy of 0.005 inch.

Balance - The balance used was a Mettler AE260 analytical balance.

SEM - The scanning electron microscope used was a Hitachi S-570 scanning electron microscope. Gold was used as a coating film for the sample analyses.

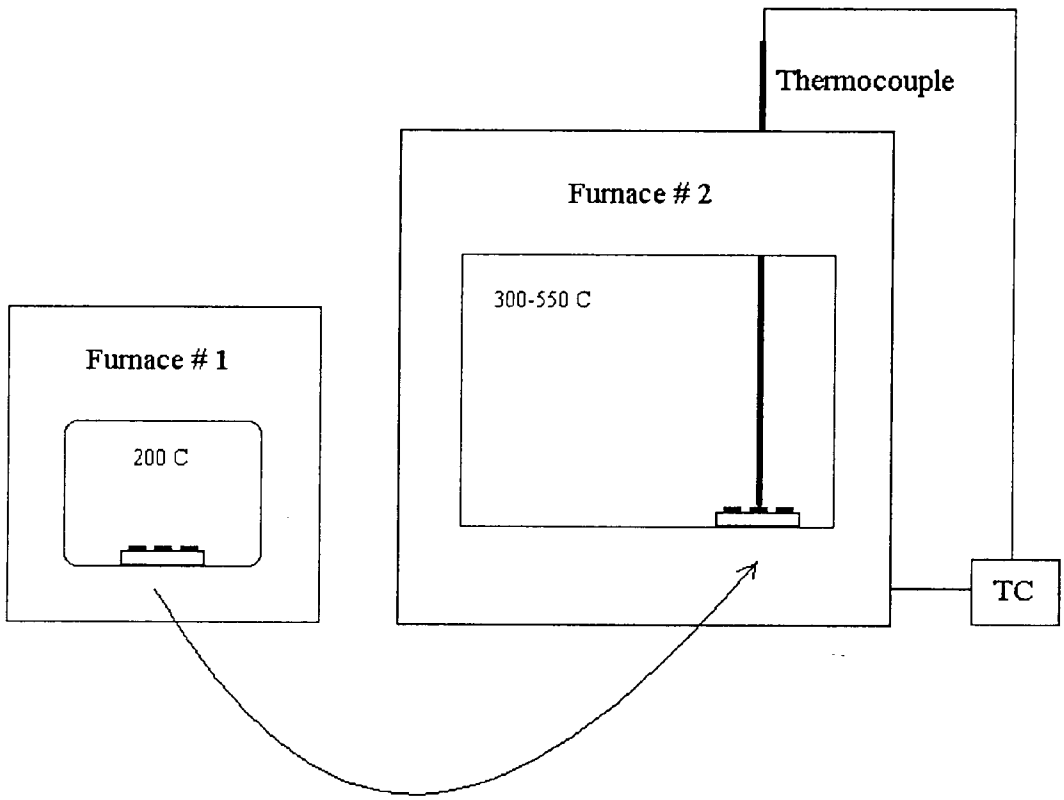

Figure 4.2 : Experimental setup

4.3 Experimental Procedure

4.3.1 Pellet Making

- Fill the pellet mold with approximate 3 g of precipitator dust. Shake the pellet mold well.
- Put the pellet mold into the chamber of the press. Apply maximum pressure which does not cause lamination in the pellet. If the applied pressure is too high, a pellet will separate into layers. The optimum pressure is the pressure that produces less than 20% bad pellets.
- Measure the thickness of a pellet by micrometer. Measure the mass of a pellet in the balance. The diameter of a pellet was fixed at 1 inch by the inside diameter of the pellet holder. Typical values for applied pressure are 2500 psi for low chloride dust and 500 psi for high chloride dust. The average density of a fresh pellet made from low chloride dust was 1.43 g/cm^3. The average density of a fresh pellet made from high chloride dust was 1.17 g/cm^3.

4.3.2 Sintering Test

- Put three pellets on the ceramic plate.
- Preheat the pellets in furnace # 1 at 200 ^0C for 1 hour. This temperature was low enough that there was no sintering at all.
- Preheat furnace # 2 to the sintering temperature.

- Quickly remove the ceramic plate from the furnace # 1 and put it into the furnace # 2 at a fixed location where the thermocouple touches the top of the middle pellet. Start timing after the pellets were heated up to the sintering temperature again as indicated by the thermocouple in contact with the center pellet. The heat-up time was about 2-3 minutes. The complete diagram of the experimental setup is shown in Figure 4.2.
- Take the ceramic plate out of the furnace # 2 once the desired sintering time is reached. Let the sintered pellets cool down at room temperature.
- Randomly measure the thickness of each pellet three times at different point on the surface using micrometer. Record the average value. Randomly measure the diameter of each pellet three times at different point on the circumference using callipers. Record the average value. Measure and record the mass of each pellet.
- Keep all the sintered pellets for morphology study.
- The sintering temperature and time schemes for both dusts are shown in Table 4.2.

Table 4.2 : Sintering temperature and time schemes

Dust sample	Temperature (^{0}C)	Initial density (g/cm^3)	sintering time (min)
low chloride	300	1.43	60,120,240,480*
	350	1.43	15,20,30,45,60,90,120,180,480*
	400	1.43	0,5*,7,10*,15,20,30*,45,60*,120,480*
	450	1.43	0,3*,4,5,7*,10*,15*,20,30*,60*,480*
	450	1.36	0,5,10,15,30,60
	450	1.19	0,5,10,15,30,60*
	450	0.88	0,5,10,15,30,60
	500	1.43	0,1,2,3*,5*,7,10*,15,30,60,120,240,480*
	550	1.43	30
high chloride	350	1.17	30,60,120,240,480
	400	1.17	0,5,10,15,20,30,60,120,480
	450	1.17	0,5,7,10,15,30,60*,480
	500	1.17	0,5,7,10,30,480
	550	1.17	30

(Note : The times marked by asterisk (*) were used for the microscopic analyses)

CHAPTER 5
RESULTS AND DISCUSSION

5.1 Side Reaction During Sintering

The majority of the component in dust particles is the sulfate species which is the most stable form of sulfur oxides. Therefore, oxidation of these species should not take place. The reaction of chloride and carbonate species with the surrounding gas can occur only if there is sulfur dioxide presented. However, this gas was not added during the experiments. The weight loss of each sintered pellet was extremely low, with an average weight loss of about 0.2% and a maximum weight loss of 0.5%.

5.2 Reproducibility

Reproducibility is justified from the standard deviation of the density values of pellets sintered at the same temperature under the same period of time. At least three pellets were used for each sintering temperature and time. The maximum number of pellets for specific sintering temperature and time is eight. These sintered pellets were obtained through three identical sintering runs. Table 5.1 shows that reproducibility is acceptable. The density of these pellets before the sintering tests was roughly equal to 1.43 g/cm^3 for the pellets made from the low chloride dust and 1.17 g/cm^3 for the pellets made from the high chloride dust.

Table 5.1 : Reproducibility testing

Dust sample	Sintering temperature (^{0}C)	Sintering time (min)	Number of samples	Average density (g/cm^3)	Standard deviation
low chloride	500	1	5	1.837	0.050
low chloride	500	2	5	2.085	0.026
low chloride	500	3	5	2.181	0.029
low chloride	500	7	6	2.444	0.009
low chloride	500	480	6	2.485	0.012
low chloride	450	60	8	2.465	0.013
low chloride	400	30	7	2.086	0.030
low chloride	400	480	6	2.420	0.025
high chloride	450	30	5	2.007	0.058

5.3 Temperature Effect

From the experimental data, the density of each sintered pellet was calculated from volume and mass. The isotherms of density versus time are shown in Figures 5.1 and 5.2 for low chloride and high chloride dusts respectively. As expected, the densification rate and the sinterability or final density increase as the sintering temperature increases. This is in agreement with the sintering theory mentioned earlier that the process is thermally activated. The results also confirm the conclusion drawn by Tran *et al.*[1].

For both dusts, the densification rate is extremely low at low sintering temperatures, as is the final density. The lowest temperatures at which sintering was

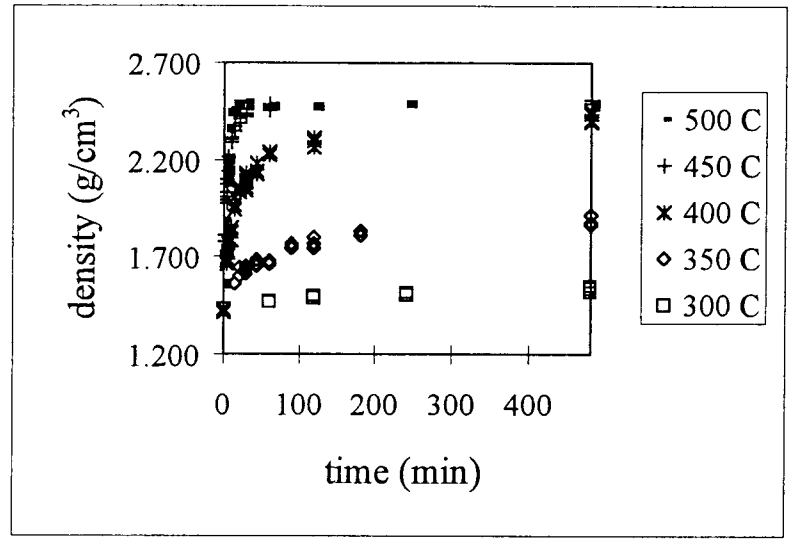

a

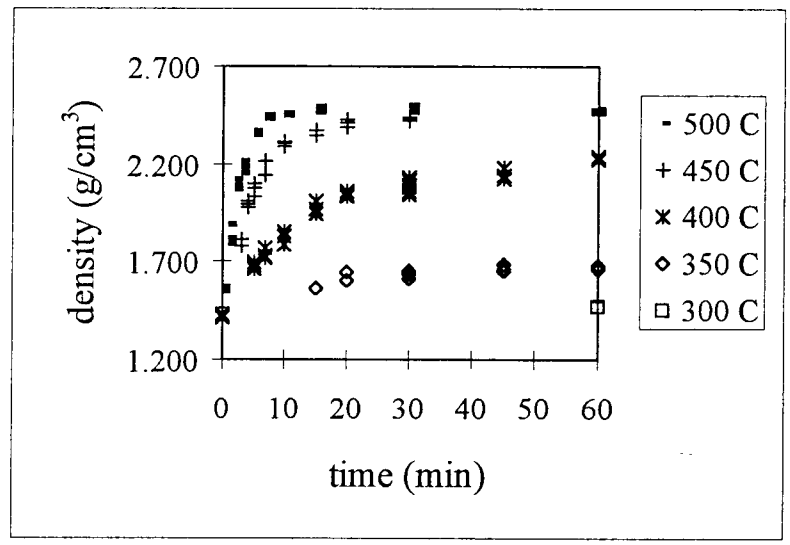

b

Figure 5.1 : Isotherms of density change with time for low chloride dust, (a) scale 0-480 min, (b) scale 0-60 min

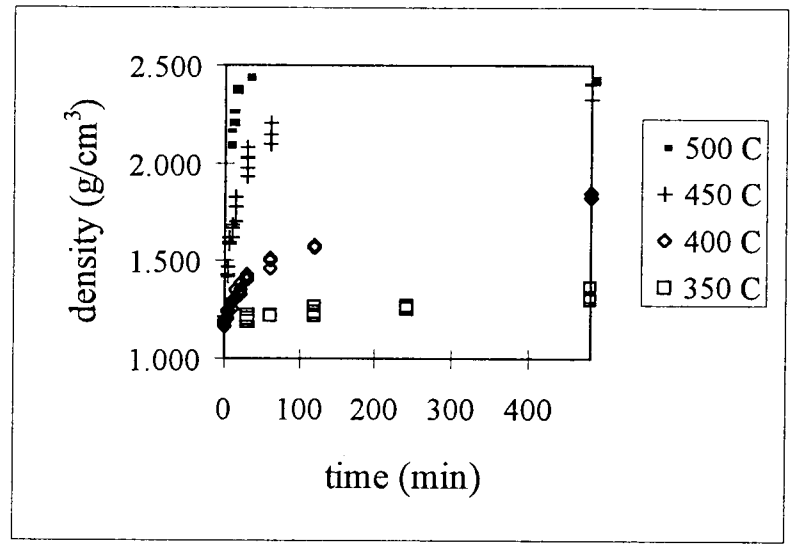

a

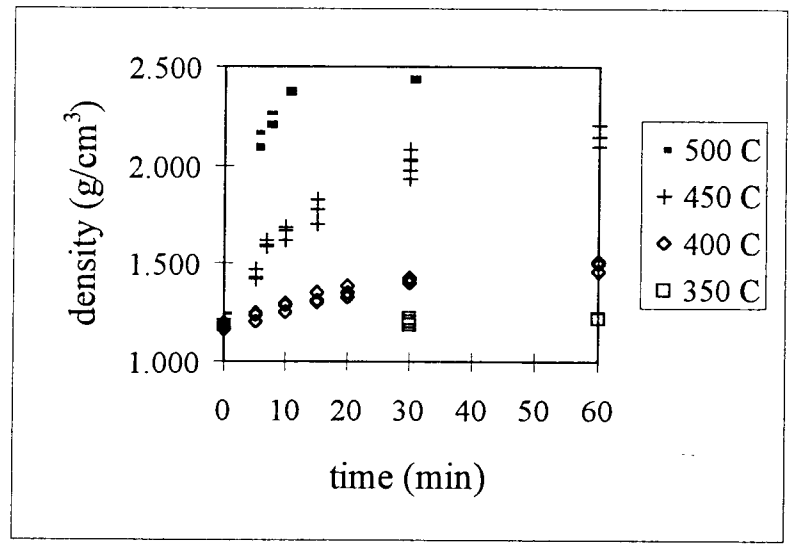

b

Figure 5.2 : Isotherms of density change with time for high chloride dust, (a) scale 0-480 min, (b) scale 0-60 min

observed were 300 ^{0}C for low chloride dust and 350 ^{0}C for high chloride dust. No significant sintering occurs at temperature below 400 ^{0}C. The sintering rate becomes very fast at temperature above 400 ^{0}C. For both dusts, the pellet samples reach the final density in less than 15 minutes when sintered at 500 ^{0}C. At higher temperature, the final density is independent of the sintering temperature. The final density of pellets sintered at 500 ^{0}C is very close to that of the pellets sintered at 450 ^{0}C. At 400 ^{0}C, 450 ^{0}C, and 500 ^{0}C, some amount of sintering had already taken place during heat-up time before the pellet sample reached the desired temperature. Therefore, the recorded density values at time zero for these temperatures are higher than the density of a fresh pellet. At lower temperature, no sintering was detected during the heat-up time.

The upper limit for sintering temperature is defined by the fact that the material will begin to melt at a certain temperature. The existence of liquid phase at temperature above the first melting point will result in a different densification mechanism which is beyond the scope of our study. A few observations were made to verify the upper limit as follows,

- From the phase diagram of Na_2SO_4-K_2SO_4-NaCl-KCl system (see Appendix C), the first melting point is at 518 ^{0}C.
- The final density of pellets sintered at 550 ^{0}C is less than that of pellets sintered at 500 ^{0}C. The result is shown in Table 5.2. This indicates that some pores are trapped when the particles begin to melt.

Table 5.2 : Comparison of final density of pellets sintered at 500 ^{0}C and 550 ^{0}C

Dust sample	**Average final density (g/cm^3)**	
	500 ^{0}C	550 ^{0}C
low chloride	2.488	2.202
high chloride	2.437	2.396

- The SEM picture of a pellet (low chloride dust) sintered at 550 ^{0}C for 30 minutes shows many large round pores occurred by pore agglomeration through liquid-phase media along the grain boundary (see Figure 5.3). The air trapped in these pores is not soluble in the liquid phase. Therefore, it could not diffuse out through the grain boundary during sintering, resulting in a more porous pellet.

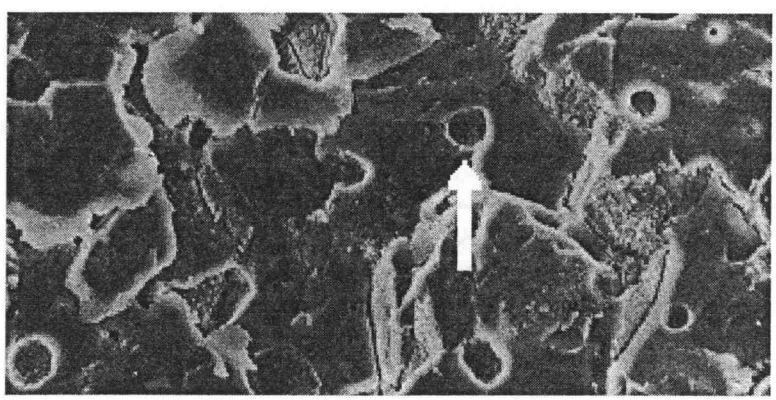

Figure 5.3 : SEM picture of a pellet (low chloride dust) sintered at 550 ^{0}C for 30 minutes. Scale bar is 100 μm. The arrow points to a rounded pore.

5.4 Microstructural Development

SEM pictures of both kinds of precipitator dusts prior to sintering are shown in Figure 5.4 below. Both dusts have the same average particle size which is about 0.5 μm.

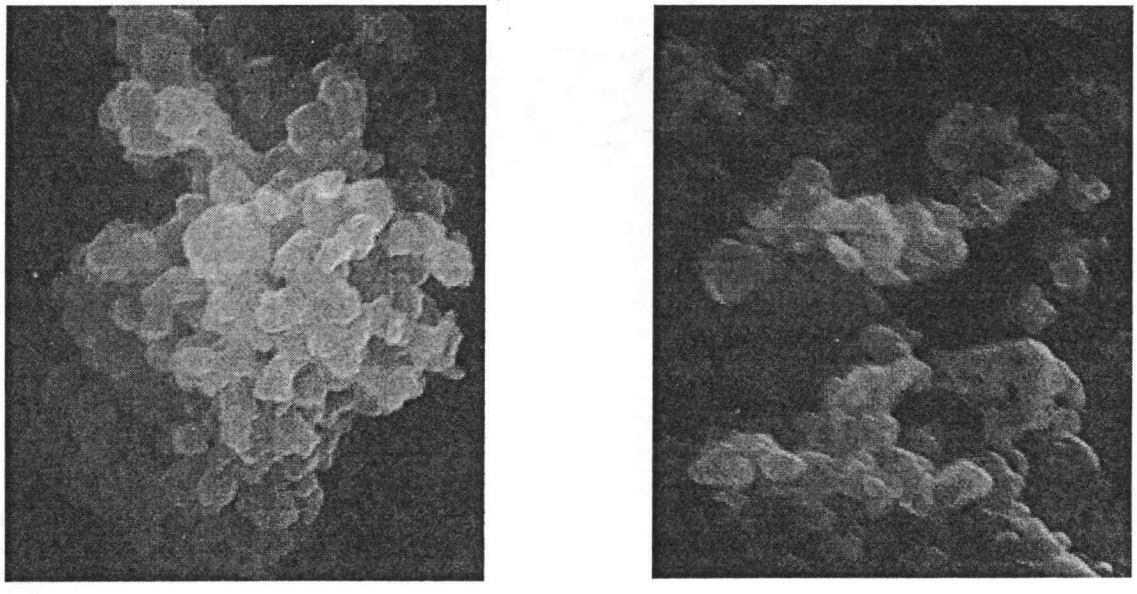

a b

Figure 5.4 : SEM pictures of precipitator dusts, (a) low chloride dust, (b) high chloride dust. Scale bar is 1 μm.

The SEM pictures of pellets (low chloride) sintered at 300-500 ^{o}C for 8 hours are shown in Figure 5.5.

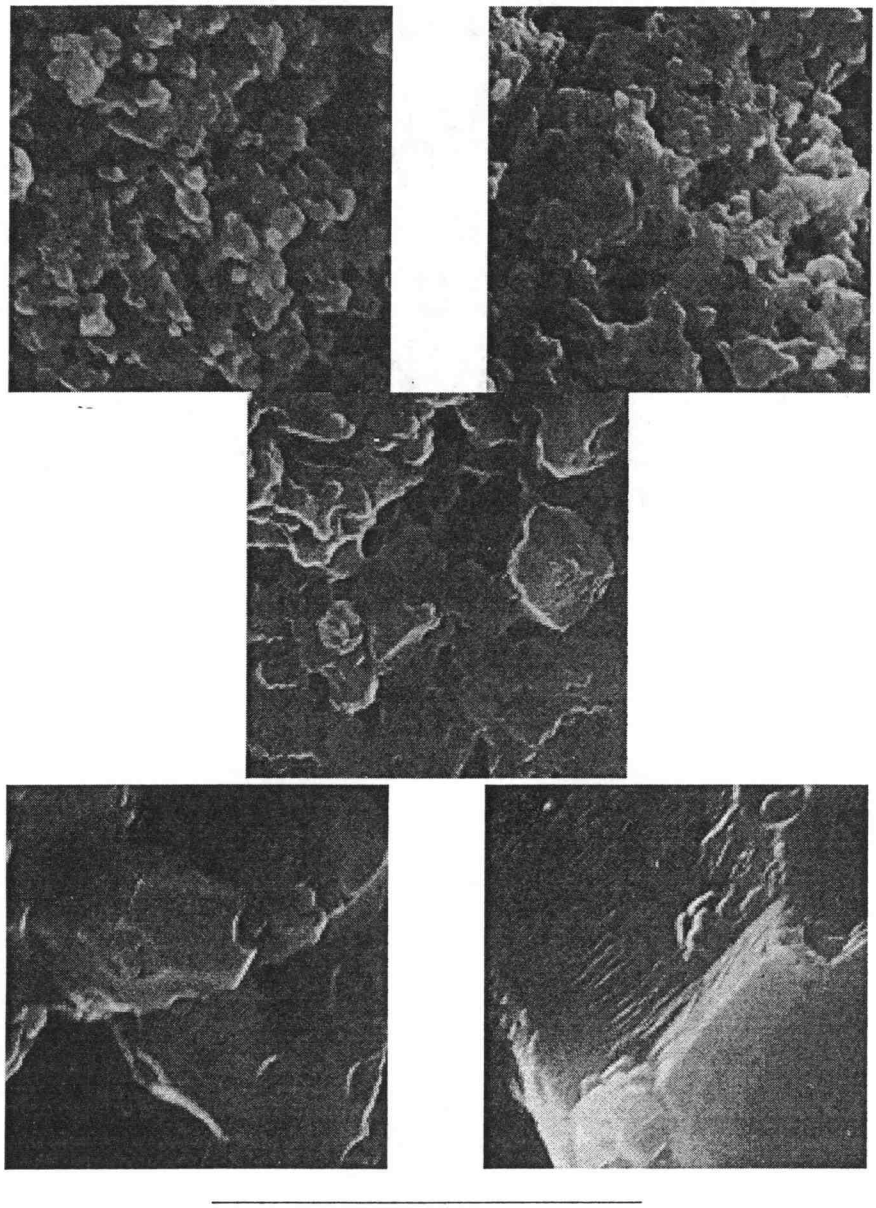

Figure 5.5 : SEM pictures of pellets (low chloride) sintered for 8 hours, (upper left) 300 ^{0}C, (upper right) 350 ^{0}C, (center) 400 ^{0}C, (lower left) 450 ^{0}C, (lower right) 500 ^{0}C. Scale bar is 10 μm

For the pellet sintered at 300 ^{0}C for 8 hours (see Figure 5.5), only particle bridging occurred. The average particle size has not changed from the initial one. The pores are still open and connected. Only initial stage sintering took place. For the pellet sintered at 350 ^{0}C for 8 hours, sintering occurred up to the point that some pores became closed and average grain size increased slightly. This point of sintering can be taken as a reference for the end of initial stage and the beginning of intermediate stage. Since the initial stage sintering model predicts the relative linear shrinkage with time, the linear shrinkage at this point of time (8 hours), which is about 10%, will be used as the upper limit for modeling of this stage in the next chapter. For the pellets sintered at 400-500 ^{0}C for 8 hours, significant grain growth occurred. There are still some pores left in the 400 ^{0}C pellet sample, but most of them are closed. From Figure 5.1, the densification rate is very low at this point of time for the sintering at 400 °C. This indicates that sintering of dust pellets at 400 ^{0}C reached the transition point between the intermediate stage and the final stage after 8 hours of sintering. At 450 and 500 ^{0}C, almost all of the pores were eliminated before 8 hours of sintering. There are still some tiny pores trapped at the grain corners, but the volume fraction of these pores is very small compared to the grain volume. The pellets sintered at these two temperatures reached the final stage long before 8 hours as can be seen in Figure 5.1. The final grain size, determined by a direct measurement on SEM pictures, as a function of temperature is shown in Figure 5.6. The final grain size increases sharply at temperature close to the first melting point.

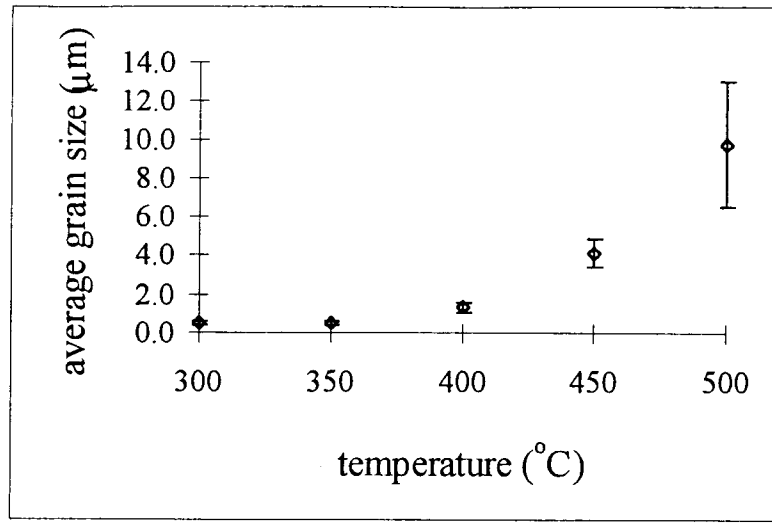

Figure 5.6 : Final grain size at each sintering temperature (Error bars are standard deviations.)

The SEM pictures of pellets (low chloride) sintered for different periods of time at 400, 450, and 500 ^{0}C are shown in Figures 5.7, 5.8, and 5.9 respectively.

At 400 ^{0}C, There was no grain growth for the pellets sintered for 5 and 10 minutes. There was substantial grain growth for the pellets sintered for 30 minutes. Therefore, the intermediate stage sintering started somewhere between 10 minutes and minutes of sintering. At 450 ^{0}C, there was no grain growth for the pellet sintered for 3 minutes. There was substantial grain growth for the pellet sintered for 7 minutes. This shows that the intermediate stage sintering started somewhere between 3 and 7 minutes of sintering. At 30 minutes, most of the pores were already eliminated and the sintering was essentially in the final stage. This is in agreement with Figure 5.1 which shows that at this sintering time, the final density had been reached. At 500 ^{0}C, the pellet sintered

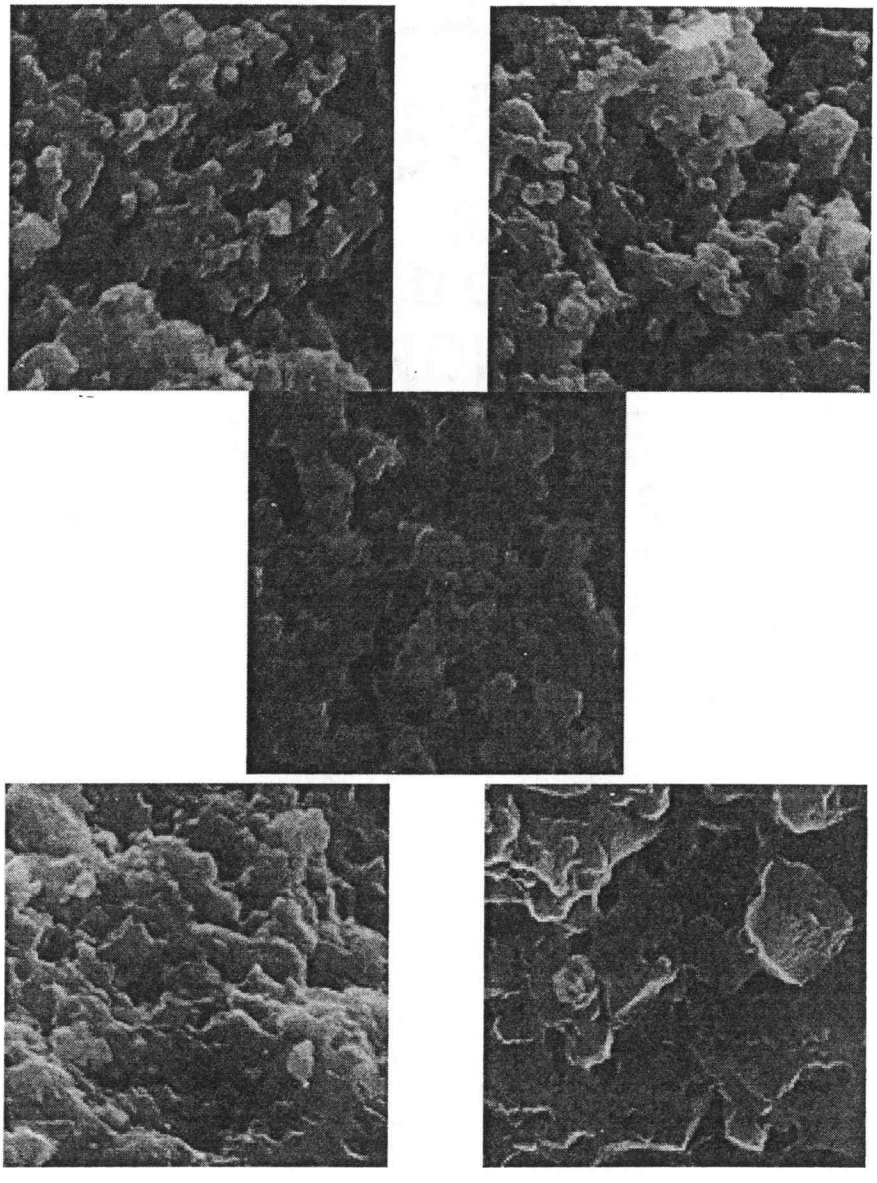

Figure 5.7 : SEM pictures of pellets (low chloride) sintered at 400 ^{0}C, (upper left) 5 min, (upper right) 10 min, (center) 30 min, (lower left) 60 min, (lower right) 480 min. Scale bar is 10 μm

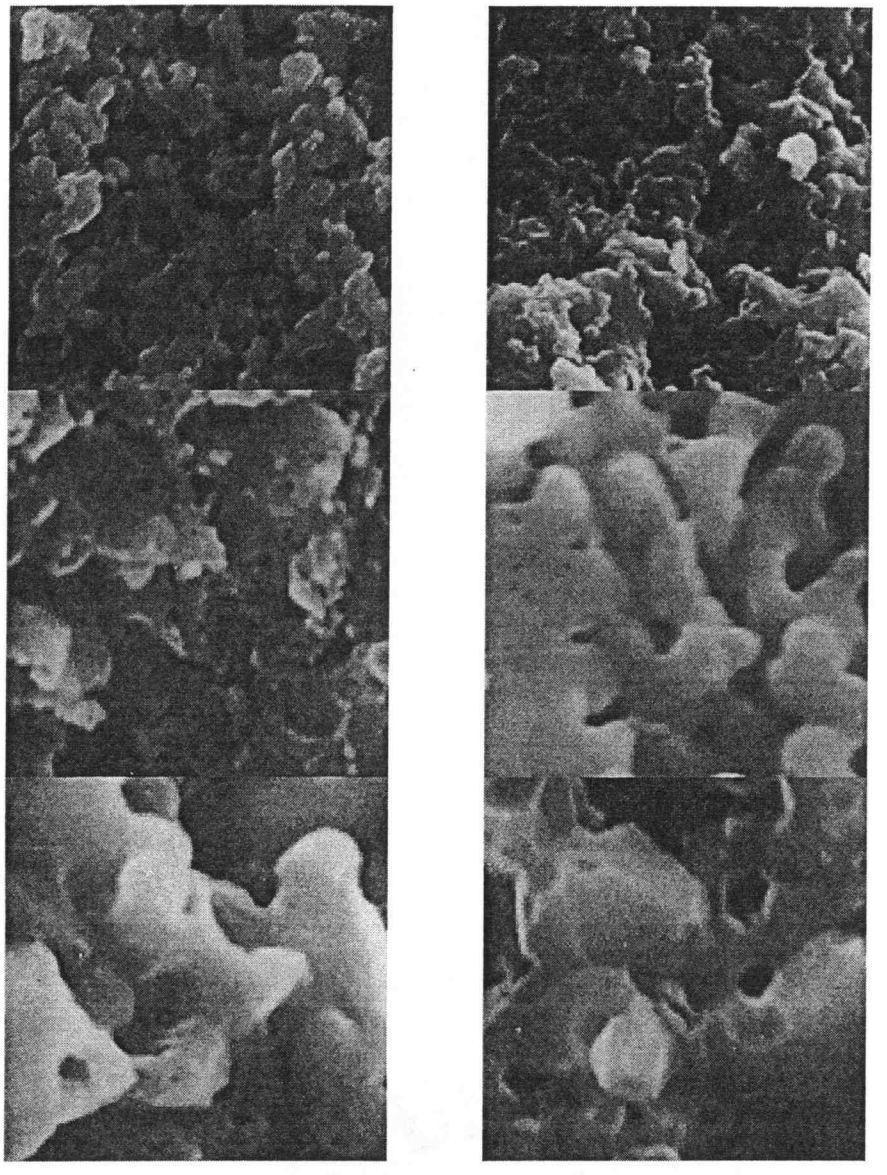

Figure 5.8 : SEM pictures of pellets (low chloride) sintered at 450 ^{0}C, (upper left) 3 min, (upper right) 7 min, (center left) 10 min, (center right) 15 min, (lower left) 30 min, (lower right) 60 min. Scale bar is 10 μm.

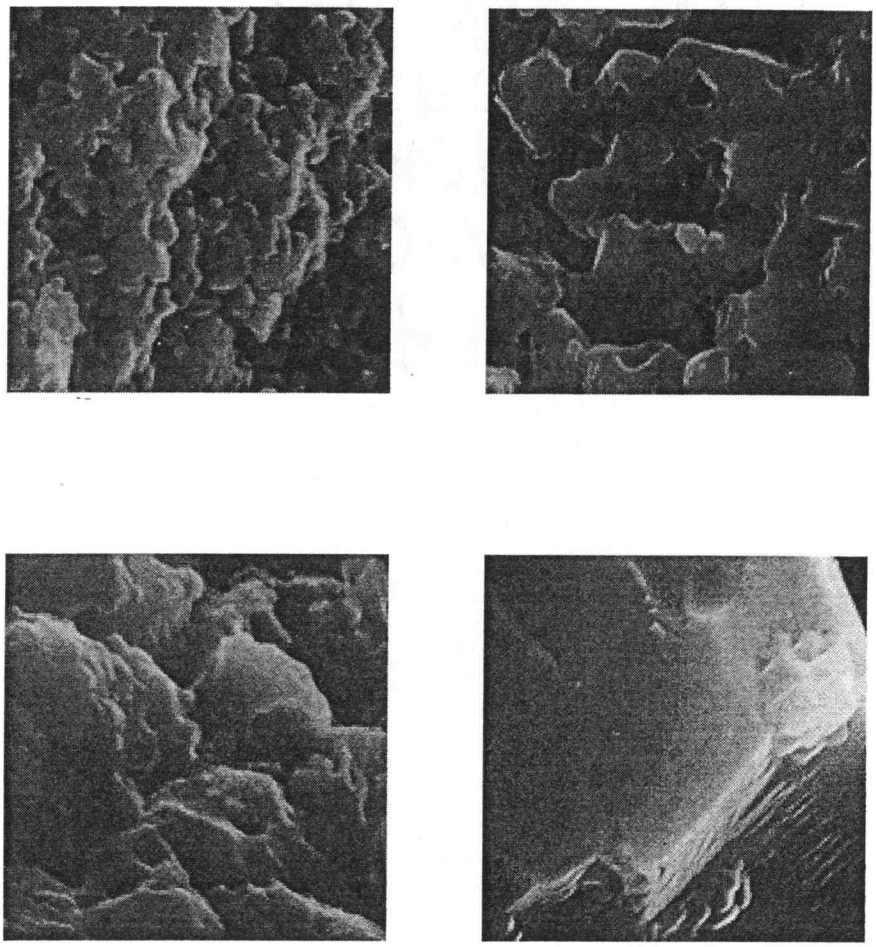

Figure 5.9 : SEM pictures of pellets (low chloride) sintered at 500 ^{0}C, (upper left) 3 min, (upper right) 5 min, (lower left) 10 min, (lower right) 480 min. Scale bar is 10 μm

for 3 minutes experienced substantial grain growth and some amount of closed pores. Hence, the sintering at this temperature reached the intermediate stage before 3 minutes. For the pellet sintered for 10 minutes, most of the pores were already eliminated and the sintering was already in the final stage. This agrees well with Figure 5.1 which shows that at this time, the final density had been reached.

From thermodynamic point of view, we can explain the process using free energy concept. The increase in temperature results in the excess free energy of the system. To shift to a new equilibrium at the lowest energy state, the system must utilize this amount energy. By sintering, the system can reduce its total surface area, resulting in decrease in total surface energy. Even though the system experiences an increase in total grain-boundary energy, the outcome is a decrease in excess free energy. At low sintering temperatures, the excess free energy is so low that the system can reach the equilibrium by mean of initial stage sintering. At high sintering temperature, the excess free energy is so high that the system reduces almost all of the surface area, resulting in a significant increase in grain-boundary area. At temperatures very close to the first melting point, the higher excess free energy results in the migration of the grain boundary in order to reduce the total grain-boundary energy and increase the total bonding energy in the bulk of solid. The outcome is the use of excess free energy to put more atoms into the crystal structure via the grain growth process. By direct measurement on the SEM pictures, the grain size and time data for each sintering temperature was recorded. This data is included in Appendix D. The isotherms of average grain size change with time are shown in Figure 5.10.

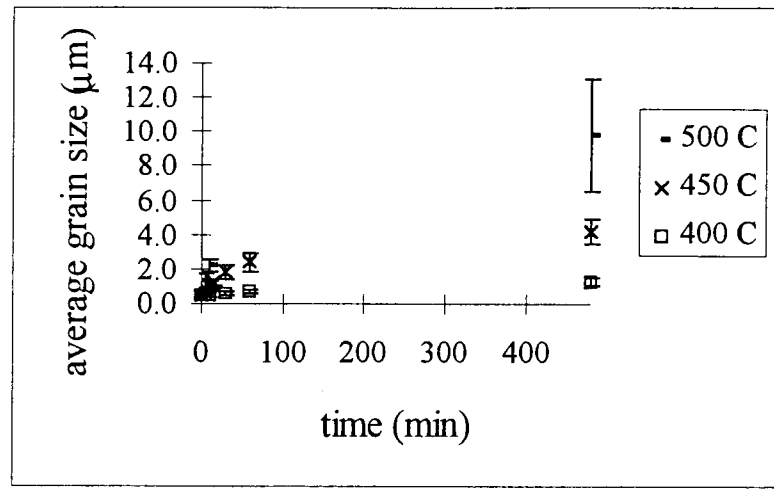

a

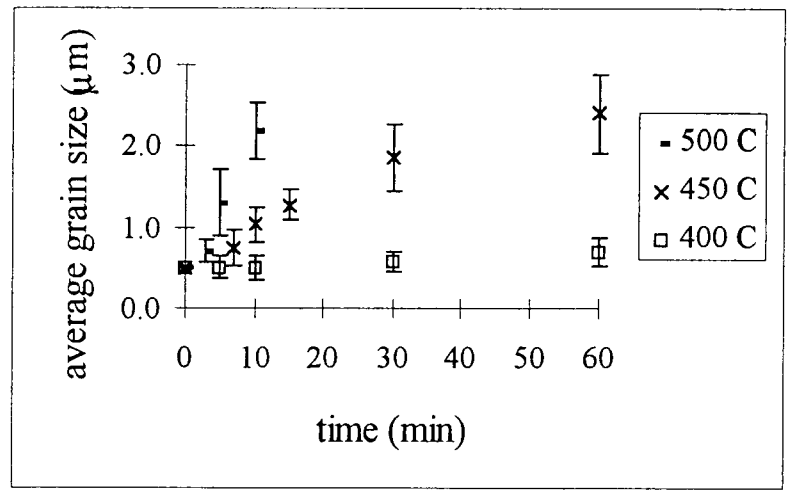

b

Figure 5.10 : Isotherms of average grain size change with time, (a) scale 0-480 min, (b) scale 0-60 min (Error bars are standard deviation)

5.5 Effect of Initial Density

A series of experiment were conducted in order to study the effect of the green density of pellets on the sintering kinetics. Pellets made from the low chloride dust with four different values of initial density were sintered at 450 ^{0}C for different period of time. The results are shown in Figure 5.11 below.

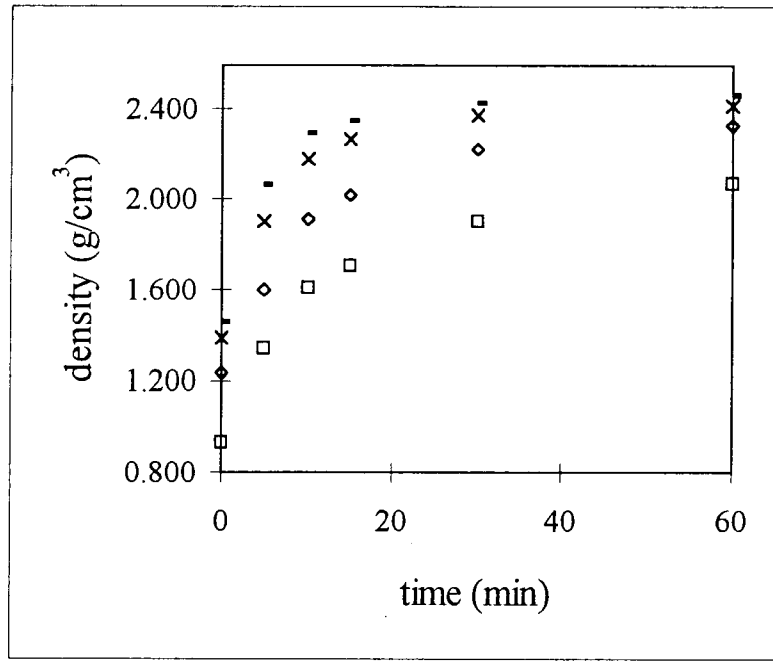

Figure 5.11 : Sintering of pellets (low chloride) with different initial density at 450 ^{0}C

It can be seen that the densification rate is independent of the initial density of the pellet. All the pellets reached the final density within about 60 minutes. The differences in final density is roughly the same as the differences in initial density. However, the less-packed pellets tends to shrink a little bit more after 60 minutes.

5.6 Final Density

The theoretical density of a solid is the density of each individual dense perfect crystalline particle. The alkali salt crystalline particle is dense by nature. Therefore, the theoretical density of fume dust can be estimated from the intrinsic density of the dust particles using a porosimeter. In this study, the density of the sintered pellet having the highest final density is used as a theoretical density for each specific dust regardless of the essentially negligible volume fraction of trapped pores. The theoretical density of both kinds of dust is shown in Table 5.3.

Table 5.3 : Theoretical densities of the dusts

Dust sample	Theoretical density (g/cm^3)
low chloride	2.507
high chloride	2.450

5.7 Effect of Chloride Contents

Since the theoretical density of low chloride dust is different from high chloride dust, the fractional density was used in order to compared the densification rate of the two dusts. Fractional density is defined as the ratio of the compact density and the theoretical density (See Appendix E for the data). It tells how high the compact density compares to the theoretical density. The comparison of densification rate of the pellets made from the two dusts at various temperatures is shown in Figure 5.12.

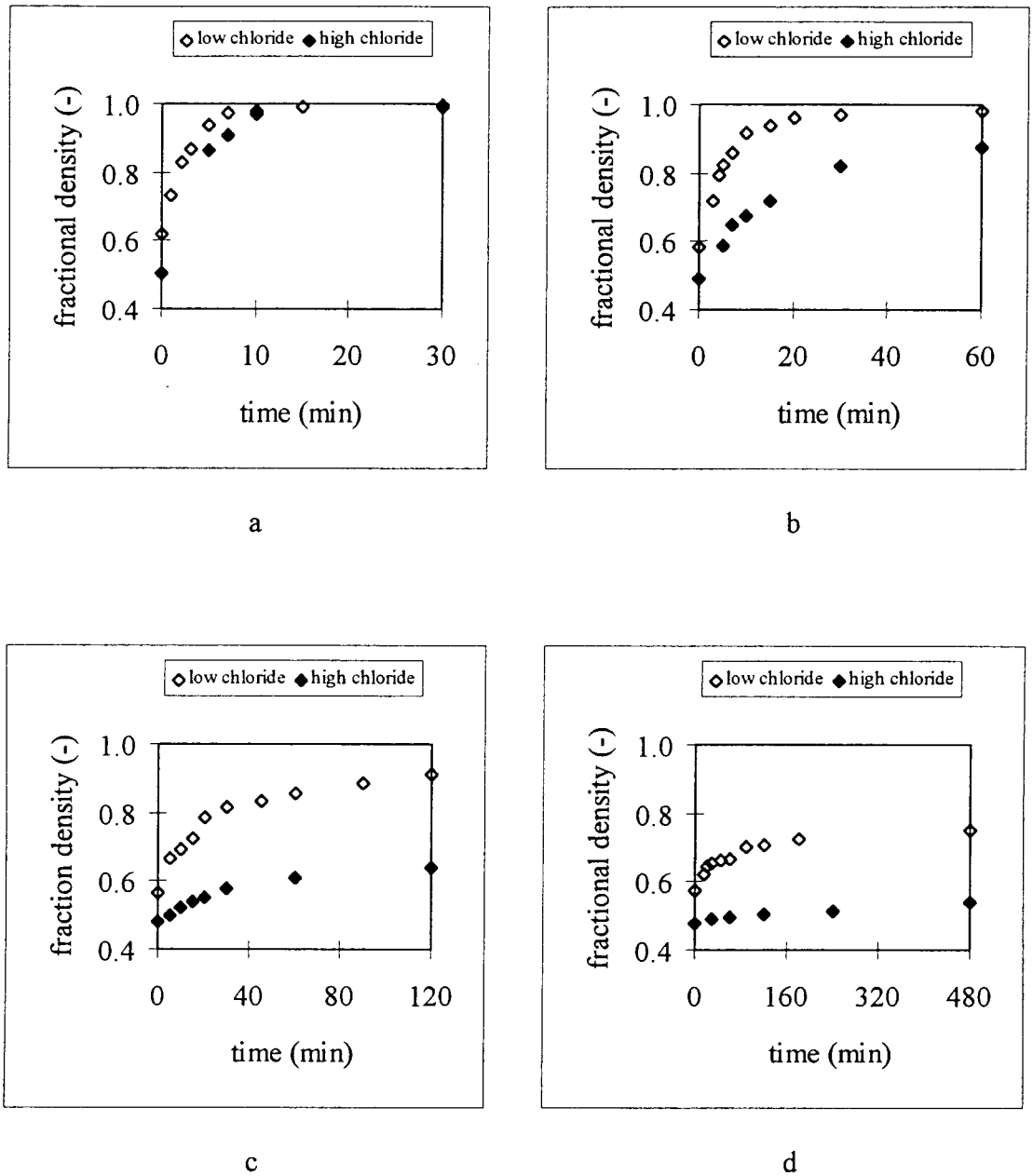

Figure 5.12 : Fractional density changes with time of two dusts, (a) 500 ^{0}C, (b) 450 ^{0}C, (c) 400 ^{0}C, (d) 350 ^{0}C

It can be seen that the densification rate of high chloride dust is much lower than that of low chloride dust at low sintering temperatures. At higher sintering temperatures, the densification rate is not much different for both dusts. At 500 ^{0}C, both dusts have about the same densification rate. The average final fractional density of sintered pellets for both dusts at various sintering temperatures is shown in Table 5.4. For comparison, the average initial fractional density of a pellet made from low chloride dust is about 0.571 and that of a pellet made from high chloride dust is about 0.482.

Table 5.4 : Comparision of the average final fractional density of pellets made from different dusts sintered at various temperature

Dust sample	**Average final fractional density (-)**			
	500 ^{0}C	450 ^{0}C	400 ^{0}C	350 ^{0}C
low chloride	0.991	0.997	0.965	0.752
high chloride	0.989	0.971	0.748	0.541

At low temperatures, the sinterability of the low chloride dust is higher than high chloride dust. For example, the fractional density of low chloride pellets increased by 32% at 350 ^{0}C and 69 % at 400 ^{0}C while the fractional density of high chloride pellets increased by 12 % and 55 % at these two temperatures. At higher temperatures, the final fractional density of both dusts is close to 1. This indicates that the different in chloride content does not have a significant effect on the degree of sintering at high temperatures.

Sodium chloride has a lower surface energy than sodium sulfate. Therefore, the presence of chloride species in the fume dust can cause a substantial decrease in surface energy of the sulphate species which is the major phase. The subsequent effect is a lower energy requirement for the surface atoms to diffuse into the bulk and form bonds with the atoms in the bulk. This results in the higher potential for the system to reduce its total surface area when there is an increase in excess free energy. In other word, at the same sintering temperature, fume dust has higher sinterability than pure sulphate salts having the same particle size.

Thermodynamically, chloride species tends to form a separate phase at the surface of the particle to form the most stable energy configuration. This is in agreement with the fume formation mechanisms mentioned in Chapter 3. It is postulated here that a little amount of chloride can result in a great decrease in surface energy. However, the presence of a higher amount of chloride does not result in a further decrease in surface energy, but acts as a non-densifying phase blocking the diffusion pathway. This excess amount of chloride can also retard the grain growth rate during the intermediate stage sintering by slowing atom diffusion across the grain boundary.

Dust with low chloride sinters better than dust with high chloride at low sintering temperatures because there is less non-densifying phase. Therefore, the bridging of dust particles in the initial stage sintering is much easier. However, at higher temperatures, dust with high chloride can sinter close to the final density because of the slow grain growth rate in the intermediate stage sintering. With the slower grain growth rate,

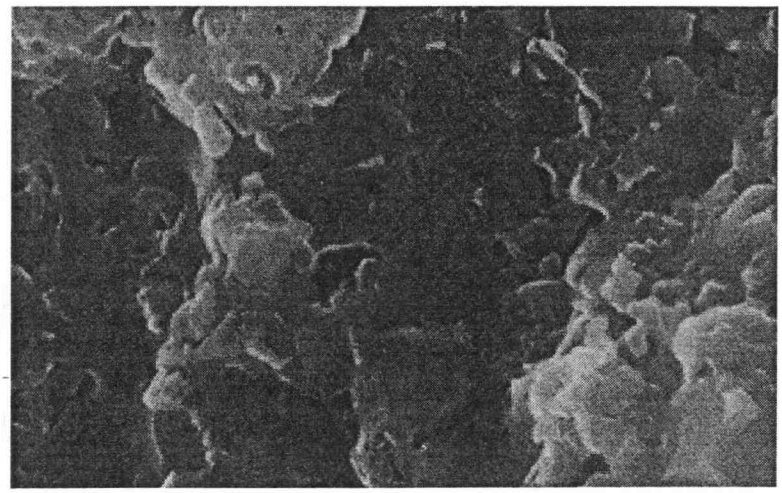

a

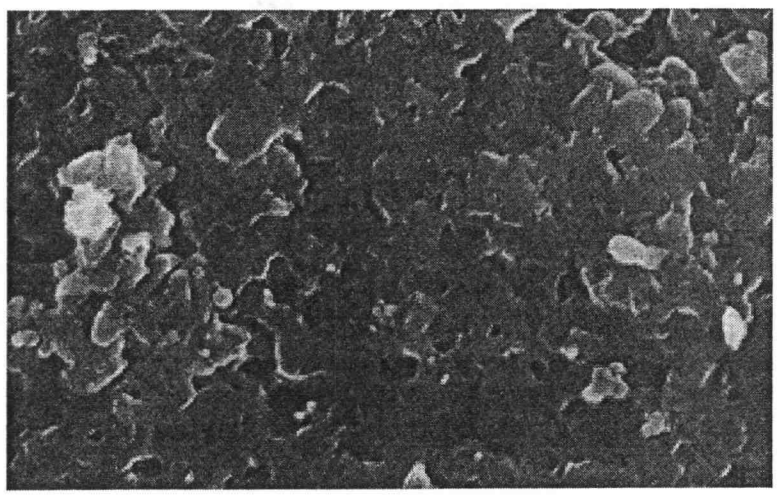

b

Figure 5.13 : Morphology of pellets sintered at 450 ^{0}C for 60 minutes,
(a) low chloride dust, (b) high chloride dust

the densification process can occur much more extensively because the smaller grain size can result in the larger total surface area which is the driving force for the sintering process. Even though the densification process in the intermediate stage sintering of the high chloride dust is retarded by the lower diffusive pathway, this effect is counterbalanced by the grain size effect. The grain sizes of both dusts sintered at 450 ^{0}C for 60 minutes are shown in Figure 5.13.

CHAPTER 6
MODELING OF SINTERING OF LOW CHLORIDE DUST

This chapter contains the modeling work of sintering and grain growth of the low chloride dust. For the high chloride dust, there is not enough data on the kinetics of grain growth which is an essential part for the modeling of the sintering process. Therefore, it is not possible to develop a model for the sintering of the high chloride dust.

6.1 Initial Stage Sintering

Eq.(2.6) is rewritten below,

$$\frac{\Delta L}{L_0} = \left[\frac{K\gamma\Omega D}{kTG_0^p}\right]^n t^n \qquad 2.6$$

The mechanism based constant n ranges from 0.4-0.5 for volume diffusion control and 0.31-0.33 for grain-boundary diffusion control as shown in Table 2.3. The values of p are 3 for volume diffusion control and 4 for grain-boundary diffusion control. The K, γ, Ω, D, and k values are grouped together to be an empirical parameter K_1 since some physical parameters are not known. Only the diffusion coefficient D is dependent on the temperature. It is further assumed here that the size distribution effect and packing non-uniformity are taken care of by the parameter K_1.

From Chapter 5, the initial stage sintering exists and is observable at 300, 350, and 400 ^{0}C. At 300 ^{0}C, the sintering is in this stage throughout 8 hours time frame. At

350 ^{0}C, all data points but the one for 8-hour sintering are considered to be in this stage. For 400 ^{0}C, the sintering for a period no longer than 10 minutes is classified as the initial stage.

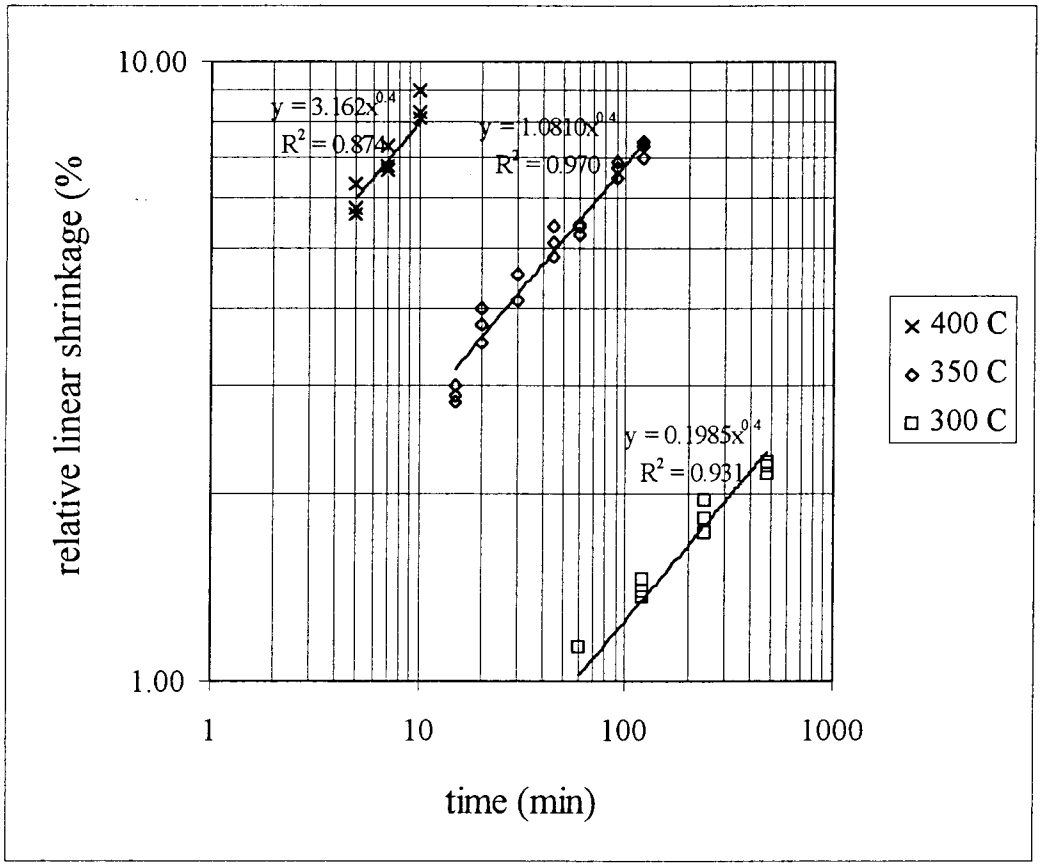

Figure 6.1 : Relative linear shrinkage as a function of time for the initial stage sintering (Note : At 400 ^{0}C, the shrinkage at time zero was subtracted from all the data points.)

From the plot shown in Figure 6.1, the data fit pretty well with the linear shrinkage model to the power of 0.4 which corresponds to the model proposed by Kingery and Berg[7]. The controlling mechanism is therefore volume diffusion. The K_1 for each isotherm was calculated from the slope as shown below,

$$\left[\frac{K\chi\Omega D}{kTG_0^p}\right]^n = \frac{slope}{100}$$

$$\left[\frac{K_1}{TG_0^p}\right]^n = \frac{slope}{100}$$

$$K_1 = \left[\frac{slope}{100}\right]^{1/n} TG_0^p$$

$$K_1 = \left[\frac{slope}{100}\right]^{1/0.4} TG_0^3$$

The value G_0 is constant at 0.5 μm and T is the absolute temperature. At 300 ^{0}C,

$$K_1 = \left[\frac{0.1985}{100}\right]^{2.5} (573)\left(0.5\times10^{-4}\right)^3$$

$$= 1.26\times10^{-17} \quad [\text{K-cm}^3/\text{min}]$$

The value of K_1 for each temperature is shown in Table 6.1. The Arhenius-type plot of K_1 is shown in Figure 6.2. From the slope of the plot, we obtain the apparent activation energy E_1 which is equal to 54.5 ± 27.7 kcal/mol or 227.9 ± 115.9 kJ/mol with 90% confidence interval using t-Distribution. The value K_1 can be written as a function of temperature as shown in eq.(6.1)

Table 6.1 : Value K_1 at 300-400 ^{0}C

Temperature (^{0}C)	K_1 (K-cm^3/min)
300	1.26×10^{-17}
350	9.46×10^{-16}
400	1.50×10^{-14}

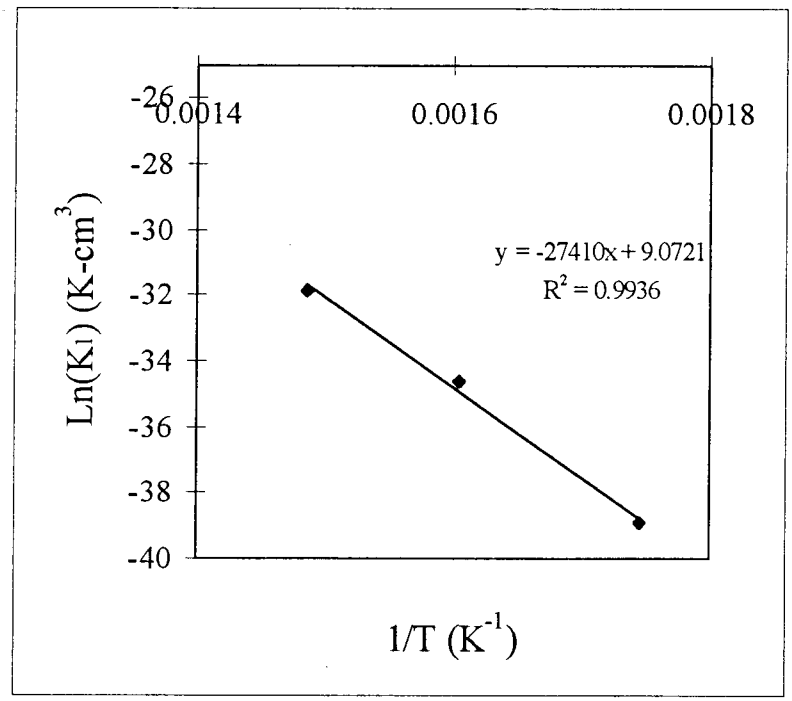

Figure 6.2 : Arhenius-type plot of K_1

$$K_1 = K_1' e^{\frac{-E_1}{RT}} \qquad 6.1$$

where K_1' = 8.71×10^3 [K-cm^3/min]

E_1 = 227.9 [kJ/mol]

Then, the relative linear shrinkage model can be written as

$$\frac{\Delta L}{L_0} = \left[\frac{K_1}{TG_0^3}\right]^{0.4} t^{0.4} \qquad 6.2$$

where $G_0 = 0.5 \times 10^{-4}$ [cm]

From Chapter 5, this initial stage sintering model limits to the first 10% relative linear shrinkage which is the value of the 8-hour sintering at 350 ^{0}C.

6.2 Grain Growth

The grain growth kinetic equation from chapter 2 is rewritten here,

$$G^N - G_0^N = m(t - t_0) \qquad 2.15$$

The typical value of N is 3. From the grain size-time data at 400-500 ^{0}C in Appendix D, we can find the rate constant m for the grain growth rate at each sintering temperature as follow.

6.2.1 Grain Growth Rate At 400 ^{0}C

From the available data, the first substantial grain growth was observed at 30-minute sintering. Therefore, t_0 is set to be 30 minutes and G_0 is essentially 0.57 μm instead of 0.50 μm. The use of different values of G_0 does not have any effect on the grain growth rate. G^3-G_0^3 and t-t_0 were calculated and shown in Table 6.2.

Table 6.2 : Values t, G, $t-t_0$, and $G^3-G_0^3$ for grain growth at 400 ^{0}C

t	G	$t-t_0$	$G^3-G_0^3$
30	0.57	0	0.000
60	0.70	30	0.158
480	1.30	450	2.012

The plot between $G^3-G_0^3$ and $t-t_0$ is shown in Figure 6.3. From the plot, rate constant m appears to be 0.0045 μm^3/min. The data fit well with the model

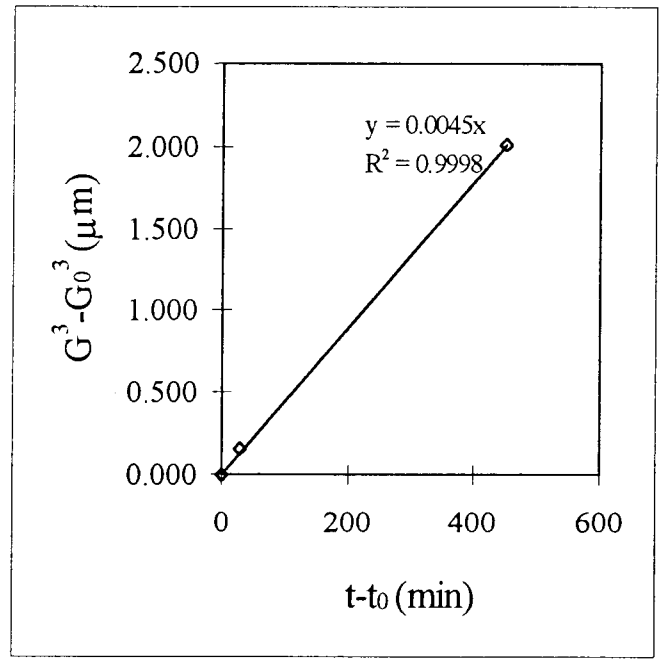

Figure 6.3 : Grain growth rate at 400 ^{0}C

6.2.2 Grain Growth Rate At 450 ^{0}C

From the available data, the first substantial grain growth was observed at 7-minute sintering. Therefore, t_0 is set to be 7 minutes and G_0 is essentially 0.75 μm. The G^3-G_0^3 and t-t_0 were calculated and shown in Table 6.3.

Table 6.3 : Values t, G, t-t_0, and G^3-G_0^3 for grain growth at 450 ^{0}C

t	G	t-t_0	G^3-G_0^3
7	0.75	0	0.000
10	1.03	3	0.671
15	1.27	8	1.627
30	1.85	23	5.910
60	2.40	53	13.402
480	4.15	473	71.052

The plot between G^3-G_0^3 and t-t_0 is shown in figure 6.4. From the plot, rate constant m appears to be 0.1518 μm^3/min. The data fit well with the model.

6.2.3 Grain Growth Rate At 500 ^{0}C

From the available data, the first substantial grain growth was observed at 3-minute sintering. Therefore, t_0 is set to be 3 minutes and G_0 is essentially 0.70 μm. The G^3-G_0^3 and t-t_0 were calculated and shown in Table 6.4. The plot between

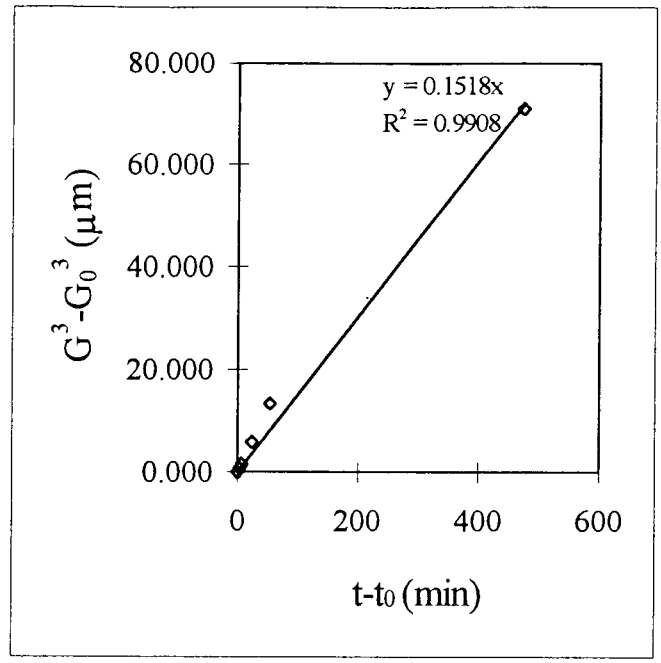

Figure 6.4 : Grain growth rate at 450 ^{0}C

G^3-G_0^3 and t-t_0 is shown in Figure 6.5. From the plot, rate constant m appears to be 1.9723 μm^3/min. The data fit well with the model.

Table 6.4 : Values t, G, t-t_0, and G^3-G_0^3 for grain growth at 500 ^{0}C

t	G	t-t_0	G^3-G_0^3
3	0.70	0	0.000
5	1.30	2	1.854
10	2.18	7	10.017
480	9.80	477	940.85

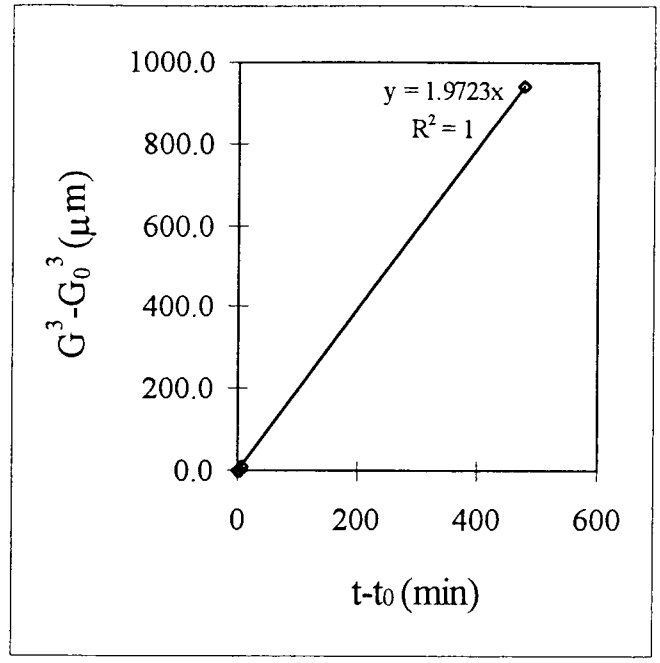

Figure 6.5 : Grain growth rate at 500 ^{0}C

The rate constant m at each sintering temperature is shown in Table 6.5 below,

Table 6.5 : Grain growth rate constant m at 400-500 ^{0}C

Temperature (^{0}C)	**m (μm^3/min)**
400	0.0045
450	0.1518
500	1.9723

The Arhenius-type plot for m is shown in Figure 6.6. The calculated apparent activation energy E_G is equal to 63.0 ± 20.1 kcal/mol or 263.6 ± 84.1 kJ/mol with 90% confidence interval using t-Distribution. The calculated m_0 is equal to 1.42×10^{18} μm^3/min. The grain growth kinetic equation can be rewritten as shown in eq.(6.3).

$$G^3 - G_0^3 = m_0 e^{-\left(\frac{E_G}{RT}\right)}(t - t_0) \qquad 6.3$$

where t_0 = time at which relative linear shrinkage reaches 10%

G_0 = 0.5 μm

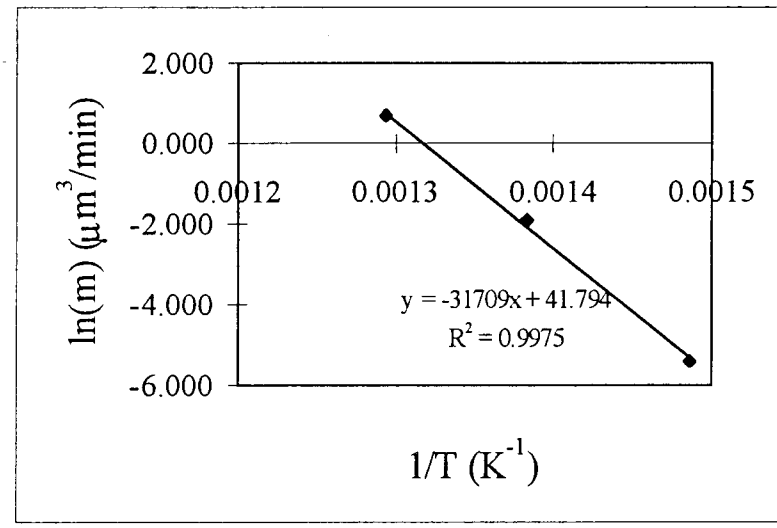

Figure 6.6 : Arhenius plot of grain growth rate constant m

It is important to comment here that each data point in Figures 6.3, 6.4, and 6.5 has a wide range of uncertainty due to the scattering of measured grain sizes. A rate constant m is subjected to the grain growth rate that fits best with all the average values. Therefore, a grain growth rate model at each temperature is controlled mainly by large values of G^3-G_0^3 and t-t_0, resulting in slight deviation of the model from the measured values when G^3-G_0^3 and t-t_0 are small. However, these models are acceptable since the differences of the calculated values and the measured values are within the range of uncertainty.

6.3 Intermediate Stage Sintering

The sintering model with volume diffusion as a control mechanism from eq.(2.14) is rewritten below,

$$\frac{dP}{dt} = \frac{-720 D_V \gamma \Omega}{G^3 kT} \qquad 2.14$$

Since the model includes some unknown parameters, the coefficient 720 and parameters D_V, γ, Ω, and k are grouped together to be an empirical constant K_2 which is temperature dependent through the parameter D_V. Eq.(2.14) can be rewritten as

$$\frac{dP}{dt} = \frac{-K_2}{G^3 T} \qquad 6.4$$

Because grain size also changes with time as shown in eq.(6.3), eq.(6.4) can be rewritten as eq.(6.5). The term in the bracket has been extended from the grain growth.

$$\frac{dP}{dt} = \frac{-K_2}{T}\left[\frac{1}{m(t-t_0)+G_0^3}\right] \qquad 6.5$$

By integration from t_0 to t and from P_0 to P, the model predicting porosity as a function of time is obtained as shown in eq.(6.6).

$$P = \frac{-K_2}{mT} Ln\left[\frac{m(t-t_0)+G_0^3}{G_0^3}\right] + P_0 \qquad 6.6$$

where t_0 = time when intermediate stage sintering starts or when initial stage sintering ends

G_0 = grain size at time t_0

P_0 = porosity at time t_0

Since the fume particle is non-porous, the porosity of a sintered pellet can be calculated by subtract the fractional density from 1 as shown in eq.(6.7) below,

$$P = 1 - \frac{\rho}{\rho_{th}} \qquad 6.7$$

where ρ = bulk density of a sintered pellet

ρ_{th} = theoretical density of fume dust

All the porosity versus time data at each sintering temperature can be found in appendix E. From Chapter 5, at 400 ^{0}C, the intermediate stage started before 30 minutes and ended before 480 minutes. Therefore, data at 30, 45, 60, and 120 minutes were used for model fitting. At 450 ^{0}C, the intermediate stage started before 7 minutes and ended before 30 minutes. Therefore, data at 7, 10, 15, and 20 minutes were used for model fitting. At 500 ^{0}C, the intermediate stage started before 3 minutes and ended before 10 minutes. Therefore, data at 3, 5, and 7 were used for model fitting. From the available data, t_0 values are 30, 7, and 3 minutes for sintering at 400, 450, and 500 ^{0}C respectively. The G_0 values are essentially 0.57, 0.75, and 0.70 μm for 400, 450, and

500 ^{0}C respectively. Even though all t_0 values are not the real starting time of intermediate stage sintering, they do not interfere with the densification rate predicted by eq.(6.5).

Let Λ stands for the term $\mathrm{Ln}\left[\frac{m(t-t_0)+G_0^3}{G_0^3}\right]$. The value Λ for each porosity-time data at each temperature was calculated and shown in Tables 6.6, 6.7, and 6.8 for 400, 450, and 500 ^{0}C respectively. The m values were obtained from the grain growth rate constants in Table 6.5. The plots between Λ and P for the three temperatures are shown in Figures 6.7, 6.8, and 6.9.

Table 6.6 : The values Λ at each porosity-time data for each individual pellet during intermediate stage sintering at 400 ^{0}C

t (min)	Λ (-)	P (-)
30	0.000	0.171
30	0.000	0.167
30	0.000	0.150
30	0.000	0.156
30	0.000	0.168
30	0.000	0.180
30	0.000	0.185
45	0.311	0.130
45	0.311	0.147
45	0.311	0.154
60	0.548	0.112
60	0.548	0.115
60	0.548	0.108
120	1.159	0.079
120	1.159	0.084
120	1.159	0.098

Table 6.7 : The values Λ at each porosity-time data for each individual pellet during intermediate stage sintering at 450 ^{0}C

t (min)	Λ (-)	P (-)
7	0.000	0.119
7	0.000	0.148
7	0.000	0.148
10	0.732	0.079
10	0.732	0.082
10	0.732	0.088
15	1.355	0.056
15	1.355	0.064
15	1.355	0.064
20	1.737	0.033
20	1.737	0.038
20	1.737	0.050

Table 6.8 : The values Λ at each porosity-time data for each individual pellet during intermediate stage sintering at 500 ^{0}C

t (min)	Λ (-)	P (-)
3	0.000	0.123
3	0.000	0.144
3	0.000	0.117
3	0.000	0.140
3	0.000	0.127
5	2.526	0.066
5	2.526	0.056
5	2.526	0.056
7	3.178	0.021
7	3.178	0.026
7	3.178	0.026
7	3.178	0.031
7	3.178	0.027
7	3.178	0.022

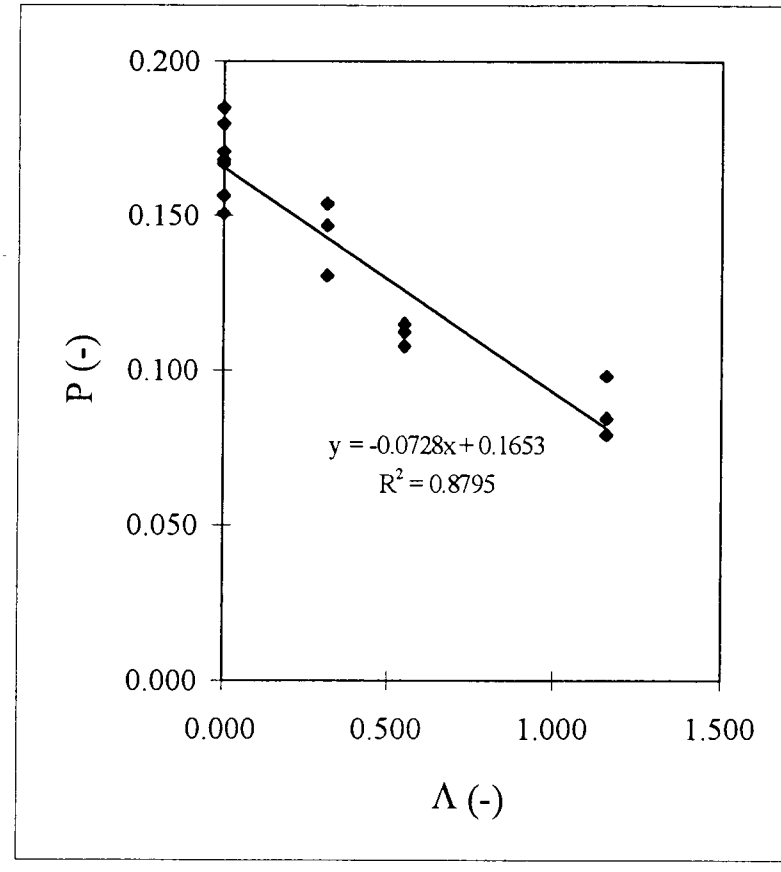

Figure 6.7 : Porosity change with time during the intermediate stage sintering at 400 ^{0}C.

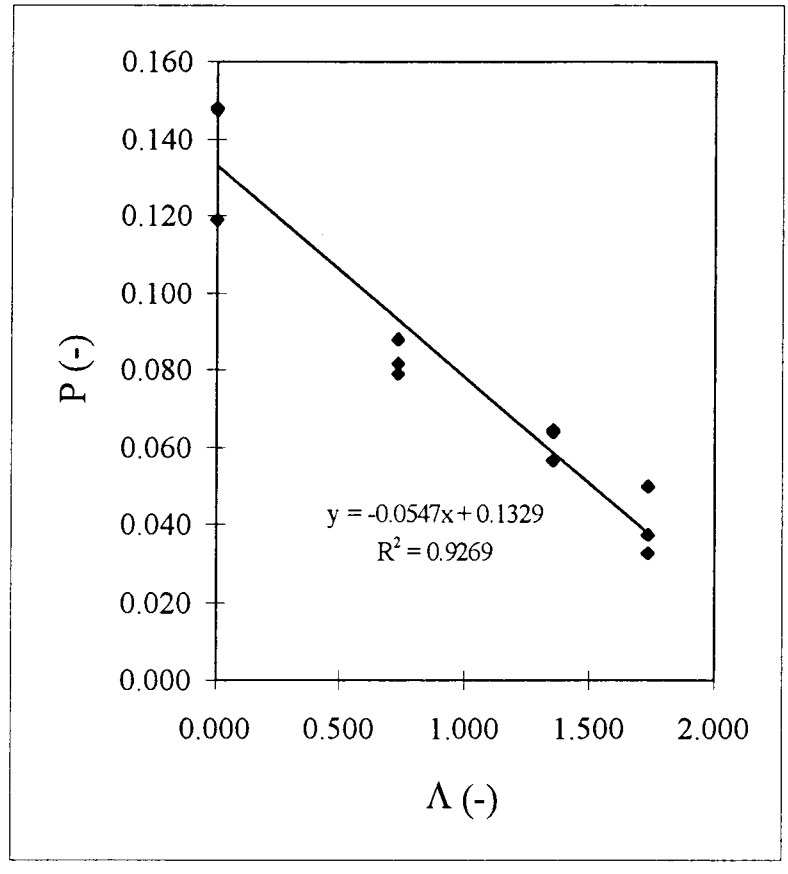

Figure 6.8 : Porosity change with time during the intermediate stage sintering at 450 ^{0}C.

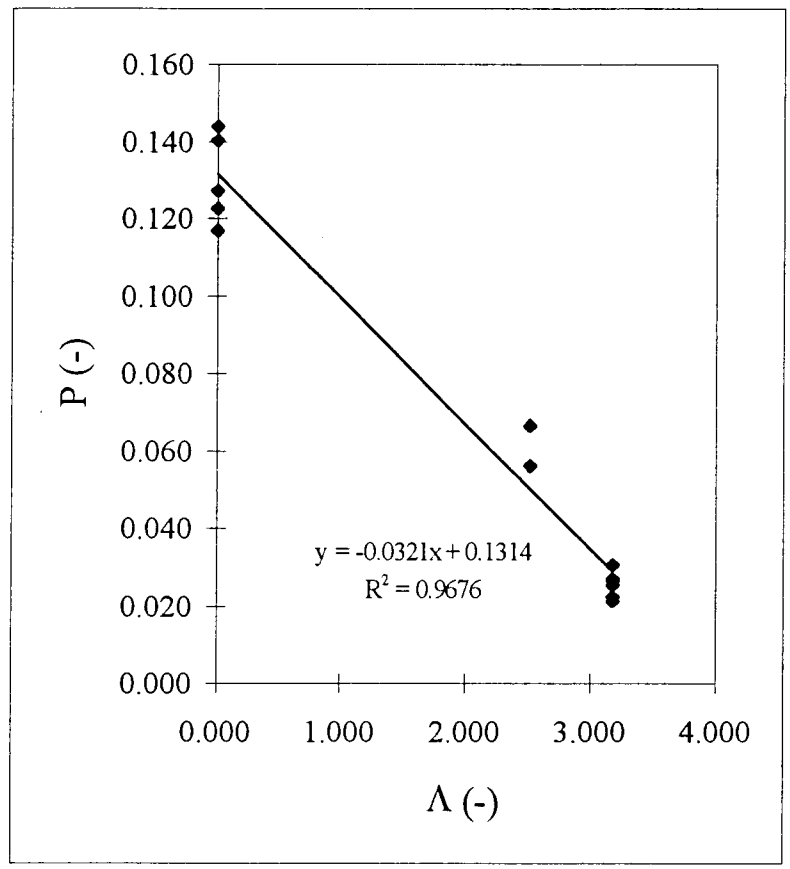

Figure 6.9 : Porosity change with time during the intermediate stage sintering at 500 ^{0}C.

From eq.(6.6), K_2 for each temperature can be obtained by multiply the slope with appropriate value of m and T. The value K_2 for each temperature was calculated and shown in Table 6.9 below,

Table 6.9 : Value K_2 at 400-500 ^{0}C

Temperature (^{0}C)	**K_2 (K-μm^3/min)**
400	0.220
450	6.003
500	48.939

The Arhenius-type plot of K_2 is shown in Figure 6.10 below,

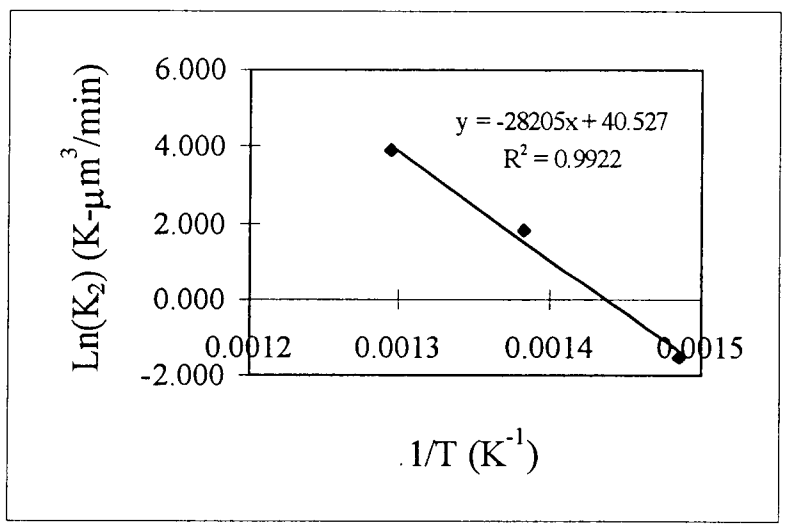

Figure 6.10 : Arhenius-type plot of K_2

From the slope of Arhenius-type plot, we obtain the apparent activation energy E_2 which is equal to 56.0 ± 31.3 kcal/mol or 234.5 ± 131.0 kJ/mol with 90% confidence interval using t-Distribution. The value K_2 can be written as a function of temperature as shown below,

$$K_2 = K_2' e^{\frac{-E_2}{RT}} \qquad 6.8$$

where $K_2' = 3.99 \times 10^{17}$ [K-μm^3/min]

$E_2 = 234.5$ [kJ/mol]

It can be seen that the apparent activation energy of K_2 is very close to that of K_1 for the initial stage sintering. This supports the conclusion that the mass transfer mechanism, volume diffusion, is the same for these two stages of sintering.

6.4 Model Testing

The initial stage, intermediate stage, and grain growth models were tested against the experimental results by mean of porosity and grain size changes with time. The model for initial stage sintering is eq.(6.1) and eq.(6.2). The grain growth model is eq.(6.3). The model for intermediate stage sintering is eq.(6.6) and eq.(6.8). The transition point from the initial stage to intermediate stage is set at 10% relative linear shrinkage. Grains start growing as soon as the intermediate stage begins. For the initial stage sintering, the porosity can be calculated from the linear shrinkage using eq.(6.9)

$$P = 1 - \left(1 - P_{unsintered}\right)\left(1 - \frac{\Delta L}{L_0}\right)^{-3} \qquad 6.9$$

where $P_{unsintered}$ = porosity of an unsintered pellet

obtained by simple dimensional analyses of a cylindrical object. The porosity of an unsintered pellet ($P_{unsintered}$) is about 0.43. The porosity of a sintered pellet at the end of initial stage or at the start of intermediate stage (P_0) is about 0.218. The average grain size before intermediate stage sintering or grain growth (G_0) is about 0.5 μm. The starting time for intermediate stage sintering or grain growth (t_0) can be calculated using eq.(6.2) as follow,

$$0.1 = \left[\frac{K_1}{TG_0^3}\right]^{0.4} t_0^{0.4}$$

$$t_0 = 0.1^{1/0.4}\left[\frac{TG_0^3}{K_1}\right]$$

The final stage is reach when porosity reach 0. The comparison of sintering models with the experimental results is shown in Figure 6.11. The comparison of grain growth model with the experimental results is shown in Figures 6.12 and 6.13.

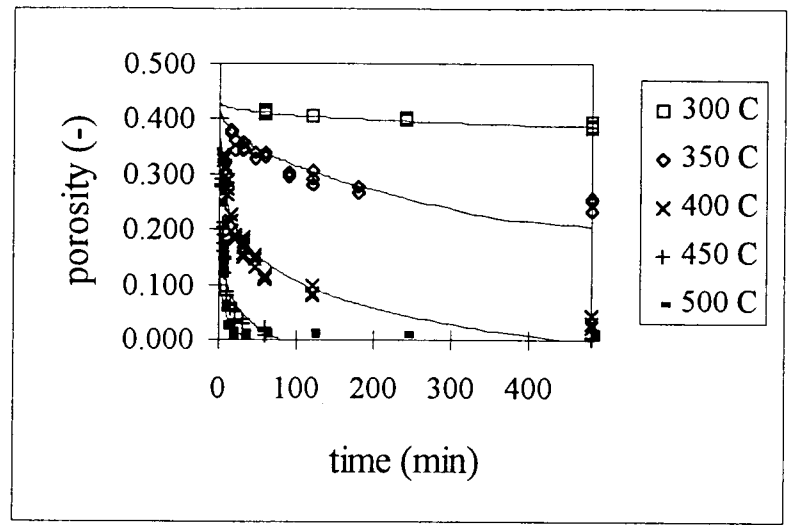

a

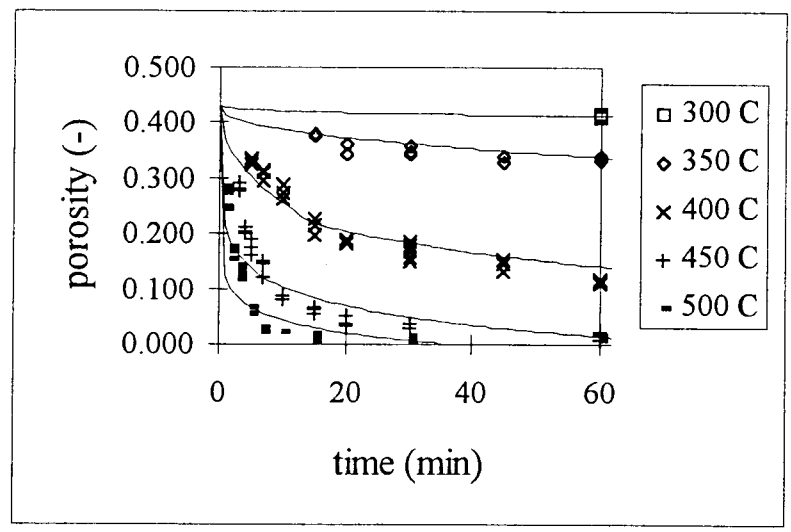

b

Figure 6.11 : Porosity change with time, (a) scale 0-480 min, (b) scale 0-60 min, the solid line is calculated from the model

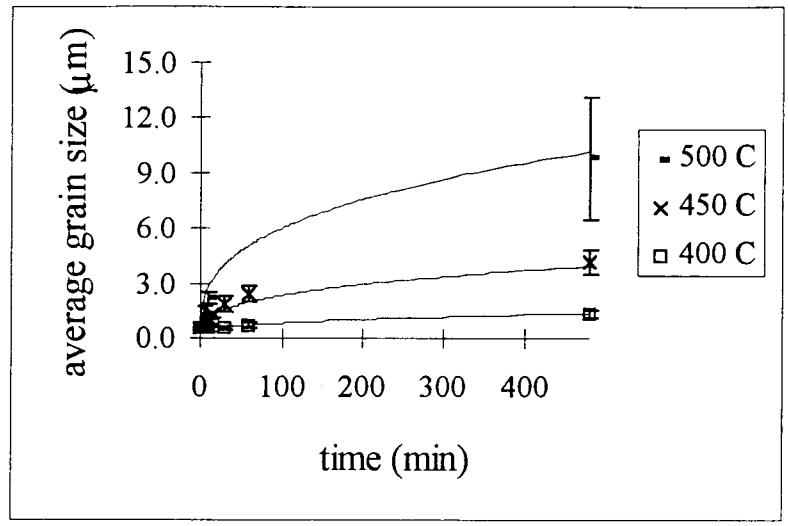

a

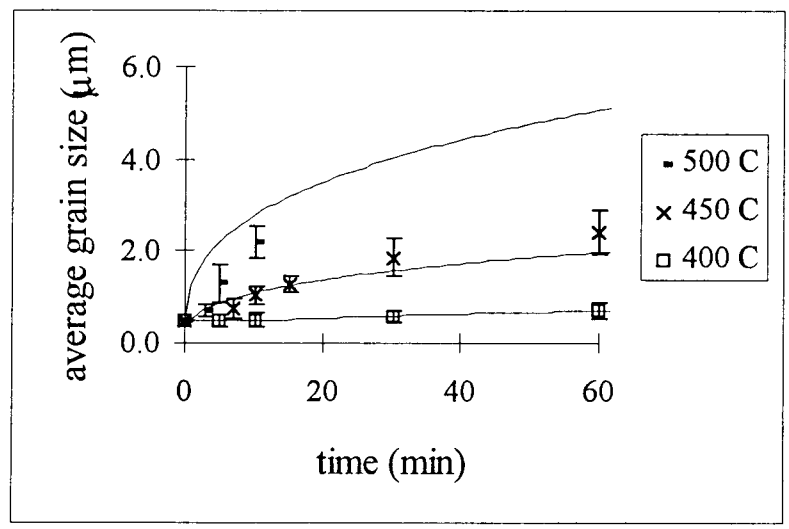

b

Figure 6.12 : Grain size change with time, (a) scale 0-480 min, (b) scale 0-60 min, the solid line is calculated from the model

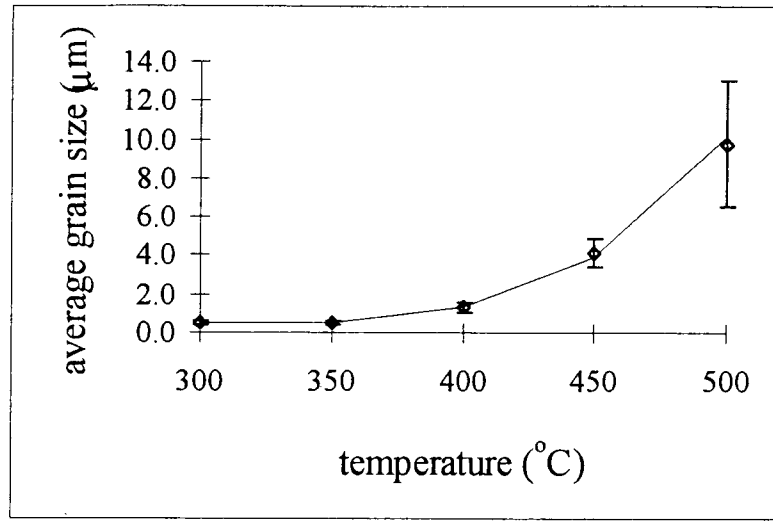

Figure 6.13 : Final grain size at each sintering temperature, the solid line is calculated from the model

The models agree very well with the experimental results. There is still some disagreement between calculated values and measured values in the early part of sintering at 450 and 500 ^{0}C as seen in Figure 6.11 (b). The model predicts a faster densification rate in the first few minutes of sintering. The initial stage ends within 1 minute at 450 ^{0}C as predicted by the model while the experimental result indicates that the sintering was still in the initial stage after 3 minutes. This implies that during the sintering test, the bulk of a pellet was still cold by the time the surface of the pellet reached the sintering temperature. Therefore, the pellets did not shrink as much as they should have been in the beginning of the sintering. The effect of temperature gradient in the pellet becomes more important at higher sintering temperatures. This effect also results in slow grain growth rate in the early part of high temperature sintering. From

figure 6.12 (b), at 500 ^{0}C, the grain growth rate predicted by the model is higher than the experimental result in the early part of the sintering.

The other deviation of the calculated value from the measured value is the unusually high final density predicted by the model at 400 ^{0}C. This is postulated to be the result of unclear transition point between the intermediate stage and the final stage. In other word, the intermediate stage model was applied without taking into account the transition point into the final stage.

The model was also tested against the experimental result using different initial pellet density as shown in Figure 6.14.

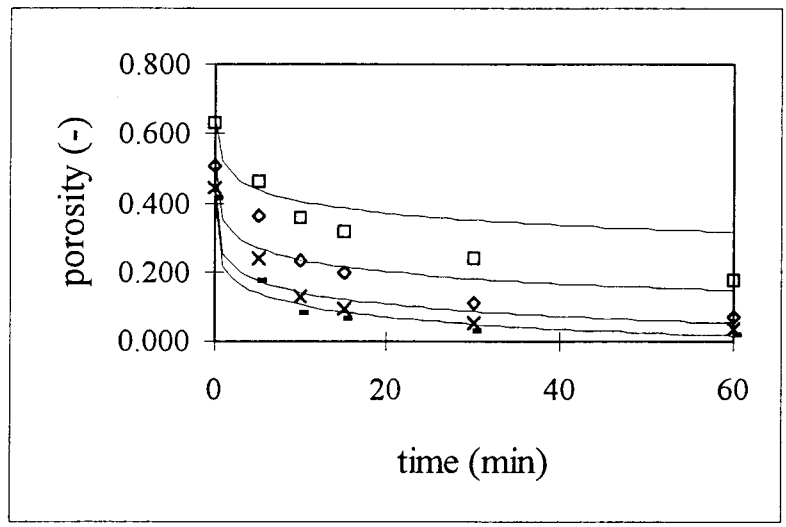

Figure 6.14 : The effect of different pellet green density on the sintering at 450 ^{0}C, the solid line is calculated from the model

It can be seen that the model deviates greatly from the experimental result when low initial pellet density was used. The following interpretations were made,

- The model ignores the effect of the particles rearrangement in the less packed specimen.
- Grain growth behavior is different for the different packing configurations, making the sinterability different. From the intermediate stage sintering model,

$$\frac{dP}{dt} = \frac{-K_2}{T}\left[\frac{1}{m(t-t_0)+G_0^3}\right] \qquad 6.5$$

if the grain growth rate is high, the high rate constant m will result in low densification rate.

CHAPTER 7
CONCLUSION

The following conclusions can be drawn:

- Each stage of sintering of low chloride fume dust was identified by the study of microstructural development.
- Semi-empirical kinetic models were developed to predict the linear shrinkage in the initial stage sintering, and the grain growth and densification rate in the intermediate stage sintering of well-packed low chloride dusts.
- The apparent activation energy for the initial stage sintering is 54.5 ± 21.7 kcal/mol.
- The apparent activation energy for the intermediate stage sintering is 56.0 ± 31.3 kcal/mol.
- The controlled mechanism is volume diffusion for both stages of sintering.
- The apparent activation energy for the grain growth process is 63.0 ± 20.1 kcal/mol.
- The models for the sintering of the specific fume dust which is well packed and sintered in air are shown here:

7.1 Initial Stage Sintering Model

$$P = 1 - \left(1 - P_{\text{unsintered}}\right)\left(1 - \frac{\Delta L}{L_0}\right)^{-3}$$

$$\frac{\Delta L}{L_0} = \left[\frac{K_1}{TG_0^3}\right]^{0.4} t^{0.4}$$

$$K_1 = K_1' e^{\frac{-E_1}{RT}}$$

7.2 Intermediate Stage Sintering Model

$$G^3 - G_0^3 = m(t - t_0)$$

$$P = \frac{-K_2}{mT} Ln\left[\frac{m(t - t_0) + G_0^3}{G_0^3}\right] + P_0$$

$$m = m_0 e^{\frac{E_G}{RT}}$$

where	K_1'	=	8.71×10^3	[K-cm^3/min]
	E_1	=	227.9	[kJ/mol]
	K_2'	=	3.99×10^5	[K-cm^3/min]
	E_2	=	234.5	[kJ/mol]
	m_0	=	1.42	[cm^3/min]
	E_G	=	263.6	[kJ/mol]
	$P_{unsintered}$	=	0.430	
	P_0	=	0.218	
	G_0	=	0.5×10^{-4}	[cm]

t_0	=	time when the initial stage sintering ends or the linear shrinkage reaches 0.1	[min]
R	=	0.008314	[kJ/mol-K]
t	=	time	[min]
T	=	temperature	[K]

- The model did not apply well to the sintering of less-packed specimens due to some unidentified side effects.
- High contents of chloride species can retard the densification rate and lower the sinterability in the initial stage sintering.
- High contents of chloride species can retard the grain growth rate in the intermediate stage sintering, resulting in a more extensive densification process.

BIBLIOGRAPHY

1. Tran, H.N., "How does a kraft recovery boiler become plugged?", TAPPI Journal, 68(11) : 102-106 (1986)

2. Tran, H.N., Barham, D., and Reeve, D.W., "Sintering of fireside deposits and its impact on plugging in kraft recovery boiler", TAPPI Journal, 70(4) : 109-113 (1988)

3. Kingery, W.D., Bowen, H.K., and Uhlmann, D.R., "Introduction to Ceramics, 2nd Edition", p.448-490, John Wiley & Sons, 1976

4. Pask, J.A., "Grain boundaries in sintering", Science of Sintering, p.381-393, Plenum Press, 1989

5. Readey, D.W., "Mass transport and sintering in impure ionic solids", Journal of American Ceramic Society, 49(17) : 366-369 (1966)

6. Johnson, D.L. and Cutler, I.B., "Diffusion sintering : I. Initial stage sintering models and their application to shrinkage of powder compacts", Journal of American Ceramic Society, 46(11) : 541-545 (1963)

7. Kingery, W.D. and Berg, M., "Study of the initial stages of sintering solids by viscous flow, evaporation-condensation, and self-diffusion", Journal of Applied Physics, 26(10) : 1205-1212 (1955)

8. Coble, R.L., "Initial sintering of alumina and hematite", Journal of American Ceramic Society, 41(2) : 55-62 (1958)

9. Johnson, D.L. and Clarke, T.M., "Grain boundary and volume diffusion in the sintering of silver", Acta Metallurgica, 12(10) : 1173-1179 (1964)

10. Johnson, D.L., "New method of obtaining volume, grain-boundary, and surface diffusion coefficients from sintering data", Journal of Applied Physics, 40(1) : 192-200 (1969)

11. Gessinger, G.H., "Volume diffusion as densification rate-controlling step in sintering", Scripta METALLURGICA, 4(9) : 673-676 (1970)

12. Johnson, D.L., Discussion of "Volume diffusion as densification rate-controlling step in sintering", Scripta METALLURGICA, 4(9) : 677-680 (1970)

13. Wong, B. and Pask, J.A., "Models for kinetics of solid state sintering", Journal of American Ceramic Society, 64(3-4) : 138-141 (1979)

14. Swinkels, F.B. and Ashby, M.F., "A second report on sintering diagrams", Acta Metallurgica, 29(2) : 259-281 (1981)

15. Exner, H.E., "Neck shape and limiting GBD/SD ratios in solid state sintering", Acta Metallurgica, 35(3) : 587-591 (1987)

16. (a) Coble, R.L., "Sintering crystalline solid. I. Intermediate and final state diffusion models", Journal of Applied Physics, 32(5) : 787-792 (1961), (b) Coble, R.L., "Intermediate stage sintering : Modification and correction of a lattice-diffusion model", Journal of Applied Physics, 36(7) : 2327 (1965)

17. Yan, M.F., Cannon, R.M., and Bowen, H.K., "Grain boundary migration in ceramics", Ceramic Microstructure, p.276-307, Westview Press, 1976

18. Brook, R.J., Howlett, S.P., and SU XING WU, "The use of solid solution additives in sintering", Sintering-Theory and Practice, p.135-144, Elsevier Scientific Publishing Company, 1982

19. Johnson, D.L., "Recent development in the theoretical analysis of solid state sintering", Sintering-Theory and Practice, p.37-44, Elsevier Scientific Publishing Company, 1982

20. Sokiniemi, J.K., Pyykonen, J., Mikkanen, P., and Kauppinen, E.I., "Modelling alkali salt deposition on kraft recovery boiler heat exchangers", International Chemical Recovery Conference, Toronto, Ontario, Canada, 1995

21. Skrifvars, B., Hupa, M., and Hyoty, P., "Composition of recovery boiler dust and its effect on sintering", TAPPI Journal, 74(6) : 185-189

APPENDICES

APPENDIX A

EXPERIMENTAL DATA

Table A-1 : Experimental data for sintering of low chloride dust at 300 ^{0}C

Time	Before sintering				After sintering				Diameter	Weight
	Weight	Thickness	Diameter	Density	Weight	Thickness	Diameter	Density	change	loss
(min)	(g)	(mm)	(mm)	(g/cm^3)	(g)	(mm)	(mm)	(g/cm^3)	(%)	(%)
60	2.960	4.110	25.400	1.42	2.956	4.087	25.112	1.46	1.13	-0.14
60	2.981	4.100	25.400	1.43	2.979	4.077	25.112	1.48	1.13	-0.07
120	2.958	4.070	25.400	1.43	2.956	4.030	25.053	1.49	1.37	-0.07
120	2.969	4.060	25.400	1.44	2.965	4.027	25.044	1.49	1.40	-0.13
120	2.957	4.060	25.400	1.44	2.954	4.013	25.027	1.50	1.47	-0.10
240	2.958	4.080	25.400	1.43	2.953	4.023	24.900	1.51	1.97	-0.17
240	2.961	4.060	25.400	1.44	2.958	4.003	24.934	1.51	1.83	-0.10
240	2.962	4.070	25.400	1.44	2.958	4.020	24.960	1.50	1.73	-0.14
480	2.963	4.050	25.400	1.44	2.959	3.977	24.824	1.54	2.27	-0.13
480	2.959	4.030	25.400	1.45	2.955	3.947	24.833	1.55	2.23	-0.14
480	2.960	4.100	25.400	1.42	2.957	4.020	24.850	1.52	2.17	-0.10

Table A-2 : Experimental data for sintering of low chloride dust at 350 ^{0}C

Time	Before sintering				After sintering				Diameter	Weight
	Weight	Thickness	Diameter	Density	Weight	Thickness	Diameter	Density	change	loss
(min)	(g)	(mm)	(mm)	(g/cm^3)	(g)	(mm)	(mm)	(g/cm^3)	(%)	(%)
15	2.964	4.070	25.400	1.44	2.960	3.980	24.638	1.56	3.00	-0.13
15	2.962	4.050	25.400	1.44	2.958	3.967	24.663	1.56	2.90	-0.14
15	2.960	4.040	25.400	1.45	2.962	3.960	24.680	1.56	2.83	0.07
20	2.961	3.960	25.400	1.48	2.958	3.843	24.384	1.65	4.00	-0.10
20	2.966	4.070	25.400	1.44	2.962	3.937	24.443	1.60	3.77	-0.13
20	2.965	4.040	25.400	1.45	2.962	3.923	24.511	1.60	3.50	-0.10
30	2.963	4.030	25.400	1.45	2.960	3.883	24.249	1.65	4.53	-0.10
30	2.964	4.050	25.400	1.44	2.961	3.910	24.249	1.64	4.53	-0.10
30	2.961	4.070	25.400	1.44	2.957	3.930	24.359	1.61	4.10	-0.14
45	2.964	4.040	25.400	1.45	2.959	3.870	24.028	1.69	5.40	-0.17
45	2.966	4.090	25.400	1.43	2.962	3.920	24.105	1.66	5.10	-0.13
45	2.964	4.020	25.400	1.46	2.960	3.883	24.172	1.66	4.83	-0.13
60	2.960	4.040	25.400	1.45	2.955	3.880	24.028	1.68	5.40	-0.17
60	2.959	4.080	25.400	1.43	2.955	3.897	24.011	1.67	5.47	-0.14
60	2.962	4.080	25.400	1.43	2.957	3.917	24.062	1.66	5.27	-0.17
90	2.966	4.020	25.400	1.46	2.961	3.807	23.647	1.77	6.90	-0.17
90	2.963	4.030	25.400	1.45	2.958	3.807	23.690	1.76	6.73	-0.17
90	2.964	4.020	25.400	1.46	2.960	3.820	23.757	1.75	6.47	-0.13
120	2.961	4.090	25.400	1.43	2.957	3.843	23.512	1.77	7.43	-0.14
120	2.962	4.010	25.400	1.46	2.958	3.777	23.546	1.80	7.30	-0.14
120	2.965	4.100	25.400	1.43	2.960	3.877	23.630	1.74	6.97	-0.17
180	2.964	4.030	25.400	1.45	2.959	3.760	23.360	1.84	8.03	-0.17
180	2.955	4.000	25.400	1.46	2.950	3.753	23.495	1.81	7.50	-0.17
180	2.967	4.070	25.400	1.44	2.962	3.807	23.376	1.81	7.97	-0.17
480	2.967	4.120	25.400	1.42	2.961	3.773	22.818	1.92	10.17	-0.20
480	2.970	4.190	25.400	1.40	2.964	3.850	22.860	1.88	10.00	-0.20
480	2.967	4.140	25.400	1.41	2.962	3.820	23.012	1.86	9.40	-0.17

Table A-3 : Experimental data for sintering of low chloride dust at 400 ^{0}C

Time	Before sintering				After sintering				Diameter	Weight
	Weight	Thickness	Diameter	Density	Weight	Thickness	Diameter	Density	change	loss
(min)	(g)	(mm)	(mm)	(g/cm^3)	(g)	(mm)	(mm)	(g/cm^3)	(%)	(%)
0	2.950	4.080	25.400	1.43	2.946	4.080	25.358	1.43	0.17	-0.14
0	2.968	4.140	25.400	1.41	2.954	4.137	25.349	1.41	0.20	-0.47
0	2.970	4.130	25.400	1.42	2.957	4.130	25.341	1.42	0.23	-0.44
5	2.962	4.110	25.400	1.42	2.958	3.933	23.791	1.69	6.33	-0.14
5	2.960	4.100	25.400	1.42	2.956	3.937	23.961	1.67	5.67	-0.14
5	2.957	4.070	25.400	1.43	2.953	3.917	23.927	1.68	5.80	-0.14
7	2.959	4.050	25.400	1.44	2.954	3.833	23.546	1.77	7.30	-0.17
7	2.958	4.090	25.400	1.43	2.952	3.883	23.673	1.73	6.80	-0.20
7	2.963	4.080	25.400	1.43	2.957	3.900	23.707	1.72	6.67	-0.20
10	2.959	4.090	25.400	1.43	2.952	3.807	23.114	1.85	9.00	-0.24
10	2.956	4.060	25.400	1.44	2.951	3.793	23.292	1.83	8.30	-0.17
10	2.957	4.120	25.400	1.42	2.951	3.870	23.334	1.78	8.13	-0.20
15	2.957	4.040	25.400	1.44	2.952	3.663	22.598	2.01	11.03	-0.17
15	2.964	4.060	25.400	1.44	2.959	3.707	22.750	1.96	10.43	-0.17
15	2.954	4.050	25.400	1.44	2.950	3.720	22.809	1.94	10.20	-0.14
20	2.959	4.090	25.400	1.43	2.955	3.673	22.335	2.05	12.07	-0.14
20	2.969	4.080	25.400	1.44	2.964	3.687	22.394	2.04	11.83	-0.17
20	2.965	4.070	25.400	1.44	2.961	3.680	22.437	2.04	11.67	-0.13
30	2.959	4.090	25.400	1.43	2.954	3.667	22.208	2.08	12.57	-0.17
30	2.959	4.100	25.400	1.42	2.953	3.667	22.149	2.09	12.80	-0.20
30	2.961	4.100	25.400	1.43	2.956	3.637	22.039	2.13	13.23	-0.17
30	2.964	4.120	25.400	1.42	2.960	3.673	22.022	2.12	13.30	-0.13
30	2.957	4.080	25.400	1.43	2.952	3.653	22.208	2.09	12.57	-0.17
30	2.963	4.100	25.400	1.43	2.957	3.677	22.310	2.06	12.17	-0.20
30	2.957	4.070	25.400	1.43	2.953	3.673	22.377	2.04	11.90	-0.14

Table A-3 : (continued)

Time	Before sintering				After sintering				Diameter	Weight
	Weight	Thickness	Diameter	Density	Weight	Thickness	Diameter	Density	change	loss
(min)	(g)	(mm)	(mm)	(g/cm^3)	(g)	(mm)	(mm)	(g/cm^3)	(%)	(%)
45	2.958	4.090	25.400	1.43	2.953	3.607	21.861	2.18	13.93	-0.17
45	2.966	4.090	25.400	1.43	2.961	3.650	21.971	2.14	13.50	-0.17
45	2.965	4.120	25.400	1.42	2.960	3.653	22.047	2.12	13.20	-0.17
60	2.963	4.100	25.400	1.43	2.958	3.587	21.717	2.23	14.50	-0.17
60	2.962	4.090	25.400	1.43	2.957	3.580	21.768	2.22	14.30	-0.17
60	2.967	4.080	25.400	1.44	2.958	3.580	21.683	2.24	14.63	-0.30
120	2.965	4.090	25.400	1.43	2.957	3.533	21.480	2.31	15.43	-0.27
120	2.961	4.040	25.400	1.45	2.955	3.520	21.573	2.30	15.07	-0.20
120	2.967	4.110	25.400	1.42	2.962	3.577	21.590	2.26	15.00	-0.17
480	2.969	4.170	25.400	1.41	2.963	3.553	21.040	2.40	17.17	-0.20
480	2.964	4.130	25.400	1.42	2.957	3.530	21.074	2.40	17.03	-0.24
480	2.972	4.120	25.400	1.42	2.965	3.537	21.116	2.39	16.87	-0.24
480	2.965	4.150	25.400	1.41	2.959	3.510	20.980	2.44	17.40	-0.20
480	2.967	4.150	25.400	1.41	2.960	3.500	20.955	2.45	17.50	-0.24
480	2.964	4.120	25.400	1.42	2.967	3.520	20.989	2.44	17.37	0.10

Table A-4 : Experimental data for sintering of low chloride dust at 450 ^{0}C

Time	Before sintering				After sintering				Diameter	Weight
	Weight	Thickness	Diameter	Density	Weight	Thickness	Diameter	Density	change	loss
(min)	(g)	(mm)	(mm)	(g/cm^3)	(g)	(mm)	(mm)	(g/cm^3)	(%)	(%)
0	2.964	4.160	25.400	1.41	2.950	4.120	24.934	1.47	1.83	-0.47
0	2.962	4.130	25.400	1.42	2.959	4.107	25.044	1.46	1.40	-0.10
0	2.966	4.110	25.400	1.42	2.952	4.093	25.070	1.46	1.30	-0.47
3	2.960	4.100	25.400	1.42	2.956	3.880	23.131	1.81	8.93	-0.14
3	2.962	4.110	25.400	1.42	2.957	3.890	23.326	1.78	8.17	-0.17
3	2.961	4.070	25.400	1.44	2.951	3.873	23.165	1.81	8.80	-0.34
4	2.962	4.110	25.400	1.42	2.954	3.740	22.377	2.01	11.90	-0.27
4	2.959	4.060	25.400	1.44	2.953	3.723	22.606	1.98	11.00	-0.20
4	2.966	4.040	25.400	1.45	2.961	3.717	22.555	1.99	11.20	-0.17
5	2.960	4.080	25.400	1.43	2.955	3.667	22.098	2.10	13.00	-0.17
5	2.964	4.120	25.400	1.42	2.959	3.723	22.301	2.03	12.20	-0.17
5	2.965	4.070	25.400	1.44	2.960	3.653	22.310	2.07	12.17	-0.17
7	2.965	4.010	25.400	1.46	2.960	3.543	21.937	2.21	13.63	-0.17
7	2.966	4.060	25.400	1.44	2.957	3.607	22.098	2.14	13.00	-0.30
7	2.963	4.060	25.400	1.44	2.958	3.613	22.090	2.14	13.03	-0.17
10	2.965	4.060	25.400	1.44	2.960	3.537	21.480	2.31	15.43	-0.17
10	2.963	4.020	25.400	1.45	2.957	3.507	21.590	2.30	15.00	-0.20
10	2.969	4.060	25.400	1.44	2.963	3.537	21.590	2.29	15.00	-0.20
15	2.964	4.050	25.400	1.44	2.956	3.497	21.328	2.37	16.03	-0.27
15	2.962	4.060	25.400	1.44	2.956	3.520	21.344	2.35	15.97	-0.20
15	2.967	4.060	25.400	1.44	2.963	3.527	21.344	2.35	15.97	-0.13
20	2.956	4.090	25.400	1.43	2.952	3.467	21.141	2.43	16.77	-0.14
20	2.964	4.040	25.400	1.45	2.959	3.453	21.260	2.41	16.30	-0.17
20	2.967	4.090	25.400	1.43	2.962	3.510	21.234	2.38	16.40	-0.17
30	2.969	4.050	25.400	1.45	2.964	3.453	21.184	2.44	16.60	-0.17
30	2.964	4.100	25.400	1.43	2.959	3.487	21.082	2.43	17.00	-0.17
30	2.963	4.060	25.400	1.44	2.956	3.473	21.158	2.42	16.70	-0.24

Table A-4 : (continued)

Time	Before sintering				After sintering				Diameter	Weight
	Weight	Thickness	Diameter	Density	Weight	Thickness	Diameter	Density	change	loss
(min)	(g)	(mm)	(mm)	(g/cm^3)	(g)	(mm)	(mm)	(g/cm^3)	(%)	(%)
60	2.964	4.090	25.400	1.43	2.959	3.467	20.997	2.46	17.33	-0.17
60	2.968	4.030	25.400	1.45	2.963	3.413	21.082	2.49	17.00	-0.17
60	2.965	4.040	25.400	1.45	2.960	3.437	21.057	2.47	17.10	-0.17
60	2.966	4.030	25.400	1.45	2.960	3.447	21.057	2.47	17.10	-0.20
60	2.963	4.020	25.400	1.45	2.958	3.427	21.082	2.47	17.00	-0.17
60	2.967	4.150	25.400	1.41	2.961	3.517	20.887	2.46	17.77	-0.20
60	2.971	4.160	25.400	1.41	2.965	3.533	20.879	2.45	17.80	-0.20
60	2.963	4.130	25.400	1.42	2.957	3.487	20.997	2.45	17.33	-0.20
480	2.967	4.130	25.400	1.42	2.961	3.470	20.820	2.51	18.03	-0.20
480	2.963	4.210	25.400	1.39	2.957	3.527	20.684	2.50	18.57	-0.20

Table A-4 : (continued)

Time	Before sintering				After sintering				Diameter	Weight
	Weight	Thickness	Diameter	Density	Weight	Thickness	Diameter	Density	change	loss
(min)	(g)	(mm)	(mm)	(g/cm^3)	(g)	(mm)	(mm)	(g/cm^3)	(%)	(%)
0	2.972	4.380	25.400	1.34	2.965	4.363	25.011	1.38	1.53	-0.24
0	2.970	4.340	25.400	1.35	2.967	4.317	25.129	1.39	1.07	-0.10
0	2.969	4.300	25.400	1.36	2.966	4.280	25.138	1.40	1.03	-0.10
5	2.968	4.280	25.400	1.37	2.964	3.880	22.352	1.95	12.00	-0.13
5	2.970	4.290	25.400	1.37	2.965	3.923	22.657	1.87	10.80	-0.17
5	2.969	4.260	25.400	1.38	2.963	3.903	22.521	1.91	11.33	-0.20
10	2.970	4.280	25.400	1.37	2.964	3.723	21.463	2.20	15.50	-0.20
10	2.969	4.290	25.400	1.37	2.964	3.733	21.565	2.17	15.10	-0.17
10	2.970	4.290	25.400	1.37	2.964	3.737	21.590	2.17	15.00	-0.20
15	2.971	4.310	25.400	1.36	2.964	3.660	21.192	2.30	16.57	-0.24
15	2.968	4.240	25.400	1.38	2.963	3.637	21.311	2.28	16.10	-0.17
15	2.969	4.300	25.400	1.36	2.963	3.717	21.319	2.23	16.07	-0.20
30	2.969	4.310	25.400	1.36	2.964	3.620	20.836	2.40	17.97	-0.17
30	2.967	4.290	25.400	1.36	2.962	3.620	20.879	2.39	17.80	-0.17
30	2.967	4.290	25.400	1.36	2.962	3.647	20.980	2.35	17.40	-0.17
60	2.973	4.320	25.400	1.36	2.964	3.593	20.735	2.44	18.37	-0.30
60	2.969	4.300	25.400	1.36	2.963	3.613	20.786	2.42	18.17	-0.20
60	2.973	4.340	25.400	1.35	2.967	3.633	20.803	2.40	18.10	-0.20

Table A-4 : (continued)

Time	Before sintering				After sintering				Diameter	Weight
	Weight	Thickness	Diameter	Density	Weight	Thickness	Diameter	Density	change	loss
(min)	(g)	(mm)	(mm)	(g/cm^3)	(g)	(mm)	(mm)	(g/cm^3)	(%)	(%)
0	2.980	4.860	25.400	1.21	2.977	4.830	25.078	1.25	1.27	-0.10
0	2.979	4.900	25.400	1.20	2.976	4.863	25.112	1.24	1.13	-0.10
0	2.978	4.960	25.400	1.18	2.975	4.933	25.070	1.22	1.30	-0.10
5	2.980	5.050	25.400	1.16	2.975	4.587	22.445	1.64	11.63	-0.17
5	2.979	5.000	25.400	1.18	2.973	4.597	22.860	1.58	10.00	-0.20
5	2.980	5.010	25.400	1.17	2.975	4.597	22.691	1.60	10.67	-0.17
10	2.979	4.950	25.400	1.19	2.974	4.293	21.251	1.95	16.33	-0.17
10	2.981	4.930	25.400	1.19	2.975	4.297	21.514	1.90	15.30	-0.20
10	2.978	4.980	25.400	1.18	2.973	4.320	21.539	1.89	15.20	-0.17
15	2.984	5.040	25.400	1.17	2.979	4.243	20.794	2.07	18.13	-0.17
15	2.980	4.970	25.400	1.18	2.976	4.203	21.014	2.04	17.27	-0.13
15	2.982	4.940	25.400	1.19	2.977	4.207	21.539	1.94	15.20	-0.17
30	2.979	4.900	25.400	1.20	2.974	4.033	20.422	2.25	19.60	-0.17
30	2.979	4.880	25.400	1.20	2.974	4.063	20.498	2.22	19.30	-0.17
30	2.980	4.840	25.400	1.22	2.974	4.043	20.574	2.21	19.00	-0.20
60	2.979	4.960	25.400	1.19	2.973	4.010	20.074	2.34	20.97	-0.20
60	2.982	4.950	25.400	1.19	2.976	4.013	20.125	2.33	20.77	-0.20
60	2.977	4.900	25.400	1.20	2.971	3.990	20.210	2.32	20.43	-0.20

Table A-4 : (continued)

Time	Before sintering				After sintering				Diameter	Weight
	Weight	Thickness	Diameter	Density	Weight	Thickness	Diameter	Density	change	loss
(min)	(g)	(mm)	(mm)	(g/cm^3)	(g)	(mm)	(mm)	(g/cm^3)	(%)	(%)
0	2.986	6.550	25.400	0.90	2.977	4.830	25.078	0.94	1.80	-0.13
0	2.987	6.600	25.400	0.89	2.976	4.863	25.112	0.93	1.40	-0.07
0	2.989	6.650	25.400	0.89	2.975	4.933	25.070	0.93	1.97	-0.10
5	2.985	6.600	25.400	0.89	2.975	4.587	22.445	1.41	14.70	-0.17
5	2.983	6.740	25.400	0.87	2.973	4.597	22.860	1.29	12.97	-0.13
5	2.984	6.650	25.400	0.89	2.975	4.597	22.691	1.34	13.77	-0.13
10	2.985	6.810	25.400	0.87	2.974	4.293	21.251	1.64	20.00	-0.20
10	2.983	6.800	25.400	0.87	2.975	4.297	21.514	1.59	18.97	-0.17
10	2.986	6.750	25.400	0.87	2.973	4.320	21.539	1.60	19.17	-0.17
15	2.984	6.810	25.400	0.86	2.979	4.243	20.794	1.74	21.43	-0.20
15	2.985	6.790	25.400	0.87	2.976	4.203	21.014	1.70	20.90	-0.20
15	2.983	6.750	25.400	0.87	2.977	4.207	21.539	1.69	20.57	-0.13
30	2.983	6.660	25.400	0.88	2.974	4.033	20.422	1.94	24.00	-0.57
30	2.983	6.800	25.400	0.87	2.974	4.063	20.498	1.92	23.90	-0.20
30	2.985	6.780	25.400	0.87	2.974	4.043	20.574	1.87	23.23	-0.17
60	2.986	6.430	25.400	0.92	2.973	4.010	20.074	2.11	25.00	-0.17
60	2.987	6.480	25.400	0.91	2.976	4.013	20.125	2.10	25.00	-0.17
60	2.988	6.690	25.400	0.88	2.971	3.990	20.210	2.00	24.90	-0.10

Table A-5 : Experimental data for sintering of low chloride dust at 500 ^{0}C

Time	Before sintering				After sintering				Diameter	Weight
	Weight	Thickness	Diameter	Density	Weight	Thickness	Diameter	Density	change	loss
(min)	(g)	(mm)	(mm)	(g/cm^3)	(g)	(mm)	(mm)	(g/cm^3)	(%)	(%)
0	2.965	4.090	25.400	1.43	2.958	4.020	24.392	1.57	3.97	-0.24
0	2.963	4.100	25.400	1.43	2.958	4.040	24.587	1.54	3.20	-0.17
0	2.968	4.110	25.400	1.43	2.964	4.057	24.452	1.56	3.73	-0.13
1	2.963	4.100	25.400	1.43	2.958	3.837	22.775	1.89	10.33	-0.17
1	2.966	4.100	25.400	1.43	2.961	3.890	23.233	1.80	8.53	-0.17
1	2.965	4.120	25.400	1.42	2.961	3.900	23.241	1.79	8.50	-0.13
1	2.965	4.110	25.400	1.42	2.960	3.843	22.784	1.89	10.30	-0.17
1	2.965	4.120	25.400	1.42	2.961	3.897	23.063	1.82	9.20	-0.13
2	2.955	4.070	25.400	1.43	2.950	3.633	22.047	2.13	13.20	-0.17
2	2.975	4.150	25.400	1.41	2.970	3.743	22.115	2.07	12.93	-0.17
2	2.970	4.140	25.400	1.42	2.964	3.727	22.005	2.09	13.37	-0.20
2	2.951	4.070	25.400	1.43	2.945	3.683	22.157	2.07	12.77	-0.20
2	2.961	4.100	25.400	1.43	2.952	3.720	22.115	2.07	12.93	-0.30
3	2.961	4.080	25.400	1.43	2.956	3.607	21.776	2.20	14.27	-0.17
3	2.963	4.120	25.400	1.42	2.958	3.653	21.912	2.15	13.73	-0.17
3	2.960	4.070	25.400	1.44	2.954	3.590	21.751	2.21	14.37	-0.20
3	2.962	4.100	25.400	1.43	2.956	3.647	21.878	2.16	13.87	-0.20
3	2.958	4.070	25.400	1.43	2.950	3.600	21.836	2.19	14.03	-0.27
5	2.958	4.100	25.400	1.42	2.952	3.523	21.344	2.34	15.97	-0.20
5	2.954	4.100	25.400	1.42	2.948	3.493	21.302	2.37	16.13	-0.20
5	2.960	4.110	25.400	1.42	2.954	3.513	21.268	2.37	16.27	-0.20
7	2.963	4.050	25.400	1.44	2.958	3.450	21.090	2.45	16.97	-0.17
7	2.960	3.960	25.400	1.48	2.954	3.400	21.285	2.44	16.20	-0.20
7	2.961	4.020	25.400	1.45	2.955	3.437	21.167	2.44	16.67	-0.20
7	2.958	4.100	25.400	1.42	2.952	3.490	21.048	2.43	17.13	-0.20
7	2.968	4.090	25.400	1.43	2.962	3.483	21.065	2.44	17.07	-0.20
7	2.965	4.060	25.400	1.44	2.958	3.450	21.099	2.45	16.93	-0.24

Table A-5 : (continued)

Time	Before sintering				After sintering				Diameter	Weight
	Weight	Thickness	Diameter	Density	Weight	Thickness	Diameter	Density	change	loss
(min)	(g)	(mm)	(mm)	(g/cm^3)	(g)	(mm)	(mm)	(g/cm^3)	(%)	(%)
10	2.964	4.040	25.400	1.45	2.958	3.443	21.099	2.46	16.93	-0.20
10	2.966	4.120	25.400	1.42	2.960	3.473	21.040	2.45	17.17	-0.20
10	2.962	4.140	25.400	1.41	2.953	3.497	20.955	2.45	17.50	-0.30
15	2.962	4.080	25.400	1.43	2.956	3.470	20.896	2.48	17.73	-0.20
15	2.965	4.070	25.400	1.44	2.959	3.433	20.972	2.49	17.43	-0.20
15	3.021	4.160	25.400	1.43	3.016	3.520	21.040	2.46	17.17	-0.17
30	2.961	4.160	25.400	1.40	2.955	3.487	20.811	2.49	18.07	-0.20
30	2.962	4.070	25.400	1.44	2.955	3.437	20.921	2.50	17.63	-0.24
30	2.966	4.120	25.400	1.42	2.951	3.450	20.989	2.47	17.37	-0.51
60	2.963	4.170	25.400	1.40	2.950	3.510	20.803	2.47	18.10	-0.44
60	2.959	4.200	25.400	1.39	2.951	3.520	20.769	2.47	18.23	-0.27
60	2.970	4.190	25.400	1.40	2.962	3.503	20.794	2.49	18.13	-0.27
120	2.968	4.110	25.400	1.43	2.962	3.477	20.879	2.49	17.80	-0.20
120	2.962	4.110	25.400	1.42	2.956	3.487	20.904	2.47	17.70	-0.20
120	2.956	4.120	25.400	1.42	2.950	3.480	20.904	2.47	17.70	-0.20
240	2.966	4.130	25.400	1.42	2.961	3.487	20.836	2.49	17.97	-0.17
240	2.966	4.080	25.400	1.43	2.960	3.463	20.938	2.48	17.57	-0.20
240	2.965	4.180	25.400	1.40	2.955	3.500	20.786	2.49	18.17	-0.34
480	2.965	4.110	25.400	1.42	2.956	3.483	20.921	2.47	17.63	-0.30
480	2.967	4.140	25.400	1.41	2.960	3.470	20.836	2.50	17.97	-0.24
480	2.969	4.120	25.400	1.42	2.958	3.470	20.896	2.49	17.73	-0.37
480	2.962	4.040	25.400	1.45	2.956	3.423	21.057	2.48	17.10	-0.20
480	2.961	4.130	25.400	1.41	2.949	3.473	20.879	2.48	17.80	-0.41
480	2.965	4.080	25.400	1.43	2.958	3.453	20.913	2.49	17.67	-0.24

Table A-6 : Experimental data for sintering of low chloride dust at 550 ^{0}C

Time	Before sintering				After sintering				Diameter	Weight
	Weight	Thickness	Diameter	Density	Weight	Thickness	Diameter	Density	change	loss
(min)	(g)	(mm)	(mm)	(g/cm^3)	(g)	(mm)	(mm)	(g/cm^3)	(%)	(%)
30	2.975	4.090	25.400	1.44	2.919	3.660	21.548	2.19	15.17	-1.88
30	2.977	4.060	25.400	1.45	2.952	3.647	21.607	2.21	14.93	-0.84
30	2.974	4.060	25.400	1.45	2.952	3.663	21.539	2.21	15.20	-0.74
60	2.976	4.120	25.400	1.43	2.894	3.680	21.539	2.16	15.20	-2.76
60	2.972	4.070	25.400	1.44	2.944	3.623	21.522	2.23	15.27	-0.94
60	2.977	4.100	25.400	1.43	2.951	3.650	21.531	2.22	15.23	-0.87

Table A-7 : Experimental data for sintering of high chloride dust at 350 ^{0}C

Time	Before sintering				After sintering				Diameter	Weight
	Weight	Thickness	Diameter	Density	Weight	Thickness	Diameter	Density	change	loss
(min)	(g)	(mm)	(mm)	(g/cm^3)	(g)	(mm)	(mm)	(g/cm^3)	(%)	(%)
30	2.975	4.950	25.400	1.19	2.970	4.900	25.146	1.22	1.00	-0.17
30	2.976	5.050	25.400	1.16	2.971	5.007	25.163	1.19	0.93	-0.17
30	2.979	4.980	25.400	1.18	2.973	4.943	25.197	1.21	0.80	-0.20
60	2.977	5.030	25.400	1.17	2.973	4.970	25.053	1.21	1.37	-0.13
60	2.973	4.970	25.400	1.18	2.969	4.910	25.070	1.23	1.30	-0.13
60	2.973	4.990	25.400	1.18	2.967	4.947	25.112	1.21	1.13	-0.20
120	2.972	5.030	25.400	1.17	2.967	4.963	24.917	1.23	1.90	-0.17
120	2.972	4.890	25.400	1.20	2.964	4.817	24.867	1.27	2.10	-0.27
120	2.976	5.030	25.400	1.17	2.970	4.950	24.867	1.24	2.10	-0.20
240	2.977	5.000	25.400	1.18	2.972	4.887	24.748	1.26	2.57	-0.17
240	2.975	5.030	25.400	1.17	2.970	4.927	24.757	1.25	2.53	-0.17
240	2.975	4.940	25.400	1.19	2.970	4.830	24.782	1.27	2.43	-0.17
480	2.968	5.050	25.400	1.16	2.962	4.883	24.384	1.30	4.00	-0.20
480	2.967	5.050	25.400	1.16	2.961	4.867	24.282	1.31	4.40	-0.20
480	2.969	4.940	25.400	1.19	2.962	4.737	24.164	1.36	4.87	-0.24

Table A-8 : Experimental data for sintering of high chloride dust at 400 ^{0}C

Time	Before sintering				After sintering				Diameter	Weight
	Weight	Thickness	Diameter	Density	Weight	Thickness	Diameter	Density	change	loss
(min)	(g)	(mm)	(mm)	(g/cm^3)	(g)	(mm)	(mm)	(g/cm^3)	(%)	(%)
0	2.978	5.050	25.400	1.16	2.976	5.030	25.400	1.17	0.00	-0.07
0	2.978	4.900	25.400	1.20	2.976	4.900	25.383	1.20	0.07	-0.07
0	2.977	4.960	25.400	1.18	2.975	4.960	25.383	1.19	0.07	-0.07
5	2.976	4.910	25.400	1.20	2.971	4.857	25.027	1.24	1.47	-0.17
5	2.974	4.870	25.400	1.21	2.971	4.833	25.146	1.24	1.00	-0.10
5	2.977	5.020	25.400	1.17	2.974	4.977	25.112	1.21	1.13	-0.10
10	2.977	4.970	25.400	1.18	2.973	4.833	24.587	1.30	3.20	-0.13
10	2.978	4.930	25.400	1.19	2.974	4.823	24.697	1.29	2.77	-0.13
10	2.978	5.050	25.400	1.16	2.974	4.937	24.680	1.26	2.83	-0.13
15	2.974	4.890	25.400	1.20	2.969	4.730	24.257	1.36	4.50	-0.17
15	2.976	5.040	25.400	1.17	2.972	4.860	24.384	1.31	4.00	-0.13
15	2.973	5.040	25.400	1.16	2.968	4.873	24.409	1.30	3.90	-0.17
20	2.977	4.910	25.400	1.20	2.974	4.697	24.105	1.39	5.10	-0.10
20	2.975	5.050	25.400	1.16	2.971	4.853	24.206	1.33	4.70	-0.13
20	2.978	4.950	25.400	1.19	2.974	4.757	24.274	1.35	4.43	-0.13
30	2.978	5.030	25.400	1.17	2.974	4.737	23.749	1.42	6.50	-0.13
30	2.977	4.990	25.400	1.18	2.973	4.740	23.859	1.40	6.07	-0.13
30	2.975	4.990	25.400	1.18	2.971	4.650	23.884	1.43	5.97	-0.13
60	2.975	4.900	25.400	1.20	2.971	4.570	23.419	1.51	7.80	-0.13
60	2.977	4.860	25.400	1.21	2.973	4.533	23.554	1.51	7.27	-0.13
60	2.978	4.950	25.400	1.19	2.974	4.643	23.630	1.46	6.97	-0.13
120	2.977	4.860	25.400	1.21	2.973	4.493	23.148	1.57	8.87	-0.13
120	2.977	4.910	25.400	1.20	2.973	4.520	23.122	1.57	8.97	-0.13
120	2.977	4.850	25.400	1.21	2.972	4.473	23.139	1.58	8.90	-0.17
480	2.967	4.880	25.400	1.20	2.956	4.290	21.929	1.82	13.67	-0.37
480	2.970	4.890	25.400	1.20	2.962	4.280	21.836	1.85	14.03	-0.27
480	2.965	5.000	25.400	1.17	2.958	4.367	21.734	1.83	14.43	-0.24

Table A-9 : Experimental data for sintering of high chloride dust at 450 ^{0}C

Time	Before sintering				After sintering				Diameter	Weight
	Weight	Thickness	Diameter	Density	Weight	Thickness	Diameter	Density	change	loss
(min)	(g)	(mm)	(mm)	(g/cm^3)	(g)	(mm)	(mm)	(g/cm^3)	(%)	(%)
0	2.973	4.940	25.400	1.19	2.971	4.917	25.180	1.21	0.87	-0.07
0	2.973	4.910	25.400	1.19	2.969	4.890	25.197	1.22	0.80	-0.13
0	2.972	5.060	25.400	1.16	2.969	5.023	25.163	1.19	0.93	-0.10
5	2.971	5.020	25.400	1.17	2.968	4.697	23.376	1.47	7.97	-0.10
5	2.973	5.010	25.400	1.17	2.970	4.733	23.630	1.43	6.97	-0.10
5	2.971	4.970	25.400	1.18	2.968	4.710	23.757	1.42	6.47	-0.10
7	2.977	4.980	25.400	1.18	2.973	4.547	22.691	1.62	10.67	-0.13
7	2.972	4.880	25.400	1.20	2.968	4.483	23.029	1.59	9.33	-0.13
7	2.976	4.900	25.400	1.20	2.972	4.527	22.987	1.58	9.50	-0.13
10	2.976	5.050	25.400	1.16	2.972	4.510	22.318	1.68	12.13	-0.13
10	2.974	4.880	25.400	1.20	2.969	4.423	22.623	1.67	10.93	-0.17
10	2.977	5.040	25.400	1.17	2.972	4.563	22.648	1.62	10.83	-0.17
15	2.977	4.990	25.400	1.18	2.973	4.363	21.827	1.82	14.07	-0.13
15	2.976	4.950	25.400	1.19	2.972	4.360	22.106	1.78	12.97	-0.13
15	2.971	5.010	25.400	1.17	2.967	4.493	22.242	1.70	12.43	-0.13
30	2.970	4.870	25.400	1.20	2.965	4.097	21.040	2.08	17.17	-0.17
30	2.975	4.930	25.400	1.19	2.970	4.177	21.158	2.02	16.70	-0.17
30	2.973	4.910	25.400	1.19	2.968	4.170	21.124	2.03	16.83	-0.17
30	2.968	5.000	25.400	1.17	2.963	4.237	21.260	1.97	16.30	-0.17
30	2.974	4.940	25.400	1.19	2.970	4.250	21.463	1.93	15.50	-0.13
60	2.974	4.910	25.400	1.20	2.968	4.050	20.574	2.20	19.00	-0.20
60	2.976	5.010	25.400	1.17	2.971	4.137	20.659	2.14	18.67	-0.17
60	2.975	4.990	25.400	1.18	2.970	4.160	20.828	2.10	18.00	-0.17
480	2.963	5.040	25.400	1.16	2.955	4.120	19.820	2.32	21.97	-0.27
480	2.968	4.940	25.400	1.19	2.961	3.967	19.871	2.41	21.77	-0.24
480	2.964	4.890	25.400	1.20	2.956	3.943	19.931	2.40	21.53	-0.27

Table A-10 : Experimental data for sintering of high chloride dust at 500 ^{0}C

Time	Before sintering				After sintering				Diameter	Weight
	Weight	Thickness	Diameter	Density	Weight	Thickness	Diameter	Density	change	loss
(min)	(g)	(mm)	(mm)	(g/cm^3)	(g)	(mm)	(mm)	(g/cm^3)	(%)	(%)
0	2.968	4.910	25.400	1.19	2.962	4.873	24.994	1.24	1.60	-0.20
0	2.967	4.910	25.400	1.19	2.961	4.870	25.036	1.24	1.43	-0.20
0	2.970	4.980	25.400	1.18	2.965	4.937	24.867	1.24	2.10	-0.17
5	2.977	5.010	25.400	1.17	2.971	4.153	20.515	2.16	19.23	-0.20
5	2.977	4.900	25.400	1.20	2.972	4.113	20.955	2.10	17.50	-0.17
5	2.978	5.010	25.400	1.17	2.972	4.197	20.786	2.09	18.17	-0.20
7	2.977	5.020	25.400	1.17	2.971	4.073	20.269	2.26	20.20	-0.20
7	2.975	4.930	25.400	1.19	2.970	4.070	20.591	2.19	18.93	-0.17
7	2.974	4.930	25.400	1.19	2.968	4.057	20.540	2.21	19.13	-0.20
10	2.975	4.920	25.400	1.19	2.969	3.943	20.049	2.38	21.07	-0.20
10	2.975	5.040	25.400	1.16	2.969	3.997	19.981	2.37	21.33	-0.20
10	2.978	4.920	25.400	1.19	2.972	3.947	20.083	2.38	20.93	-0.20
30	2.976	4.940	25.400	1.19	2.971	3.917	19.897	2.44	21.67	-0.17
30	2.974	4.960	25.400	1.18	2.968	3.913	19.897	2.44	21.67	-0.20
30	2.974	5.030	25.400	1.17	2.968	3.957	19.812	2.43	22.00	-0.20
480	2.969	4.930	25.400	1.19	2.962	3.960	19.829	2.42	21.93	-0.24
480	2.969	4.870	25.400	1.20	2.962	3.917	19.905	2.43	21.63	-0.24
480	2.963	5.030	25.400	1.16	2.956	3.987	19.770	2.42	22.17	-0.24

Table A-11 : Experimental data for sintering of high chloride dust at 550 ^{0}C

Time	Before sintering				After sintering				Diameter	Weight
	Weight	Thickness	Diameter	Density	Weight	Thickness	Diameter	Density	change	loss
(min)	(g)	(mm)	(mm)	(g/cm^3)	(g)	(mm)	(mm)	(g/cm^3)	(%)	(%)
30	2.979	4.990	25.400	1.18	2.970	3.993	19.874	2.40	21.76	-0.30
30	2.975	4.900	25.400	1.20	2.966	3.953	20.024	2.38	21.17	-0.30
30	2.977	4.900	25.400	1.20	2.968	3.943	19.947	2.41	21.47	-0.30

APPENDIX B

MODELING OF TRAN'S SINTERING DATA

Tran *et al.*[2] conducted a series of sintering tests on a specific fume dust by measuring the volume and density changes of the pellets sintered in air at various temperatures for different time interval. Their results are shown in Figure B.1.

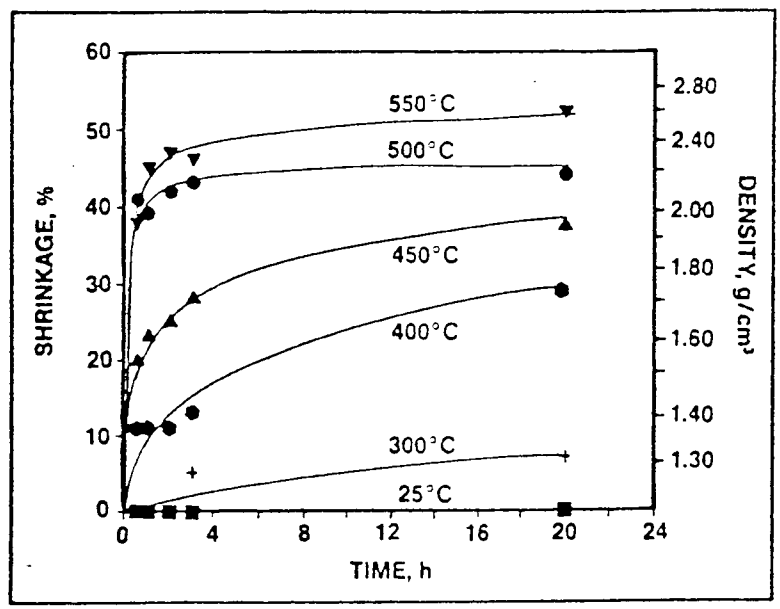

Figure B.1 : Tran's experimental data

They also studied the morphology changes of a number of sintered pellets. From the available information, we can conclude that the sintering of this particular dust at

300 and 400 ^{0}C was in the initial stage. For the sintering at 450, 500, and 550 ^{0}C, the initial stage sintering was not observed. The available grain growth data is shown in Table B-1.

Table B-1 : Tran's grain growth data

Temperature (^{0}C)	**Average grain size (μm)**	
	1 hr	**20 hrs**
450	2.5	6
500	6	8
550	6	-

From the volume shrinkage data, the linear shrinkage and porosity can be estimated using eq.(B-1) and eq.(B-2) respectively.

$$\frac{\Delta L}{L_0} = 1 - \left(1 - \frac{\Delta V}{V_0}\right)^{1/3} \qquad \text{B-1}$$

$$\frac{1 - P_0}{1 - P} = 1 - \frac{\Delta V}{V_0} \qquad \text{B-2}$$

where P_0 is the initial porosity which can be estimated by dividing the initial bulk density with the theoretical density which is about 2.6 g/cm^3.

It is not possible to fit the available data to both the initial stage and intermediate stage sintering model due to the following reasons;

- In the initial stage sintering, it is not possible to find the activation energy of the sintering process by using only two isotherms of the linear shrinkage data.
- There is not enough information for the grain growth data. Therefore, it is not possible to find the grain growth rate in the intermediate stage sintering.
- Without the grain growth rate, the modeling of the intermediate stage sintering is not possible.

APPENDIX C

PHASE DIAGRAM OF KCl-NaCl-K_2SO_4-Na_2SO_4 SYSTEM

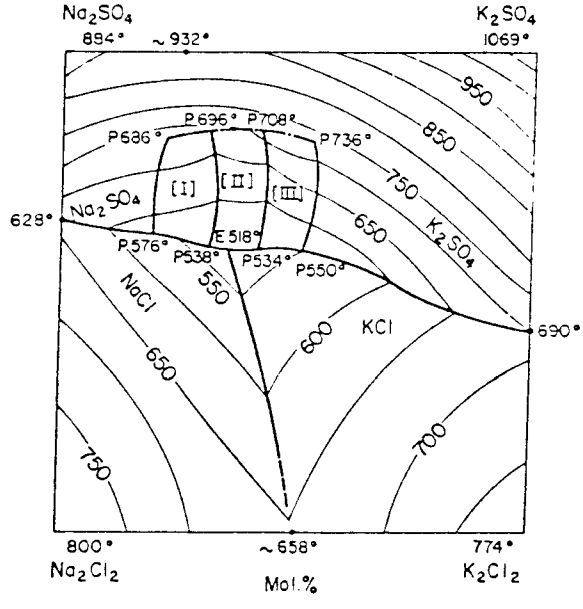

Figure C.1 : Phase diagram of KCl-NaCl-K_2SO_4-Na_2SO_4 system

APPENDIX D

GRAIN GROWTH DATA

Table D-1 : Grain growth data

Temperature (^{0}C)	Time (min)	Average grain size (μm)	S.D.
300	480	0.48	0.12
350	480	0.50	0.13
400	5	0.50	0.13
	10	0.50	0.15
	30	0.57	0.12
	60	0.70	0.17
	480	1.30	0.22
450	3	0.48	0.13
	7	0.75	0.22
	10	1.03	0.22
	15	1.27	0.18
	30	1.85	0.42
	60	2.40	0.48
	480	4.15	0.70
500	3	0.70	0.13
	5	1.30	0.42
	10	2.18	0.35
	480	9.80	3.30

APPENDIX E

FRACTIONAL DENSITY AND POROSITY DATA

Table E-1 : Fractional density and porosity of low chloride dust sintered at 300 ^{0}C

Time (min)	Fractional density (-)	Porosity (-)
60	0.582	0.418
60	0.588	0.412
120	0.593	0.407
120	0.596	0.404
120	0.597	0.403
240	0.601	0.399
240	0.603	0.397
240	0.600	0.400
480	0.613	0.387
480	0.616	0.384
480	0.605	0.395

Table E-2 : Fractional density and porosity of low chloride dust sintered at 350 ^{0}C

Time (min)	Fractional density (-)	Porosity (-)
15	0.622	0.378
15	0.622	0.378
15	0.623	0.377
20	0.657	0.343
20	0.639	0.361
20	0.638	0.362
30	0.658	0.342
30	0.654	0.346
30	0.644	0.356
45	0.672	0.328
45	0.660	0.340
45	0.662	0.338
60	0.670	0.330
60	0.668	0.332
60	0.662	0.338
90	0.706	0.294
90	0.703	0.297
90	0.697	0.303
120	0.707	0.293
120	0.717	0.283
120	0.694	0.306
180	0.732	0.268
180	0.723	0.277
180	0.723	0.277
480	0.765	0.235
480	0.748	0.252
480	0.743	0.257

Table E-3 : Fractional density and porosity of low chloride dust sintered at 400 ^{0}C

Time (min)	**Fractional density** (-)	**Porosity** (-)
0	0.570	0.430
0	0.564	0.436
0	0.566	0.434
5	0.675	0.325
5	0.664	0.336
5	0.669	0.331
7	0.706	0.294
7	0.689	0.311
7	0.685	0.315
10	0.737	0.263
10	0.728	0.272
10	0.711	0.289
15	0.801	0.199
15	0.783	0.217
15	0.774	0.226
20	0.819	0.181
20	0.814	0.186
20	0.811	0.189
30	0.829	0.171
30	0.833	0.167
30	0.850	0.150
30	0.844	0.156
30	0.832	0.168
30	0.820	0.180
30	0.815	0.185

Table E-3 : (continued)

Time (min)	Fractional density (-)	Porosity (-)
45	0.870	0.130
45	0.853	0.147
45	0.846	0.154
60	0.888	0.112
60	0.885	0.115
60	0.892	0.108
120	0.921	0.079
120	0.916	0.084
120	0.902	0.098
480	0.956	0.044
480	0.958	0.042
480	0.955	0.045
480	0.972	0.028
480	0.978	0.022
480	0.971	0.029

Table E-4 : Fractional density and porosity of low chloride dust sintered at 450 ^{0}C

Time (min)	**Fractional density** (-)	**Porosity** (-)
0	0.585	0.415
0	0.583	0.417
0	0.583	0.417
3	0.723	0.277
3	0.709	0.291
3	0.721	0.279
4	0.801	0.199
4	0.788	0.212
4	0.795	0.205
5	0.838	0.162
5	0.811	0.189
5	0.826	0.174
7	0.881	0.119
7	0.852	0.148
7	0.852	0.148
10	0.921	0.079
10	0.918	0.082
10	0.912	0.088
15	0.944	0.056
15	0.936	0.064
15	0.936	0.064
20	0.967	0.033
20	0.962	0.038
20	0.950	0.050
30	0.971	0.029
30	0.969	0.031
30	0.965	0.035

Table E-4 : (continued)

Time (min)	Fractional density (-)	Porosity (-)
60	0.983	0.017
60	0.992	0.008
60	0.986	0.014
60	0.983	0.017
60	0.986	0.014
60	0.980	0.020
60	0.977	0.023
60	0.977	0.023
480	0.999	0.001
480	0.995	0.005

Table E-4 : (continued)

Time (min)	Fractional density (-)	Porosity (-)
0	0.551	0.449
0	0.553	0.447
0	0.557	0.443
5	0.776	0.224
5	0.747	0.253
5	0.760	0.240
10	0.877	0.123
10	0.867	0.133
10	0.864	0.136
15	0.915	0.085
15	0.911	0.089
15	0.890	0.110
30	0.957	0.043
30	0.953	0.047
30	0.937	0.063
60	0.974	0.026
60	0.964	0.036
60	0.958	0.042

Table E-4 : (continued)

Time (min)	Fractional density (-)	Porosity (-)
0	0.498	0.502
0	0.493	0.507
0	0.487	0.513
5	0.654	0.346
5	0.628	0.372
5	0.638	0.362
10	0.779	0.221
10	0.759	0.241
10	0.753	0.247
15	0.824	0.176
15	0.814	0.186
15	0.774	0.226
30	0.898	0.102
30	0.884	0.116
30	0.882	0.118
60	0.934	0.066
60	0.929	0.071
60	0.926	0.074

Table E-4 : (continued)

Time (min)	**Fractional density** (-)	**Porosity** (-)
0	0.375	0.625
0	0.369	0.631
0	0.370	0.630
5	0.562	0.438
5	0.513	0.487
5	0.534	0.466
10	0.655	0.345
10	0.634	0.366
10	0.639	0.361
15	0.695	0.305
15	0.677	0.323
15	0.675	0.325
30	0.774	0.226
30	0.764	0.236
30	0.746	0.254
60	0.841	0.159
60	0.839	0.161
60	0.796	0.204

Table E-5 : Fractional density and porosity of low chloride dust sintered at 500 ^{0}C

Time (min)	**Fractional density** (-)	**Porosity** (-)
0	0.628	0.372
0	0.615	0.385
0	0.620	0.380
1	0.755	0.245
1	0.716	0.284
1	0.714	0.286
1	0.753	0.247
1	0.725	0.275
2	0.848	0.152
2	0.824	0.176
2	0.834	0.166
2	0.827	0.173
2	0.824	0.176
3	0.877	0.123
3	0.856	0.144
3	0.883	0.117
3	0.860	0.140
3	0.873	0.127
5	0.934	0.066
5	0.944	0.056
5	0.944	0.056
7	0.979	0.021
7	0.974	0.026
7	0.974	0.026
7	0.969	0.031
7	0.973	0.027
7	0.978	0.022

Table E-5 : (continued)

Time (min)	Fractional density (-)	Porosity (-)
10	0.980	0.020
10	0.977	0.023
10	0.976	0.024
15	0.990	0.010
15	0.995	0.005
15	0.983	0.017
30	0.993	0.007
30	0.997	0.003
30	0.986	0.014
60	0.986	0.014
60	0.987	0.013
60	0.993	0.007
120	0.992	0.008
120	0.985	0.015
120	0.985	0.015
240	0.993	0.007
240	0.990	0.010
240	0.992	0.008
480	0.984	0.016
480	0.997	0.003
480	0.991	0.009
480	0.989	0.011
480	0.989	0.011
480	0.994	0.006

Table E-6 : Fractional density and porosity of high chloride dust sintered at 350 ^{0}C

Time (min)	Fractional density (-)	Porosity (-)
30	0.498	0.502
30	0.487	0.513
30	0.492	0.508
60	0.495	0.505
60	0.500	0.500
60	0.494	0.506
120	0.500	0.500
120	0.517	0.483
120	0.504	0.496
240	0.516	0.484
240	0.511	0.489
240	0.520	0.480
480	0.530	0.470
480	0.536	0.464
480	0.557	0.443

Table E-7 : Fractional density and porosity of high chloride dust sintered at 400 ^{0}C

Time (min)	Fractional density (-)	Porosity (-)
0	0.477	0.523
0	0.490	0.510
0	0.484	0.516
5	0.508	0.492
5	0.505	0.495
5	0.492	0.508
10	0.529	0.471
10	0.525	0.475
10	0.514	0.486
15	0.554	0.446
15	0.534	0.466
15	0.531	0.469
20	0.566	0.434
20	0.543	0.457
20	0.551	0.449
30	0.579	0.421
30	0.573	0.427
30	0.582	0.418
60	0.616	0.384
60	0.614	0.386
60	0.596	0.404
120	0.642	0.358
120	0.639	0.361
120	0.645	0.355
480	0.745	0.255
480	0.754	0.246
480	0.745	0.255

Table E-8 : Fractional density and porosity of high chloride dust sintered at 450 ^{0}C

Time (min)	Fractional density (-)	Porosity (-)
0	0.495	0.505
0	0.497	0.503
0	0.485	0.515
5	0.601	0.399
5	0.584	0.416
5	0.580	0.420
7	0.660	0.340
7	0.649	0.351
7	0.646	0.354
10	0.688	0.312
10	0.682	0.318
10	0.660	0.340
15	0.743	0.257
15	0.725	0.275
15	0.694	0.306
30	0.850	0.150
30	0.825	0.175
30	0.829	0.171
30	0.804	0.196
30	0.788	0.212
60	0.900	0.100
60	0.875	0.125
60	0.855	0.145
480	0.949	0.051
480	0.982	0.018
480	0.981	0.019

Table E-9 : Fractional density and porosity of high chloride dust sintered at 500 ^{0}C

Time (min)	Fractional density (-)	Porosity (-)
0	0.506	0.494
0	0.504	0.496
0	0.505	0.495
5	0.883	0.117
5	0.855	0.145
5	0.852	0.148
7	0.923	0.077
7	0.894	0.106
7	0.901	0.099
10	0.973	0.027
10	0.967	0.033
10	0.970	0.030
30	0.996	0.004
30	0.996	0.004
30	0.993	0.007
480	0.989	0.011
480	0.992	0.008
480	0.986	0.014